Discrete Modeling of Drying Induced Ion Transport and Crystallization in Porous Media

Dissertation
zur Erlangung des akademischen Grades

Doktoringenieur
(Dr.-Ing.)

von M.Sc. Arman Rahimi
geb. am 15.05.1987 in Mashhad, Iran

genehmigt durch die Fakultät für Verfahrens- und Systemtechnik
der Otto-von-Guericke-Universität Magdeburg

Promotionskommission:	Prof. Dr. Heike Lorenz (Vorsitz)
	Prof. Dr.-Ing. habil. Evangelos Tsotsas (Gutachter)
	Prof. Dr.-Ing. habil. Achim Kienle (Gutachter)
	Dr.-Ing. habil. Thomas Metzger (Gutachter)

eingereicht am:	19.06.2019
Promotionskolloquium am:	13.11.2019

Declaration

I hereby declare that I prepared the dissertation with the title:

"Discrete modeling of drying induced ion transport and crystallization in porous media"

without inadmissible assistance and without the use of any aids other than those indicated. Facts or ideas taken from other sources, either directly or indirectly, have been marked as such. In particular, I did not use the services of a commercial graduation consultation. Further, I have not made payments to third parties either directly or indirectly for any work connected with the contents of the submitted dissertation.

The work has not so far been submitted either in Germany or abroad in same or similar form as a dissertation and has also not yet been published as a whole.

Magdeburg, June , 2019

M.Sc. Arman Rahimi

Abstract

Crystallization has been the subject of many studies over the years. The general process that leads up to crystallization is enrichment of ions in liquid phase (salt solution) until a certain value, known as saturation concentration, has been exceeded. There are generally two scenarios which may lead to ion enrichment namely temperature variation and evaporation of the solvent. It is essential to take ion transportation in the liquid phase into account if the enrichment process is to be fully understood. The kinetics of crystallization has also been studied extensively. The entirety of the crystallization process consists of two separate phenomena of nucleation and growth. However, an area in which further investigation is necessary is crystallization in porous media, especially during drying. A thorough understanding of the whole process is still missing due to the complexity of drying porous media combined with the effects of dissolved components, as well as crystallization mechanism and the influence of crystal formation on drying.

In this work, we focus mainly on ion transport in the liquid phase, with a discrete approach to the modeling of porous media. The main mechanisms responsible for ion transport namely advective flow of the ions with the bulk of liquid and diffusion of the ions due to elevated concentration (which is a result of advection) have been taken into account. On the contrary, adsorption of ions at the solid phase (pore walls) as well as all the colligative effects of salt solutions have been neglected. Crystallization has only been modeled from a pseudo-thermodynamic aspect, i.e. the growth and nucleation rate of crystals are not included in the model. In fact, none of the major effects of the crystal formation has been taken into account (such as: clogging of pores due to crystal growth, change in the drying rate, etc.).

Pore network modeling (PNM) is shown to be a helpful tool in investigating the influence of individual variables, such as drying rate and pore size distribution, on the final crystallization pattern. In a pore network model, the void space of porous media is represented by an interconnected network of pores and throats. In this thesis, two different types of pore network models with different pore geometries and

rules regarding the motion of liquid in the network have been proposed. The basic model consists of cylindrical throats connected via nodes that have no volume. Simulations of this model usually start with a fully saturated network with uniform salt concentration until the network is completely dry. Liquid can flow within one liquid cluster but may not invade throats which have already been dried. Ion transport in the throats is based on a 1D advection-diffusion equation. In order to validate the model two test cases have been investigated and it is demonstrated that numerical error is highly dependent on the local Péclet number (Pe). As a result, the throats have been selectively discretized based on their local-temporal Pe number and refining and coarsening of the grid is possible. The advanced model, which is capable of simulating wetting process in addition to drying process of porous media, comprises of spherical pores at the junctions of cylindrical throats. Simulations generally consist of a so-called wetting stage in which a liquid reservoir at the network surface is utilized to supply liquid to the empty network. As the reservoir depletes the simulation enters a second period, namely drying stage, where the liquid that has infiltrated the network evaporates. The model combines wetting and drying algorithms with a new geometry and drying takes place during the entire process. Ion transport and crystallization in the advanced model is unaltered. However, the addition of the new spherical pores introduces a new element in the algorithm for which no sub-discretization has been done. The simulation results obtained from both models have been compared to one another for identical pore networks. In many cases, the basic model can be utilized for faster computation at the expense of certain physical effects.

3D pore network simulations have been carried out only with the basic model since the computation cost does not allow for relevant 3D network size with the advanced model. However, taking into account the crystallization pattern and drying curves reported in other sources certain modifications to the geometry proved essential (specifically due to overestimated drop in the drying rate after a short first drying period). Further investigation revealed that porosity of basic PNMs is generally too low for a typical porous material. This issue was tackled by introducing bundles of capillaries instead of single throats connecting neighboring nodes. Drying curves obtained from simulations by this modified model show an extended first drying period as well as a smooth decrease during the transition to the second drying period. Furthermore, it has been demonstrated that slow drying causes the majority of salt to crystallize on the surface of the network (efflorescence), whereas fast drying leads to more crystallization within the network, especially beneath the surface (subflorescence).

Another important aim of the pore network simulations has been to identify whether

the results are consistent among randomly generated networks of the same size. To this goal, Monte-Carlo type simulations have been carried out. Salt profiles have been plotted and variance of the data for each set of simulations has been studied. It is concluded that for high drying rate the variance decreases significantly via an increase in network size. The case of slow drying and high initial concentration shows good reproducibility for both small and large pore network simulations. In this case, the representative network size is achieved measurably smaller. Lowering the concentration while keeping the drying rate low introduces some more inconsistency in the results. The variance of the data is especially high for simulations with smaller networks, whereas the reproducibility of the results benefits from network size increase.

Kurzzusammenfassung

Kristallisation ist ein seit langem untersuchter Prozess. Er beruht auf der Anreicherung von Ionen in der flüssigen Phase (Salzlösung), bis ein bestimmter Wert, die Sättigungskonzentration, erreicht werden ist. Im Allgemeinen gibt es zwei Szenarien, die zur Ionenanreicherung führen, Temperaturveränderung und Verdunstung des Lösungsmittels. Um die Ionenanreicherung vollständig zu verstehen, ist es notwendig den Transport der Ionen in der flüssigen Phase zu berücksichtigen. Außerdem muss die Kinetik der Kristallisation ausführlich untersucht werden. Der gesamte Kristallisationsprozess besteht aus zwei separaten Phänomenen, Keimbildung und Wachstum. Hinsichtlich der Kristallisation in porösen Medien, insbesondere während Trocknung, sind weitere wissenschaftliche Untersuchungen notwendig. Aufgrund der Komplexität der kombinierten Trocknung und Kristallisation in porösen Medien sowie des Einflusses der gelösten Komponente, fehlt ein umfassendes Verständnis des Gesamtprozesses.

In der vorliegenden Doktorarbeit liegt der Fokus hauptsächlich auf dem Ionentransport in der flüssigen Phase, mit einer diskreten Modellierung der porösen Medien. Die Hauptmechanismen, die für den Ionentransport verantwortlich sind, der advektive Transport der Ionen sowie die Diffusion der Ionen aufgrund einer erhöhten Konzentration (verursacht durch Advektion), werden entsprechend berücksichtigt. Alledings werden die Adsorption der Ionen an der festen Phase (Porenwände) und die kolligativen Eigenschaften der Salzlösung vernachlässigt. Die Kristallisation wird mit einem pseudo-thermodynamischem Ansatz modelliert. Wachstums- und Keimbildungsrate der Kristalle werden vernachlässigt, ebenfalls wie die Haupteffekte der Kristallbildung (Verstopfung der Poren aufgrund des Kristallwachstums, Änderung der Trocknungsgeschwindigkeit).

Porennetzwerkmodelierung (PNM) ermöglicht die Ermittlung des Einflusses einzelner Variablen, wie Trocknungsgeschwindigkeit und Porengrößenverteilung, auf das finale Kristallisationmuster. In einem Porennetzwerkmodell wird der Leerraum der porösen Medien durch ein Netzwerk von verbundenen Poren und Hälsen dargestellt.

In dieser Doktorarbeit werden zwei verschiedene Konzepte von Porennetzwerkmodellen mit unterschiedlicher Porengemometrie und Regeln bezüglich der Bewegung der Flüssigkeit im Netzwerk vorgestellt. Das grundsätzliche Modell besteht aus zylindrischen Hälsen, die durch Knoten ohne eigenes Volumen verbunden sind. Simulationen mit diesem Modell beginnen in den meisten Fällen mit einem vollständig gesätigten Netzwerk mit gleichmäßiger Lösungsmittelkonzenration und werden durchführt bis das gesamte Netzwerk komplett getrocknet ist. Die Flüssigkeit kann nicht in bereits ausgetrocknete Hälse strömen. Der Ionentranport in einem Hals basiert auf einer eindimensionalen Advektions-Diffusions Gleichung. Um das Modell zu validieren, werden zwei Testszenarien untersucht und es wird gezeigt, dass der numerische Fehler stark von der Péclet-Zahl abhängt. Daher werden die Hälse im Bezug auf die lokale Pe-Zahl selektiv diskretisiert und das Gitter entsprechend verfeinert oder vergröbert. Das verbesserte Modell, welches neben der Trocknung der porösen Medien auch den Benetzungsprozess abbilden kann, besteht aus sphärischen Poren an den Verbindungsstellen der Hälse. In der Regel bestehen die Simulationen aus einer sogennanten Benetzungsphase, während welcher ein Flüssigkeitsreservoir an der Oberfläche des Netwerks das leere Netzwerk mit der Flüssigkeit beliefert. Wenn dieses Reservoir erschöpft ist, tritt in der Simulation die Trocknungsphase ein, in der die Flüssigkeit, die vorher von dem Netzwerk eingesaugt wurde, verdunstet. Dieses Model kombiniert die Algorithmen von Verdunstung und Benetzung mit einer neuen Geometrie. Trocknung findet während des gesamten Prozesses statt. Weiterhin soll erwähnt werdem, dass der Ionentransport und Kristallisation sind im verbesserten Modell unverändert. Allerdings wird durch die sphärischen Poren ein neues Element in das Modell eingeführt, für das keine Diskretisierung durchgefürt wird. Die Simulationergebnisse beider Modellen werden für identische Porennetwerke miteinander verglichen. Aus den Ergebnissen wird gefolgert, dass in bestimmten Fällen das einfachere Modell verwendet kann, um kürzere Rechenzeiten zu erhalten. Allerdings werden dann einige physikalische Effekte nicht berücksichtigt.

Dreidimensionale Porennetzwerksimulationen werden wegen des erhöhten Rechenaufwandes des verbesserten Modells ausschließlich mit dem einfachen Modell durchgeführt. Allerdings erweisen sich unter Berücksichtigung des Kristallisationsmusters und der Trocknungskurve bestimmte Modifizierungen an der Geometrie als notwendig (insbesondere wegen des zu steilen Rückgangs der Trocknungsgeschwindigkeit nach dem ersten Trocknugsabschnitt). Zuzätzlich sin die Porositäten der zuvorgenannten Porennetzwerke generell zu niedrig für ein typisches poröses Material. Dieses Problem wurde durch Einführung von Kapillarbündeln, anstatt einzeler Hälse, zur die Verbindung benachbarter Knoten gelöst. Die durch Simulation mit dem modifizierten Modell erhaltenen Trocknungskurven zeigen einen verlängerten ersten Trocknungsab-

schnitt und einen weniger steilen Verlauf im zweiten Trocknungsabschnitt. Zusätzlich wird gezeigt, dass langsame Trocknung zur verstärkten Kristallbildung auf der Oberfläche führt, wohingegen schnelle Trocknung mehr Kristallisation innerhalb des Netzwerkes (insbesondere unter der Oberfläche) bewirkt.

Ein weiteres Ziel der Porennetzwerksimulationen war zu prüfen, ob die Ergebnisse bei zufällig generierten Netzwerken gleicher Größe einheiten bleiben. Zu diesem Zweck wurden Monte-Carlo-Simulationen durchgeführt, in denen alle Bedingungen außer der Netzwerkgenerierung konstant gehalten wurden. Die resultierenden Salzprofile werden grafisch dargestellt und die Varianz der Daten jeder Simulationsreihe wird untersucht. Aus den Ergebnissen kann geschlossen werden, dass sich bei hohen Trocknungsgeschwindingkeiten und steigender Netzwerkgröße die Varianz der Daten signifikant verringert. Die Ergebnisse für langsame Trocknung bei hohen Anfangskonzentrationen zeigen eine gute Reproduzierbarkeit für sowohl kleine als auch große Netzwerke. In diesem Fall ist die repräsentative Netzwerkgröße kleiner. Niedrige Anfangskonzentrationen bei langsamer Trocknung führen zu höherer Inkonsistenz in den Ergebnissen. Die Varianz den Daten ist insbesondere hoch für die Simulationen kleinerer Netzwerke. Somit verbessert eine Vergrößung des Netzwerks die Reproduzierbarkeit der Ergebnisse.

Contents

Nomenclature

Notations

A	cross-sectional area	m^2
B	nuclei birth rate	s^{-1}
C	concentration	$kg \cdot m^{-3}$
D	diffusion coefficient in the liquid phase	$m^2 \cdot s^{-1}$
H	droplet height	m
J	diffusive flux	$kg \cdot m^{-2} \cdot s^{-1}$
K	permeability	m^2
k	rate constant	$-$
L	length	m
$\dot{M}$	mass flow rate	$kg \cdot s^{-1}$
$\tilde{M}$	molar mass	$kg \cdot mol^{-1}$
N	number of nuclei	$-$
n	empirical exponent for nuclei formation	$-$
P	pressure	Pa
p	partial pressure	Pa
Q	volumetric flow rate	$m^3 \cdot s^{-1}$
$\tilde{R}$	universal gas constant	$J \cdot mol^{-1} \cdot K^{-1}$
r	radius	m

t	time	s
u	velocity	$m \cdot s^{-1}$
V	volume	m^3
W	sessile droplet diameter	m
x	position	m
y	position	m
z	position	m

Superscripts and subscripts

b	bulk
c	capillary
d	droplet
g	gas
i	throat or pore index
ij	throat connecting pores i and j
j	throat or pore index
k	throat or pore index
l	liquid
Np	number of pores
Nt	number of throats
old	old values
p	pore
s	solid
$salt$	salt
v	vapor

w	water	
0	initial	
ϵ	excessive	
$*$	saturation	
∞	ambient	

Greek symbols

δ	diffusion coefficient in the gas phase	$m^2 \cdot s^{-1}$
ϵ	porosity	-
μ	dynamic viscosity	$Pa \cdot s$
ρ	density	$kg \cdot m^{-3}$
σ	surface tension	$N \cdot m^{-1}$
τ	shear stress	N
θ	contact angle	$degree$

Abbreviations

$2D$	two dimensional
$3D$	three dimensional
adv	advection
Ca	capillary number
CRP	constant rate period
$diff$	diffusion
EPD	efflorescence pathway diagram
FRP	falling rate period
MRI	magnetic resonance imaging
Pe	Péclet number

PSD pore size distribution

We Weber number

Matrices

A contribution matrix

b boundary condition matrix

C concentration matrix at throats, pores or nodes

P matrix of pressure at throat junctions

Chapter 1

Introduction

1.1 Background

Transport phenomena in porous media has been a subject of research from many perspectives through decades. The complexity of related issues is highly dependent on the envisaged applications as well as the variety of phenomena involved. Moreover, there has been considerable amount of effort put into the modeling of such processes. Generally, two approaches are proposed for modeling transport phenomena in porous media, namely the continuum approach and the discrete approach. The aforementioned approaches are fundamentally different both in term of priorities as well as the information they provide. Continuum models are generally favored because of the fast computational rate of respective numerical solutions and the ability to simulate larger scale problems. The main disadvantage of this approach lies in the fact that it is most suitable for single phase problems. On the other hand, the discrete approach is best suited for micro-scale problems, especially when detailed information on the behavior of different phases involved is necessary so that this approach generally deals with multiphase problems.

Drying porous media in the presence of dissolved materials is common in everyday life and industry. There are two sides to this process which makes it an interesting subject for research: Applications of crystallization/precipitation in porous media (desired) and the issues instigated by unwanted crystallization (undesired). For instance, production of catalyst by impregnation of catalyst supports is one of the main methods of catalyst production. On the contrary, crystallization can be detrimental to the integrity of construction materials and historical monuments. However, the overall understanding of the entire process is currently mediocre due to several reasons such as the complexity of drying porous media as an independent subject,

tracking of the dissolved component as other transport phenomena take place, etc. Another important part of this process, to which even less attention has been paid, is the sequence of events or, more specifically, the stage of the process in which the porous medium is filled or contaminated by the solution. Sometimes, the liquid is still being supplied to the porous medium as drying and crystallization take place, for instance in case of building material exposed to ground salt water. In this sense, development of a model that can explain these phenomena in detail and provide an understanding of different scenarios is paramount. Hence, pore network modeling (as a form of the discrete approach) is expected to be a powerful tool that can handle said subjects immaculately on relatively simple first principles.

1.2 Porous media

Porous media are a subcategory of solid materials in which a large proportion of the volume consists of interconnected pores (voids). In some cases, the entire void space of such materials can be interconnected, whereas in others certain clusters of pores might be disconnected from the bulk of the void space. Porous media either exist naturally such as soil, fruits, sediments, etc. or are man-produced such as paper, construction bricks, catalyst supports, etc. Generally, a porous medium is characterized by two main properties: porosity and pore size distribution (PSD), neither of which on its own provides adequate information to fully describe the material. Porosity (ϵ) is an average number that is defined as the ratio of total void volume (V_p) to the bulk volume of the porous medium (V_b):

$$\epsilon = \frac{V_p}{V_b} = 1 - \frac{V_s}{V_b}. \tag{1.1}$$

The void volume can be obtained by subtracting from the bulk volume the solid volume (V_s). Porosity is a good measure for how much liquid a porous medium contains or can take up, granted it is not always possible to remove all the liquid from pores by standard means (hygroscopic material). Alternatively, pore size distribution provides general information on the topology of void space in porous materials, or more simply, tells how the void volume is distributed within the solid matrix. This characterizing property is vital to fluid flow within the material and, as shall be discussed later, can be used to define parameters, such as capillary pressure (P_c), or to inform whether certain effects, e.g. Knudsen diffusion [48], take place. A tertiary property which is often neglected when characterizing porous media is the shape of the pores, especially if a continuum approach is taken towards the modeling. As a

matter of fact, certain effects are byproducts of specific pore geometry such as the film effect [83] [114] [116].

Combining all the knowledge mentioned beforehand, pore network models can be utilized to approximate the void space of a porous medium. Generally, this approximation works at three different levels [45]. At first, a simple type of geometry is selected to describe the pores e.g. cylindrical tubes [23], tetrahedrons [12], or cubic tubes [40]. Secondly, the network is constructed by arranging the aforementioned pores in a specific pattern which takes into account dimensions, coordination numbers, and regularity. Finally, transport phenomena at the pore level should be described, which accounts for physical properties of the materials involved, PSD, etc.

There are several factors by which transport phenomena in porous media are controlled. The most important of them are as follows:

• **Capillarity:** Physical systems which exhibit coexistence of all three phases of matter (solid, liquid, gas) may be subject to capillarity. The source of this mechanism is surface tension. By definition, surface tension is the force required to form a unit area of the interfacial surface. However, interfacial forces do not always lead to significant capillarity. It is essential for a ternary interface to be formed in a narrow confined space for capillarity to have considerable effect in the system. A direct result of capillarity is the change in liquid pressure at the interface denoted as capillary pressure (P_c). For simple geometries, capillary pressure can be calculated analytically. For instance, capillary pressure for a cylindrical tube of radius r and liquid with a surface tension of σ and contact angle of θ can be formulated as [117]:

$$P_c = \frac{2\sigma}{r} cos\theta. \tag{1.2}$$

This pressure drop in the liquid phase can establish a pressure gradient between regions with different capillary pressures and consequently liquid flow in the medium.

• **Diffusion:** In a porous medium, convective transport of fluids is hindered due to the obstructions caused by the surrounding solid matrix. As a result, the movement of molecules may play an important role, especially in the gas phase, in mass transfer through pores. Diffusion is generally driven by a gradient in the concentration of different components within the fluid phase. This implies that systems in which more than one component coexist within a single phase are subject to diffusion as a means of mass transport. For instance, in the course of drying a constant flow of water molecules from the water-gas interface (high concentration) to the surroundings (low concentration) is established. Within the pore space of a porous medium diffusion

may be the main source of mass transfer. According to Fick's first law of diffusion [24], diffusion flux (J) is formulated as the product of a diffusion coefficient (D) and the concentration gradient ($\frac{\partial C}{\partial x}$):

$$J = -D\frac{\partial C}{\partial x}. \tag{1.3}$$

Generally, diffusion and bulk flow (advection) occur simultaneously and make up the entire convective transport. However, depending on different conditions one mechanism may dominate the process to an extent that renders the other one irrelevant.

• **Viscosity:** Viscosity is defined as the resistance of fluids against motion caused by shear or tensile stress. Newton's law of viscosity implies that shear stress in a fluid (τ) is proportional to the derivative of velocity in the direction perpendicular to the flow plain:

$$\tau = -\mu\frac{\partial u}{\partial y}, \tag{1.4}$$

where μ is the dynamic viscosity of the fluid. The resistance caused by viscosity acts against the motion hindering free fluid movement in the system. Consequently, as fluids flow within confinements, the aforementioned resistance is at its maximum in regions closest to the solid wall. At the limit, it is assumed that fluid molecules located at the wall are stationary, also known as "no-slip condition" [18]. In the case of a porous medium with cylindrical tubes representing the pores, a parabolic velocity profile for fluid flow can be derived where the velocity reaches a maximum at the center of the tube. On this basis, the pressure drop along a cylindrical tube can be obtained from the Hagen-Poisueille [106] equation as follows:

$$\Delta P = \frac{8\mu LQ}{\pi r^4}, \tag{1.5}$$

where ΔP is pressure drop, Q volumetric flow rate, and L and r length and radius of the tube respectively.

1.3 Drying of porous media

Drying refers to the process during which liquid is removed from solid materials by means of evaporation. In a wet porous medium, the majority of the liquid is

located within the pores of the solid matrix (as opposed to free liquid at the surface). Hence, drying of porous media involves liquid removal from the depth of the material. There are many different methods for drying porous media such as convective drying, vacuum or freeze drying, dielectric drying, etc. Among all these methods, convective drying is by far the most popular mainly due to its simplicity. In the course of convective drying, the liquid is removed from the solid by exposure to a constant flow of drying agent (most commonly hot air). The entire process comprises of three stages, namely: warm-up period, constant drying rate period denoted by "CRP" (also known as "first drying period"), and falling drying rate period denoted by "FRP" (also referred to as "second drying period").

Drying is initiated as the solid material comes into contact with hot air where almost the entire heat supplied to the product is consumed to raise the temperature. The mass transfer in this period is minimal until the temperature of the medium (solid and liquid) reaches a certain value at which point drying starts.

The warm-up period is followed by the constant rate period. During this stage, free liquid present at the surface and the majority of liquid located in the macro-pores evaporates at a constant rate. The evaporation rate in this period is dependent only on external conditions such as temperature, humidity, and flow velocity. Capillary forces are responsible to supply enough liquid for evaporation from the surface of the material. As long as the liquid flow resistance can be overcome, constant drying rate is maintained and correspondingly the first drying period. This stage is vital for products sensitive to heat as the temperature of the material remains more or less constant, at the "wet bulb temperature", essentially protecting them.

As the moisture content of the medium decreases, eventually, liquid flow resistance exceeds the capacity of capillary forces in the system. From this point on, liquid transfer is hindered and an increasing number of dry spots appear at the surface. As a result, the limiting mass transfer resistance moves within the solid matrix (as opposed to CRP). Several mechanisms are at play which define the drying rate at this stage, such as viscous-capillary flow of liquid within liquid clusters, diffusion rate of vapor in the gas within the pores, thermal effects, etc.

Drying curves are utilized as the typical means to study drying of porous media. Such a curve is produced by plotting drying rate at every moment versus the corresponding moisture content. The characteristic drying periods (CRP and FRP), which are separated by the critical moisture content (X_{cr}), can be nicely demonstrated in these curves. Exemplary drying curves for hygroscopic and non-hygroscopic materials are shown in Figure 1.1.

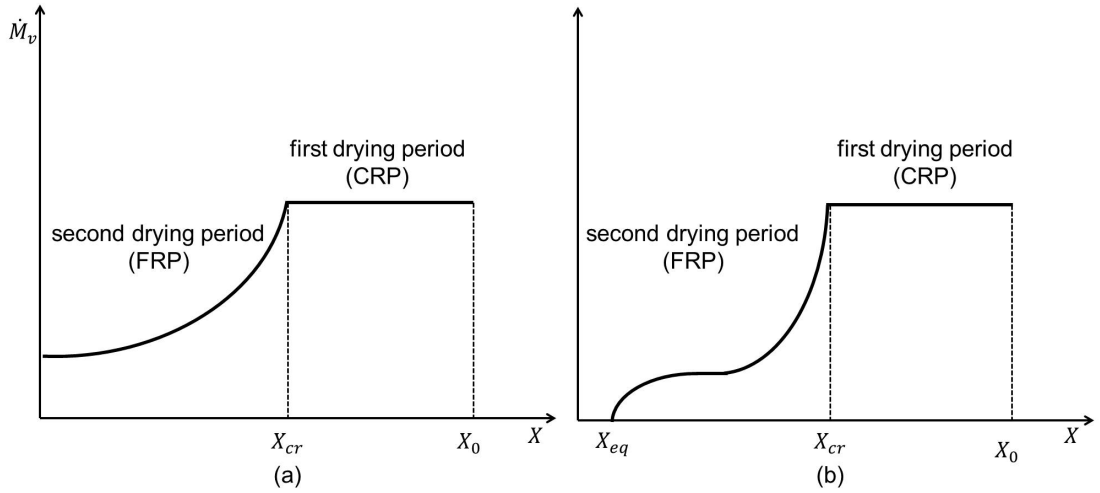

Figure 1.1: Drying curve for (a) non-hygroscopic and (b) hygroscopic porous material (adopted from [41]).

1.4 Wetting of porous media

As an external source of liquid comes in contact with solid material, the liquid may spread on and infiltrate the solid phase (in case of porous media). This action is defined as wetting. The necessary condition for wetting to occur requires the surface tension between solid and liquid being greater than that of the liquid itself or, in other words, the combination of liquid and solid should be hydrophilic. This process takes place in nature and has many industrial applications such as water suction in plant stems, ink-jet printing, spray painting, functionalization of solid supports by impregnation, etc. In the 19th century Darcy managed to extract an empirical equation which describes the interstitial velocity of liquid (u_0) in a single phase system as follows [15]:

$$u_0 = \frac{Q}{A\epsilon} = -\frac{K}{\mu}\frac{\Delta P}{L}. \tag{1.6}$$

The term K represents permeability and it showed up for the first time in Darcy's law. In theory, permeability stores all the necessary information about the ease or difficulty of fluid flow in porous media and is dependent on the void space of the medium [3].

Later on and referring to a two-phase-system, Lucas [58] and Washburn [111] discovered that the liquid travel length in a cylindrical capillary is proportional to the square root of time ($L \sim \sqrt{t}$). They used the analytical derivation of Poiseuille's law to formulate their equation as follows:

$$\frac{dL}{dt} = \frac{r\sigma cos\theta}{4\mu L}. \tag{1.7}$$

The Lucas-Washburn equation was later modified to calculate the rate of liquid penetration in porous media by taking porosity, i.e. the effective cross-sectional area for liquid flow, into account. However, one important caveat here is that all models utilizing this equation take an average value for pore radius for a certain porous medium. This fact causes some limitations in the range of applicability of said models. For example, efforts to validate the Lucas-Washburn equation have failed for certain scenarios of long-period capillary rise [56]. In that and several other articles solutions for specific cases have been proposed [27] [33].

1.5 Crystallization

A crystal is defined as a rigid solid structure of matter in which molecules or atoms are periodically well-ordered in lattice patterns in space. Crystallization is the process of forming crystals from dispersed molecules or atoms. Commonly, crystals are formed by precipitation of solid from a solution.

Crystallization consists of two consecutive phenomena namely nucleation and growth. Nucleation refers to the formation of solid surface within the liquid phase (which requires considerable amount of energy). This phenomenon consists of the transition of atoms or molecules from the liquid to the solid phase in a very small region of space. Nucleation generally requires a high degree of supersaturation due to its high activation energy. The birth rate of nuclei (B) as a function of supersaturation can be described as follows [107]:

$$B = \frac{dN}{dt} = k_n(C - C^*)^n, \tag{1.8}$$

where N is the number of nuclei per unit volume, k_n the rate constant, C concentration at given time, C^* saturation concentration and n an empirical exponent. Once enough nuclei have been formed, nucleation comes into a halt and growth starts to take over. As long as some degree of supersaturation in the solution is maintained, solute molecules are transferred constantly to the nuclei. Consequently, the size of the nuclei increases over time at a certain rate. Many models have been proposed where depending on the application, growth has been described by utilizing population balance equations [4] [28]. The most important influencing factors on growth rate in these models are the degree of supersaturation and the total crystal surface

area per unit volume of solution.

There are mainly two methods for achieving the supersaturation necessary for crystallization, namely the cooling method and the evaporative method [64]. The solubility of most solid materials is dependent on temperature. In the cooling method, the temperature of the solution is increased initially so that the solute can be transferred from its impure form to the liquid (extraction). After the saturation concentration has been reached, the solution is transferred to a cooling apparatus where its temperature is lowered rapidly. In doing so, a certain degree of supersaturation is achieved (depending on the former and current temperature of the solution), which leads to precipitation of the excess amount of solute in the form of crystals. Sometimes however, depending on the solute, solubility is not very sensitive to the temperature variation. In this case, manipulating the temperature is an ineffective strategy for crystallization. Instead, considering that the solute is generally much less volatile than the solvent, evaporation can be utilized as a method of reaching supersaturation in the liquid. Often a combination of both methods is used to achieve the desired degree of supersaturation at a higher rate if properties of the materials are suitable for both methods.

1.6 Pore network modeling

Discrete modeling is a powerful tool to study transport phenomena in porous media at the micro-scale. Pore network modeling (mentioned in Section 1.1), as a well-known discrete approach, describes the void space of porous media with an interconnected network of pores. The shape of the pores can be chosen with respect to the problem at hand, however, usually a simple geometry is selected for the sake of simplicity and to enable investigation of more important effects. For the first time, pore network models have been used in an attempt to better describe porous media than it is possible by a bundle of tubes or spheres pack [23]. Afterward, pore network modeling was more or less forgotten until the last two decades of the 20th century. In 1984 Jerauld et al. investigated the effect of random coordination number on the percolation and conduction properties in two types of network [43]. A modified form of invasion-percolation theory was later proposed in a pore network model of pores connected via thin throats [81]. In that model, capillarity, gravity, and evaporation were combined and results showed good agreement with experiments. As an example of more complexly shaped pores, Nowicki et al. generated a network where biconical pore segments intersected at pore bodies to study the drying of porous media [75]. The main aim of that work was to extract effective parameters (K, λ, δ, etc.), by

means of Monte-Carlo type simulations, to use in a continuum approach.

As time went by the utility of pore network models was realized further and new effects were added to previously existing models while new applications were found. Few of these examples are presented here. Thermal effects have been considered in pore network models in [79] [103] [104] [105] [110]. Moreover, imbibition and redistribution of liquid in porous media have been studied by [9] and [102] . Recently, simultaneous wetting and drying of porous media has been successfully modeled where a droplet is described as a reservoir [87]. Mechanical effects on solid material during drying such as shrinkage [95] and crack formation [46] [47] have been studied by pore networks. Despite the recent popularity of pore network models, there are still many areas which could benefit from in-depth micro-scale investigation such as crystallization in porous media.

1.7 Motivation

Crystallization (precipitation) during drying of porous media is a common process in nature while at the same time having many industrial applications. Examples such as protection of building materials and cultural heritage, preservation of soil, inkjet printing, production of catalysts by impregnation of porous supports are only a fringe of where we encounter this process. Despite this fact, the current understanding of the entire process leaves a lot to be desired. In our opinion, the main reason for this lack of understanding is that drying (and wetting) of porous media with pure water (let alone a solution) is complicated, to begin with. Many different approaches have been taken to the problem although almost no concrete model can describe the process in its wholesome for real materials. Addition of a secondary component to the liquid phase opens up a wide range of issues such as tracking of the dissolved molecules, dependency of vapor pressure on concentration, criterion of precipitation, etc.

It has been demonstrated that many details of drying and wetting of porous media can only be captured by discrete modeling [65] [87]. In those works, simulation results on several bimodal networks have been presented for pure drying and combined wetting-drying which show the incapability of continuous modeling to describe certain effects due to medium heterogeneity. On that note, it is reasonable to assume that tracking a secondary component in the liquid phase, which eventually may lead to crystallization, cannot be done by continuous modeling to the desired accuracy. As it is introduced in Section 1.5, crystallization is a microscopic and local phenomenon, therefore it is important to maintain high degree of accuracy in the calculations lead-

ing to it. On the other hand, the main application intended for this work is to predict the distribution of active materials in a catalyst support produced by impregnation. In this industrial process, catalyst supports are filled with a solution of active material, then drying removes the solvent, thus leaving crystals at the surface and within the solid matrix. Being aware of the fact that the distribution pattern of the active component highly impacts the efficiency of the catalysts, it would be of great value to generate a model that can predict the distribution pattern.

To this goal, salt ions have been tracked in the liquid phase by a 1D advection-diffusion equation which is coupled with capillary viscous flow in the drying pore network model. Utilizing an explicit solution scheme for ion transport in the network, sometimes requires the global time-step to be broken down to account for the stability criterion set by the solution scheme. This fact renders the model computationally less efficient than the pure drying model. Furthermore, a more advanced pore network model, capable of simulating simultaneous wetting and drying, with a modified geometry (spheres and cylinders) is coupled with the ion transport-crystallization algorithm. The latter model describes an entire impregnation process starting with an empty network and resulting in scattered salt crystals. The important caveat is that this model is computationally very expensive, limiting at this moment the possibility to run 3D simulations with large network size.

1.8 Thesis outline

This thesis consists of five chapters, the remainder of which is outlined in this section.

The second chapter introduces the ion transport and crystallization algorithm in the context of a drying pore network model. The chapter starts with a review of previous works on pore network modeling mainly related to drying. This is followed by a literature study on salt crystallization in porous media by both experimental and modeling means. Then, the pore network model of choice is briefly introduced to lay out the foundation. Ion transport and crystallization are then embedded into the drying algorithm and coupled with the liquid capillary-viscous liquid flow. The validity and numerical accuracy of the ion transport algorithm are assessed by comparison of the results with two basic test cases. It has been shown that the numerical accuracy of the model is highly dependent on the local Péclet number (Pe) which varies during drying. To tackle this issue, an adaptive discretization method is proposed where each throat is divided into smaller sub-elements leading to a reduction in the local Pe. Finally, several 2D simulation results are presented where the effect of varying drying rate and initial salt concentration can be compared

visually.

In the third chapter salt crystallization during combined wetting and drying of a pore network is studied. At first, a short review of the previous works on modeling wetting and/or imbibition of porous media is conducted. As in the previous chapter, the basis of the model, which in this case is referred to as the wetting-drying pore network model, is initially introduced. This model is based on a previous model of Rahimi et al. [87] with the addition of a number of modifications. Therefore the new rules are explained in detail. In order to point out the improvements and capabilities of this model, a comparison between the two models has been carried out through simulations of small 2D networks. The ion transport and crystallization algorithm also needs to be slightly modified to account for the new pore geometry (spherical pores at the junction of cylindrical throats). It is important to note that liquid flow pattern in this model is very different than that of the drying-crystallization model. Therefore it is necessary to compare the crystallization patterns obtained from the corresponding simulations since some effects are not captured by the drying-crystallization model. It is concluded that the more basic model generates results much more efficiently at the expense of missing certain physical effects. Finally, 2D wetting-drying-crystallization simulations are carried out for larger networks with mono-modal and bimodal pore size distributions.

In the fourth chapter, the basic model (drying-crystallization) has been selected to perform a series of Monte-Carlo type simulations. The reason for selection of this model is the importance of minimizing computational time as a significant number of simulations are carried out. This model has been extended to 3D with one important modification to the pore geometry of the network. It was observed that due to unrealistically low porosity (caused by long narrow cylindrical throats), a large drop in the drying rate occurs at the critical moisture content (X_{cr}). This problem was solved by introducing a coefficient that maps a uniform porosity in the network to each region between two consecutive nodes. Each region contains a bundle of uniform throats (rather than a single throat), but throat radius varies between different regions. Comparison of drying curves for the modified model and the traditional model shows significant improvement. 3D simulations are carried out with the new modified model for various drying rates, initial salt concentrations and pore size distributions. The aim here is to investigate whether the selected network size can be representative for the given initial conditions.

The fifth and final chapter comprises of conclusions from the findings of this thesis as well as of proposing some directions for future work related to this topic.

Chapter 2

Ion transport and crystallization in drying pore network model

2.1 Literature study

Crystallization in porous media during drying is a complicated topic. In certain scenarios, such as the damage induced to construction bricks, this process is undesired and a lot of research has been dedicated to minimize or eliminate it [38] [39] [57], [89] [94]. On the other hand, crystal formation has several industrial applications, as for example, the production of catalysts by impregnation [49] [118]. However, research results regarding these applications are fairly limited compared to the other case of damaging crystallization. In this work, we aim to develop a discrete pore network model which is fully capable of describing this process. However, as a first step previous pore network drying models are briefly reviewed to establish a base understanding of the approach. Then we segue to the experimental and theoretical studies of ion transport and crystallization in porous media prior to explanation of the model.

2.1.1 Review of drying pore network models

In the past couple of decades, pore network modeling has grown in popularity to simulate drying porous media. As one of the oldest models, Nowicki et al. used a network of biconical throats to describe the void space of a porous medium [75]. In that work, vapor transport in the system has been modeled by diffusion whereas the liquid viscosity has been accounted for. As hinted before, the main aim of this model

was to extract effective parameters which would later be used in a continuous model to simulate drying at a reasonable scale. For this purpose, the authors selected a representative network size for which multiple realizations for simulations were carried out. The results were then averaged and effective parameters were extracted as functions of network saturation and drying history.

The next network model that stands out was proposed one year later by Prat [81], based on the modified version of an invasion percolation algorithm which was traditionally used to model the drainage process. The network consisted of cylindrical pore throats. One of the main characteristics of this model was the addition of gravity to the capillary transport of liquid combined with evaporation from menisci. However, viscosity was neglected in both the liquid and the gas phases. Simulations run in 2D configuration were compared with experiments conducted on micromodels to show good agreement. Later, in 1995, Prat compared the standard invasion percolation algorithm (in case of drainage) with a modified version adopted for the drying of a network [82]. Simulations were performed for low capillary number and it was shown that the invasion front and the drying front do not completely overlap. Furthermore, the effect of gravity was studied. In the absence of gravity results that are unique to the pore network simulations (as opposed to the continuum approach) have been presented. Later on, a more extensive comparison between pore network simulations and micromodel experiments, for three different gravitational regimes, was carried out [52] [53]. The main point drawn from these studies was that agreement between simulations and experiments at a qualitative level is achieved whereas in [53] the quantitative agreement was very poor. This discrepancy was then attributed to the presence of liquid films in the experimental setup. Motivated by these findings, the model was extended to account for liquid films [83]. The CRP has been established (or extended) in this model which is a direct contribution of liquid films. This is a good example of how the discrete approach can capture essential microscopic effects which are otherwise neglected, with detrimental effects on the ability to predict reasonable results.

In 2001, Yiotis et al. published results of a pore network model where in addition to vapor diffusion in the gas phase, vapor advection was coupled with capillary-viscous liquid flow [115]. In this specific pore network model, the liquid volume is situated in spherical pores connected via cylindrical throats whose volume is neglected. The problem is mainly characterized by a binary set of dimensionless numbers, namely a diffusion-based capillary number (Ca) and a Péclet number (Pe), alongside the geometrical properties of the network. It is concluded that based on the magnitude of the two aforementioned dimensionless numbers a transition to the percolation-controlled model occurs. The previous model has been extended to account for

liquid films [114]. The results were compared with the results of previous models and experimental works by other authors. It was concluded that liquid films have a significant effect on drying in the capillary dominated regime. On the contrary in a viscous dominated scenario their contribution is negligible.

In pursuit of investigating the role of liquid viscosity in drying pore network models, Metzger et al. proposed a model which coupled the viscous force with capillary induced liquid transport [66]. In that work, the effect of pore size distribution has been studied concluding that stabilization of the drying front can only be achieved in networks with a narrow pore size distribution (2D networks). In the case of wider pore size distribution or bimodal distribution with hierarchical arrangement, i.e. large pores connected to each other forming long channels, capillary forces were far too dominant. Additionally, this model was slightly modified and compared to an older bundle of capillaries model (developed in the year 2005 [67]). The results show similar trends with relatively good agreement between the two models. It is worth mentioning that this model was built upon a previous work where liquid viscosity has been neglected [65]. That model was based on the works of Prat [81] (the invasion percolation algorithm). Various simulation results have been presented for different pore size distributions namely: networks with bimodal PSD with three different spatial correlations for macro-pores, three different coordination numbers for nodes, and finally 3D simulations with some of the aforementioned variations. The results were acquired from Monte-Carlo type simulations and provide valuable information for better understanding of the drying of porous media. The viscous model has also been extended to 3D where a stabilizing drying front is reported especially in the earlier stages [68] (as was also predicted by Prat [84]). It has to be acknowledged that an extremely narrow pore size distribution was deliberately selected for these simulations which leads to almost elimination of the constant drying rate period and generates the stabilized drying front.

In the more recent years pore network modeling has been adopted for various applications, which requires modifications; several examples of respective models and applications are as follows: evaporation of binary liquid mixture from porous media [26], drying of non-isothermal systems [37] [54] [55] [79], inclusion of the capillary valve effect in the course of slow drying of a porous solid [112] [113], modeling of water condensation at the cathodic side in the gas diffusion layer of fuel cells (which exploits a non-isothermal PNM) [6] [100].
Aside from drying, pore network models have been used for applications two of which, namely impregnation and spray agglomeration, will be presented in the following section in the current chapter and Section 3.1.

2.1.2 Review of crystallization in porous media

Utilizing pore network modeling for processes involving porous media other than drying has been the topic of many research projects. Our aim here is to develop a model that can handle drying of porous media in the presence of dissolved salt and ultimately crystallization. However, prior to that, it is essential to review the literature on crystallization in porous media. In the majority of cases, drying is involved, but sometimes crystallization (precipitation) may take place through other means such as chemical reaction.

Traditionally, this process has been viewed as undesired and many studies have been trying to prohibit or delay crystallization. Some of these scenarios include damage induced to building materials and cultural heritages [22] [50] [88] [91] [92], salinization of soil and groundwater sources [36] [69] [71], injection of CO_2 into saline aquifers [2] [78] [85], and crystallization pressure and related issues [42] [93]. At the same time, one of the most popular methods of catalyst production, i.e. impregnation of supports, involves crystallization and drying of porous media [7] [51] [99]. In this process, catalyst supports are filled with a solution containing the active material. These saturated catalyst supports are then dried, under controlled conditions, which allows crystals to form desirably within the solid matrix. However, understanding the aforementioned scenarios requires deep insight in drying of porous media in the presence of a secondary component. Despite its practical importance, this process has neither been completely understood nor deeply researched so far. To the best of our knowledge, the reason is that even standalone drying of porous media is a complicated process. Addition of dissolved component leads to several new phenomena such as variation of vapor pressure, alteration of the pore size distribution of the medium, change in drying rate due to blockage of the pores, etc. On the other hand, in order to develop a proper model the concentration of ions should be tracked in the entirety of the medium and process. In the following, we delve deeper into some of the important works on this topic to aid better understanding of the process.

Preliminarily, it should be pointed out that crystallization pattern is very important with respect to the application. For example, crystal formation at the exterior region of the medium (efflorescence) is desired in protection of masonry whereas crystallization within the solid medium (subflorescence) is desirable in catalyst production since precious active material can be protected within the pores. In order to comprehend the causality of different crystallization patterns, various experiments will be considered. It is worth mentioning that various salts and processes produce completely different crystallization patterns, hence every scenario should be seen within its narrow range of applicability. Ultimately any comparison should be made very

carefully and conclusions have to be drawn with skepticism.

Drying of a particle packing consisting of spherical glass beads saturated with aqueous NaCl solution was experimentally studied in [21]. The average size of the glass beads was varied among the experiments (leading to various pore size distributions). It was shown that the drying process is not affected significantly by the formation of salt crystals; in some cases, evaporation rate is even enhanced if the particle size (and pores as a result) is adequately large. Completely opposite effects were observed in experiments with small glass beads where the pores may even be blocked, severely limiting evaporation and capillary pumping as a result. Considering these two opposite effects, the existence of two regimes has been confirmed: one of which leads to formation of a crusty efflorescence (blocking regime) and the other one to a patchy efflorescence (enhanced drying rate regime). Similarly, the presence of two regimes was observed during the drying of sand columns saturated with saline solutions under constant hydraulic boundary conditions [70]. Evaporation rate was quantified by mass loss measurements and infrared thermography, the latter of which allows spatio-temporal quantification of salt precipitation in the porous medium. It is reported that the evaporation rate was suppressed by up to one order of magnitude from fine-textured regions, whereas the coarse-textured regions exhibited almost constant evaporation rate throughout the experiment. Additionally, comparison between two types of salts, namely NaCl and NaI, showed that the evaporation rate is affected by NaCl crystals much more severely than in case of drying of NaI solution. The explanation for these two effects is rather straight forward: NaCl has a higher tendency to form crusty efflorescence leading to the blockage of surface pores which are essential to maintain the constant drying rate period; whereas NaI is known to form crystals within the porous matrix (subflorescence) not hindering capillary driven transport of liquid to the surface. This effect has also been confirmed in a study of one-sided drying of inorganic building materials (fired-clay bricks) contaminated by NaCl solution [88]. In that work, the nuclear magnetic resonance technique was used to measure moisture and NaCl content within the material. These results were then presented in a so-called efflorescence pathway diagram (EPD). In the end, it has been concluded that in historical objects generally the formation of efflorescence cannot be avoided.

The effect of pore size distribution on crystallization pattern during one-sided drying of plaster/substrate systems (plaster always located at the open side) was studied through various experiments in [77]. The already mentioned nuclear magnetic resonance technique enabled the non-destructive measurement of crystallization pattern. These systems may represent a porous medium with bimodal pore size distribution and layered structure. Using plaster in combination with Bentheimer sandstone located the small pores at the evaporating side. It is reported that, in this case, the

majority of salt crystals were formed at the surface or within the plaster layer. On the other hand, in a plaster/calcium-silicate brick system (smaller pores located in the substrate) although some salt crystallized in the plaster layer, a significant amount of crystals was found within the brick. In order to quantify the amount of salt transport from the substrate to the plaster, an efficiency number was introduced which was believed to be obtainable from the pore size distribution (different for every salt). Similarly, the influence of paints on drying behavior and salt crystals distribution in the plaster/substrate system and stone specimens was studied by means of magnetic resonance imaging in [29]. It was observed that coating the material with paints may have various effects depending on the system so that the results were more complicated than expected. It was confirmed that paints, in general, tend to hinder evaporation from the samples, which is mainly due to the blockage of some surface pores and reduction of the available evaporation area. This effect should theoretically lead to much slower drying rate, effectively limiting viscous resistance and consequently increasing the amount of liquid transported to the surface by capillary pumping. The outcome of this effect would be an extended first drying period as long as the bulk of liquid in the porous material is not disconnected from the surface. Generally, salt crystals are formed at the evaporating zones (where the highest salt concentration is achieved), therefore a higher amount of efflorescence may be expected when drying painted samples as compared to those without paint. However, this was not always the case as other properties of the system, such as hydrophobicity of the plaster, may influence the rate of moisture transport through the plaster (and paint) towards the outer surface. For example, in the case of a hydrophobic plaster (Parlumire) the results were, first of all, similar for both painted and unpainted systems; secondly, a major crystallization zone was identified at the substrate-plaster interface. Another important effect is the influence of different types of salts on crystallization behavior. It has been observed that a painted plaster acted as salt-transporting (efflorescence) when contaminated by NaCl whereas the same plaster saturated with Na_2SO_4 solution functioned as a salt-accumulating layer (subflorescence). This effect has been explained as being mainly due to significant reduction of equilibrium relative humidity (vapor pressure) by NaCl which slows down the evaporation rate thus extending the CRP.

The effect of dissolved salt on the drying of fired-clay brick and Granada limestone was investigated experimentally with the aim of minimizing the damage induced due to crystallization in [31]. To this goal, experiments were conducted with NaCl solution in the presence and absence of crystallization inhibitors (ferrocyanide). The role of these inhibitors is to delay crystallization by prohibiting the nucleation process, leading to a higher degree of supersaturation before crystallization. The results

were satisfactory as the mass fraction of (nondestructive) efflorescence formed in the presence of inhibitors was dramatically higher compared to the case of only NaCl solution. Reduction of evaporation rate due to blockage of surface pores by efflorescence was only observed in the case of fired-clay bricks. This can be attributed to the significantly smaller mean pore size. This effect was not observed in similar experiments, where the solution is accompanied by inhibitors due to alteration of the crystals' shape and pattern as shown in Figure 2.1. Note that the crystal phase in Figure 2.1 (b) is very porous therefore having minuscule hindering effect on the drying from surface.

Figure 2.1: NaCl crystals formed at the surface of porous medium: (a) without inhibitors and (b) with inhibitors (adopted from [31]).

Moreover, the dynamics of salt crystallization during the drying of porous media was investigated experimentally by a packing of sand grains saturated with NaCl solution in [74]. The results were obtained by high resolution X-ray microtomography and scanning electron microscopy. The dependency of efflorescence formation on the spatial distribution of pore sizes was demonstrated in these results. Salt crystals tend to form at finer pores that contribute to evaporation at the surface of the medium as they stay wet for a longer period of time. This effect also implies that the common macroscopic advection-diffusion equation cannot provide accurate predictions for this problem due to lack of information concerning the heterogeneity of porous substrates.

The effects of salt concentration on the evaporation from porous media and on the dynamics of salt deposition at the surface were investigated both numerically and experimentally in [73]. The effect of activity coefficient (depending on salt concentration) on the evaporation rate, governed by modified Raoult's law [96] was investigated. It has been demonstrated that evaporation rate decreases as the salt concentration is increased only to a certain value; from this point on, any further increase in the salt concentration leads to enhancement of the evaporation rate. The

onset of efflorescence for different salt concentrations was calculated by solving the advection-diffusion equation numerically. Simulation results were found to be in close agreement with experiments conducted using a column filled with sand grains. Also, salt precipitation rate was determined experimentally by image analysis, showing that the coverage rate of the evaporating surface can be approximated by a Gaussian distribution function.

The final distribution pattern of solid precipitates that result from an impregnation process is of utmost importance in industrial applications. The influence of pore size distribution, drying conditions, and initial concentration on final solid distribution in porous media has been investigated by microtomography in [10]. In that work, it has been demonstrated that slow drying leads to significant amount of efflorescence whereas high drying rate leads to a rather uniform salt distribution at the end of the process. Moreover, it was shown that a narrow pore size distribution leads to a more uniform crystallization pattern. And last but not least, high initial salt concentration produces a significant amount of efflorescence compared to a rather homogeneous crystal distribution resulting at low initial concentration. It is well evident that the final crystallization pattern is dependent on many factors such as capillarity, connectivity of liquid, and diffusion rate. The experimental results were then compared to simulations by a new pore network model [86] and results showed good qualitative agreement.

As with other phenomena involving porous media, there are generally two approaches to modeling crystallization in porous media namely: continuous and discrete. The former has been adopted much earlier whereas pore network modeling as the main discrete approach has only been utilized in the last decade. In the following several models of both types are reviewed to establish a basic understanding of their capabilities.

Solute transport in porous media has been modeled for a brine and rock system in [35]. The unique characteristic of brine was its high concentration compared to general cases involving groundwater. This high concentration necessitates coupling of Darcy's and Fick's law due to the effect of solute on fluid motion. Two distinct methods for solving the system of finite difference equations were utilized, one of which involved a quasi-linearization and was proved to be more efficient. Similarly, non-linear boundary conditions are generally present in such problems, therefore, the linearization procedure was applied again. However, this model did not provide any consideration of crystallization/precipitation.

Advection and diffusion of ions during the first drying period have been modeled by a continuum approach in [37]. Note that in that work, formation of salt crystals

was neglected. The presence of three different regimes was identified according to the Péclet number at the evaporating surface. It was demonstrated that for $Pe \gg 1$ advection dominates the process and the concentration of ions at the surface increases significantly faster than in the bulk of liquid in the medium. On the contrary, low values of Pe ($Pe \ll 1$) lead to high diffusion in the system. As a result, ions are distributed uniformly in the liquid and it is speculated that crystallization might happen simultaneously at the surface and the interior. Crossover behavior is expected for $Pe \approx 1$. The problem was solved numerically and analytically for various drying rates. The insight provided by this model paved the way for experimental studies using the nuclear magnetic resonance technique to determine ion and crystal distribution during the process [76].

The mentioned model of Huinink et al. [37] was adopted and extended for symmetrical geometries and arbitrary shape objects in [30]. The solution proposed by Guglielmini et al. [30] focuses on intermediate drying rates where both diffusion and advection play a role in ion distribution. Initially, a numerical solution has been presented followed by an analytical solution for high Pe, cylindrical and spherical coordinate systems and, ultimately, arbitrary geometries. It has been concluded that this model can serve to predict the onset of efflorescence with respect to drying rate and general information about the solution and the porous medium. However, it is worth mentioning that this (and the previous) model only consider the constant drying rate period or, in other words, saturation of the porous medium is not varied in the proposed solutions.

Another continuum approach to ion transport and crystallization in porous media has been proposed in the framework of the finite element method [32]. Salt crystallization has been modeled within the theory of poromechanics [14]. The respective model is quite comprehensive and considers the dependency of crystallization on supersaturation, pore radii, and relative humidity. Additionally, the effect of crystallization on pore size distribution has been taken into account [11]. Experiments on hydrophobated calcium silicate samples, in which specimens were saturated with salt solution and then dried, validated the respective model.

Drying of porous media in the presence of sucrose solution was modeled using a pore network approach in [90]. In that model, the effect of dissolved sucrose on drying pattern was considered through physical properties such as liquid viscosity, vapor pressure, and surface tension. It is noteworthy that the main mechanism for ion transport in the model of [90] was diffusion. Ion concentration gradients were established by so-called Haines jumps, which transported significant amounts of salt to the drying front, and back diffusion was assumed to occur with respect

to these concentration gradients. It was assumed that hydraulic connectivity is maintained in the network, as a pseudo-film effect has been accounted for. However, ion diffusion through these films was assumed to be insignificant. Drying curves were compared for the case of drying of pure water to that of sucrose solution in simulations with identical networks. Interestingly, a slight enhancement of the drying rate was observed in simulations with sucrose solution. More simulation results in the form of liquid-gas phase distribution were presented. It was shown that the phase distribution of liquid and gas may considerably differ from one to the other case (pure water and sucrose solution). It is worth mentioning that this model lacks any consideration of crystallization, which may be seen as one of its shortcomings.

The formation of efflorescence during drying of a packed column placed inside a hollow cylinder has been studied experimentally and by a pore network model in [108]. NaCl solution was constantly supplied to the packing from the bottom side and the medium was exposed to controlled evaporation from the top. The height of the cylinder determined the thickness of the gas boundary layer as there was a distance between the surface of the packing and the top of the cylinder. Results show crystals forming at certain spots at the surface, generally with a gap in between, where no crystallization takes place. Experimental results for various boundary layer thicknesses show a clear dependency between efflorescence formation pattern and boundary layer thickness, as illustrated in Figure 2.2. Very similar results (qualitatively) have been acquired from pore network simulations. An important effect which could be captured by this model is the change in capillary flow induced by the formation of porous efflorescence. As a result, liquid flow rate in surface pores connected to the efflorescence is enhanced at the expense of a reduction in regions farther away. The direct consequence of this phenomenon is the continuous growth of crystals in certain zones where they have initially been formed. Simultaneously, it has been attempted to develop a continuous model to the same problem [109]. This model was based on a classical continuum approach to porous media [5]. The model was solved in a one-dimensional coordinate system as well as in cylindrical coordinates. In the end, it has been concluded that such continuous models are incapable of explaining the major finding of the experiments that have been confirmed by the pore network simulations, namely the discrete distribution of crystallization sites. One caveat to the utility of this system (to represent drying of porous media) is that due to constant supply of liquid to the packing, the whole medium stays completely saturated during the course of the experiments or the simulations. Therefore many important effects, which are innate to drying of porous media, have not been accounted for (e.g. liquid clustering and connectivity loss).

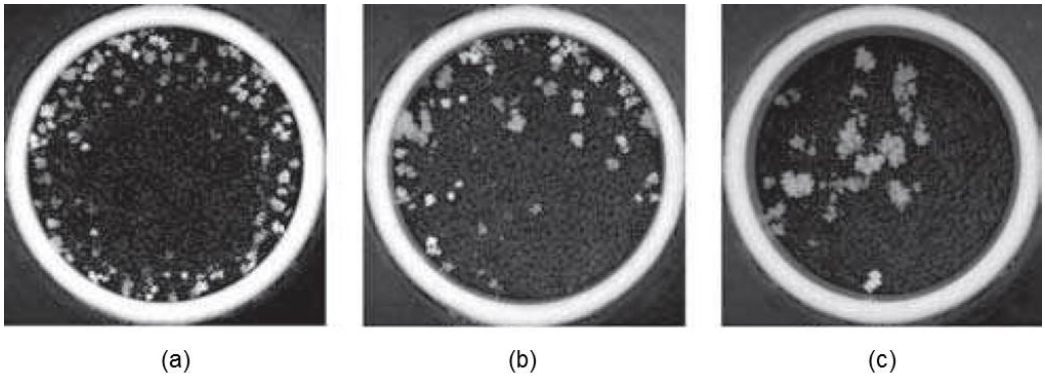

Figure 2.2: Efflorescence formation for wicking experiments with NaCl solution for boundary layer thicknesses of: (a) 2.5 mm, (b) 7.5 mm, and (c) 15 mm. (adopted from [108])

We can recapitulate important points of this review as follows:

• **Application:** Salt crystallization in porous media is an important phenomenon which has many applications. Most of the research in this area has been focused on preventing or delaying destructive crystallization which usually happens in the interior. However, this process also has several industrial applications, the most important of which is impregnation of porous solids.

• **Experiments:** Various experiments have been conducted to provide good understanding of the process. The effects of many variables have been investigated such as variation of drying rate due to solute concentration or the influence of pore size distribution on crystallization pattern. The most important finding is that the competition between capillary flow, ion diffusion, and liquid connectivity in the medium defines the final crystal distribution. Experimental results are typically obtained by an imaging method, such as X-ray microtomography or magnetic resonance imaging.

• **Continuous models:** Traditionally, continuum approaches are used for modeling porous media in this scenario. In the majority of cases, numerical solutions to specific problems have been proposed. However, within narrowly set conditions and simplifying assumptions, few analytical solutions have also been presented. However, the typical criticism to continuous models, i.e. lack of enough details regarding the micro-structure, applies to even a higher degree here. It is shown that the final crystallization pattern is strongly dependent on the intricacies of porous substrates, which may not be captured by continuous models.

• **Pore network models:** Several attempts have been made to describe crystallization in porous media by the discrete pore network approach. The results and

conclusions have so far been positive. However, these models are applicable only to certain cases and the results cannot be generalized albeit they look very promising.

Considering the numerous efforts at modeling of drying porous media in the presence of dissolved salt, lack of a model that can track ion transport by advective capillary flow and diffusion in real time is evident. As mentioned before, pore network models are precious tools to study this process by providing detailed insight into pore-scale phenomena. In this thesis, we aim to incorporate ion transport and crystallization into preexisting pore network models. Several modifications to the pore network models proved essential in this endeavor.

The remainder of this chapter focuses on a fully saturated network with uniform initial salt concentration.

2.2 Model description

This section provides a thorough description of the developed model for impregnation of porous materials. At first, the pore network drying model is briefly introduced (Section 2.2.1). Later on in Section 2.2.2, dissolved salt is incorporated and the ion transport rules are explained. Numerical accuracy of the model will be assessed by comparison with the analytical solutions of a well-known problem. This model is utilized in the subsequent Section 2.3 to investigate the effects of variation of some parameters on crystallization patterns.

2.2.1 Pore network drying model

In this chapter, we aim to approximate the void space of a porous material by a 2D square network. This pore network model consists of two different types of structural elements, namely cylindrical throats and volumeless nodes. The volume of liquid inside the medium is located within cylindrical throats that are positioned perpendicularly to one another in vertical and horizontal orientations. The connection between throats is established via nodes with no volume. These nodes provide the computational grid required for vapor and liquid pressure, and ion transport calculation. A schematic view of such a network is shown at an intermediate drying stage in Figure 2.3.

Drying is considered only from the top, whereas all other sides of the network are sealed. As a result, the vapor transport out of the network takes place via a diffusive boundary layer at the surface. This boundary layer has also been discretized into

square elements connecting neighboring nodes. The liquid and vapor flow in the entire network are considered quasi-stationary within the global time-steps.

For the sake of simplicity, several assumptions regarding the salt solution have been made which are mentioned here. Firstly, all colligative properties of salt solutions are neglected, i.e. concentration variation has no effect on the physical properties of the solution. This leads to the variation of several physical properties of the liquid to be neglected throughout the entire simulation such as liquid-gas surface tension, vapor pressure at the interface, liquid viscosity, etc. Furthermore, the volume of salt crystals has not been taken into account. This implies that all the respective effects such as variation of pore size distribution or blockage of the pores are neglected. Finally, all thermal and film effects, as well as adsorption of ions at the solid wall have also been neglected.

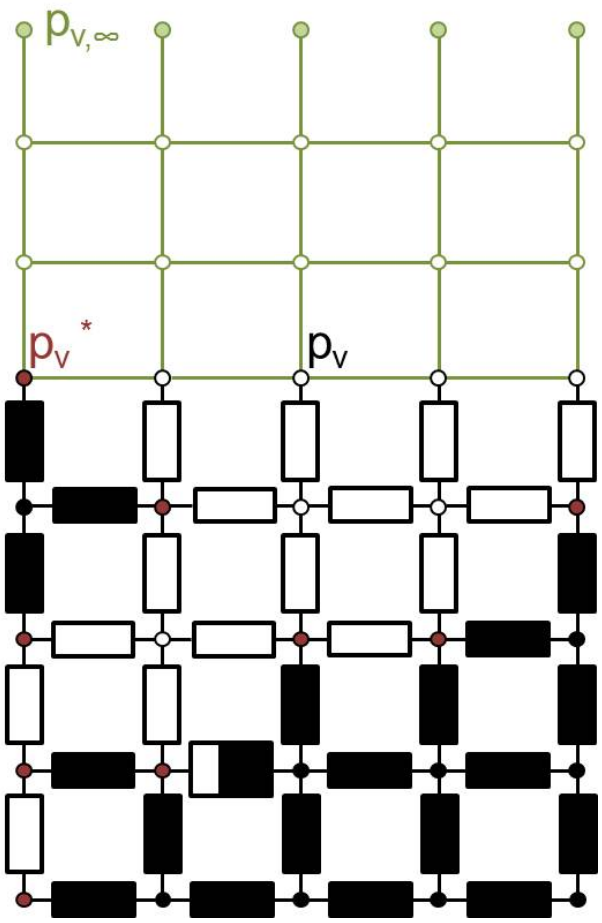

Figure 2.3: Schematic representation of the pore network model with boundary layer.

Several cases are possible regarding the saturation state of nodes and throats. Throat saturation changes as drying progresses. As soon as one throat has emptied (white

color in Figure 2.3) the meniscus recedes into the neighboring throats that contain liquid (black color in Figure 2.3). Throats may also be partly full, which represent a transient state meaning that they will either be filled or emptied in the future time-steps. The connection between throats is established via nodes, whose saturation state is dictated by their neighboring throats. A node is considered at liquid state as long as all its neighboring throats contain liquid (black color in Figure 2.3). The saturation state of the node changes to gas the very moment one of the neighboring throats depletes. However, so long as these neighboring throats contain any amount of liquid, the vapor pressure at the respective gas node is considered to be saturation vapor pressure (p_v^*, red color in Figure 2.3). Finally, the vapor pressure of a node becomes unknown (calculation procedure presented later) as soon as all neighboring throats have dried out (white color in Figure 2.3).

Vapor diffusion in the gas-filled part of the network and in the boundary layer is calculated by Stefan's law coupled with isothermal conditions in the entire system. This equation for a given throat ij (connecting nodes i and j) can be written as follows:

$$\dot{M}_{v,ij} = A_{ij}\frac{\delta}{L_{ij}}\frac{P\tilde{M}_v}{\tilde{R}T}\ln\Big(\frac{P-p_{v,j}}{P-p_{v,i}}\Big), \tag{2.1}$$

where δ is the binary diffusion coefficient between liquid vapor and air, A_{ij} and L_{ij} throat cross-sectional area and length respectively, P total gas pressure, T gas temperature, $\tilde{M}_v$ molar mass of the liquid, $\tilde{R}$ universal gas constant, and p_v partial pressure of the vapor in the gas phase. It is clear that usage of this equation for vapor flow calculations in the system requires complete knowledge of the vapor pressure field. As explained in the previous paragraph the nodes in direct neighborhood of liquid are considered at saturation vapor pressure (red in Figure 2.3). The rest of the gas nodes in the network and all the nodes in the boundary layer have unknown vapor pressure. Hence, Equation 2.1 is utilized to write the mass conservation equation at every gas node in the system as follows:

$$\sum_k \dot{M}_{v,ik} = \sum_k g_{v,ik}\ln\Big(\frac{P-p_{v,k}}{P-p_{v,i}}\Big) = 0, \tag{2.2}$$

where k changes over adjacent nodes to node i and gas conductance in each throat is denoted by g_v. Such a mass balance equation is to be written for every node with unknown vapor pressure, which produces a system of algebraic equations. The boundary conditions vector ($\mathbf{b_v}$) to this system of equations consists of nodes with saturation vapor pressure (p_v^*) and the vapor pressure at the top of the boundary layer ($p_{v,\infty}$, corresponding to ambient air relative humidity). The matrix multiplication looks as follows:

$$\mathbf{A_v} \times \ln(1 - \frac{\mathbf{p_v}}{\mathbf{P}}) = \mathbf{b_v} \Rightarrow \mathbf{p_v} = \mathbf{P}(1 - \exp(\mathbf{A_v^{-1}} \times \mathbf{b_v})). \tag{2.3}$$

In the above equation, the $\mathbf{A_v}$ matrix contains all the relevant gas conductances between nodes with unknown vapor pressure.

Liquid capillary-viscous flow within liquid clusters in the network is governed by the Hagen-Poiseuille equation (Equation 2.4). Due to pore size distribution in the network various pressure levels are held by menisci within the throats. Quasi-stationary conditions result in an instantaneous build up of pressure gradient at the beginning of each global time-step (defined later). However, in order to obtain liquid pressure at various nodes in the network, which are essential for Equation 2.4, a similar procedure as to vapor pressure field calculation shall be followed. Initially, the mass conservation law is held at every liquid pore in the network:

$$\Delta P = \frac{8\mu LQ}{\pi r^4}, \tag{2.4}$$

$$\sum_k \dot{M}_{w,ik} = \sum_k g_{w,ik}(P_{w,k} - P_{w,i}) = 0, \tag{2.5}$$

where g_w is the liquid conductance for each throat in the network. Stacking such equations for every liquid pore leads to the second system of algebraic equations whose solution provides the liquid pressure field. However, acquiring the boundary conditions for this system of equations is not as straightforward as in the previous case. These boundary conditions are defined at menisci. Two scenarios are possible here:

1. Stationary menisci: A meniscus located at the entrance of a throat (full throat) is generally stationary. According to the extent of viscous effect, various number of menisci per liquid cluster may be stationary. The curvature of stationary menisci varies depending on the balance of pressure (influenced by evaporation). Therefore, calculating liquid pressure at the interface is not an easy task. Nevertheless, the fact that a meniscus, which is exposed to evaporation, is stationary indicates no net accumulation of liquid. In other words, the entire evaporation mass is supplied by liquid flow to the throat. To put this picture in the context of liquid pressure, the curvature adjusts in order to pump enough liquid to compensate the evaporative loss.

2. Moving menisci: In the context of drying, generally moving menisci are perceived to be receding. Since liquid is lost by evaporation, capillary flow is responsible

to pump the liquid from locations with higher liquid pressure (larger throats) to the evaporation sites. Once again depending on the viscous effect one or several menisci may be receding to supply enough liquid for evaporation. However, due to the time-discretized nature of the model sometimes a receding meniscus may change to an advancing one within consecutive time-steps, e.g. if new menisci are formed in larger throats. We assume that a moving meniscus will always maintain the minimum contact angle (regardless of receding/advancing state). As a result, the pressure level at these menisci can always be calculated from the Young-Laplace equation presented in Section 1.2 as Equation 1.2, given nearby gas pressure (P_g):

$$P_l = P_g - P_c = P_g - \frac{2\sigma}{r} cos\theta. \tag{2.6}$$

The two different states introduced for menisci relate to the two types of boundary conditions for the system of equations acquired from Equation 2.5. Stationary menisci directly provide information regarding the incoming liquid flow rate whereas for moving menisci, the liquid pressure level at the interface is assigned as the boundary condition. However, viscosity of the liquid causes resistance in liquid flow between the throats. Consequently, in some cases, depending on various factors, sufficient liquid flow from a single throat (the largest one) cannot be provided to every location in the respective cluster. This implies that the state of menisci cannot be merely asserted and is to be identified. Metzger et al. [66] have presented two algorithms via which the state of menisci is found. In this model we adopt algorithm (a) from [66], a synopsis will be presented after liquid pressure calculation has been explained. Similarly to the gas phase, stacking mass conservation equations for individual liquid pores provides a system of algebraic equations. This system of equations is solved for the nodal pressures $P_{w,i}$ offering the liquid pressure field as follows:

$$\mathbf{A_w} \times \mathbf{P_w} = \mathbf{b_w} \Rightarrow \mathbf{P_w} = \mathbf{A_w^{-1}} \times \mathbf{b_w}, \tag{2.7}$$

where all the relevant liquid conductances are stored in matrix A_w. As an example this system of equations is expanded as follows:

$$\begin{bmatrix} P_{w,1} \\ P_{w,2} \\ \vdots \\ P_{w,Np} \end{bmatrix} = \begin{bmatrix} A^{-1}_{w,1,1} & A^{-1}_{w,1,2} & \dots & A^{-1}_{w,1,Np} \\ A^{-1}_{w,2,1} & A^{-1}_{w,2,2} & \dots & A^{-1}_{w,2,Np} \\ \vdots & \vdots & \ddots & \vdots \\ A^{-1}_{w,Np,1} & A^{-1}_{w,Np,2} & \dots & A^{-1}_{w,Np,Np} \end{bmatrix} \times \begin{bmatrix} b_{w,1} \\ b_{w,2} \\ \vdots \\ b_{w,Np} \end{bmatrix} \tag{2.8}$$

These two systems of equations are solved by a direct solver (the "backslash" command) in "Matlab 2013".

After the liquid pressure has been obtained it needs to be verified whether the assumptions regarding menisci and consequently boundary conditions hold up. Initially, it is assumed that all menisci except the ones at the largest, as well as party filled, throats of each cluster are stationary. Once the liquid pressure field has been calculated, the pressure difference between the adjacent nodes and the lowest possible pressure at menisci (given by Equation 1.2) is compared to the amount required to maintain evaporation at corresponding menisci. In case there are one or several menisci for which this pressure difference is not sufficient, the one with the maximum deficit has to change its state to receding. As a result, new boundary conditions are implemented in the system of equations and the liquid pressure field is recalculated. This procedure continues until no stationary meniscus has a deficit of liquid flow versus the evaporation loss.

As briefly mentioned at the beginning of Section 2.2.1, a quasi-stationary approach is adopted for the liquid and vapor flow during each global time-step. Such time-steps are defined as the time needed for at least one boundary condition to change. To further clarify: as the next meniscus fills or empties the corresponding throat, the vapor and liquid pressure fields should be recalculated. Said required time is denoted as the global time-step in the network. These time-steps are unique and depend on many factors, most important of which is the liquid and vapor phase distribution in the network.

It is important to mention that in this model liquid migration into already dried regions of the network is prohibited; the liquid may flow within one cluster but as soon as a throat has been emptied it will stay dry for the entire simulation. This is extremely important later on in Section 2.2.3 since this assumption leads to the constant mass of salt crystals within a throat as soon as it has been depleted.

2.2.2 Salt migration model

Salt migration is modeled by simultaneous advection and diffusion of ions in the liquid phase. Dissolved salt is transported by liquid capillary flow in the throats defining the advection term. Advection is modeled by plug flow in each throat which simplifies the problem: ion transport can be reduced into a one-dimensional equation, neglecting dispersion of ions in the radial direction. At the same time, this transportation leads to the establishment of concentration gradient by accumulation and consequently back-diffusion of the ions in the liquid phase.

The concentration of salt in each throat is tracked considering a 1D transient advection-diffusion equation. This equation for an infinitesimal length of a throat (dz) can be

written as follows:

$$\frac{\partial(CV)}{\partial t}|_z = (uAC)|_z - (uAC)|_{z+dz} + \frac{\partial(DAC)}{\partial(z)}|_z - \frac{\partial(DAC)}{\partial(z)}|_{z+dz}, \tag{2.9}$$

where V and A are volume and cross-sectional area of the element respectively, and u represents the flow velocity of liquid. Since the geometry of the throats is cylindrical (constant cross-sectional area), the volume of the element can be calculated as the product of length and cross-sectional area ($A \times dz$). Moreover, considering this geometry and the assumption of constant binary diffusion coefficient, Equation 2.9 can be transformed to the form:

$$\frac{\partial C}{\partial t} = -u\frac{\partial C}{\partial z} + D\frac{\partial^2 C}{\partial z^2}. \tag{2.10}$$

Equation 2.10 can be solved analytically for particular boundary conditions. However, in this network model, analytical solution of this equation is either not possible or leads to a polynomial series which is not desirable. Hence, considering the throat geometry, this equation is discretized in the Cartesian domain using throats as computational elements (Figure 2.4). Having the concept of the finite volume method in mind, each throat is represented by one uniform concentration. The governing equation for a throat of length L_k between the nodes i and j is:

$$\frac{dC_k}{dt} = u\frac{C_i - C_k}{L_k} + \frac{2D}{L_k}\Big(\frac{C_j - 2C_k + C_i}{L_k}\Big). \tag{2.11}$$

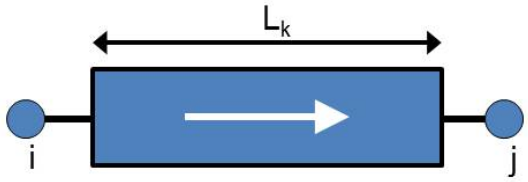

Figure 2.4: Schematic view of throat k and pores i and j subject to plug flow.

As discussed before, in the pore network drying model the nodes do not have any volume and only serve as computational grid for the liquid and vapor pressure fields. In calculations regarding salt migration, a similar role for the nodes is considered. The concentration at the nodes is calculated considering perfect mixing of the incoming liquid from different throats in addition to the diffusion effect between the pore and all the neighboring throats. For example, salt concentration at node i from

Figure 2.5 would be:

$$C_i = \frac{\sum_{k=1}^{2} u_k A_k C_k + \sum_{j=1}^{4} 2D\frac{A_j C_j}{L_j}}{\sum_{l=3}^{4} u_l A_l + \sum_{j=1}^{4} 2D\frac{A_j}{L_j}}. \tag{2.12}$$

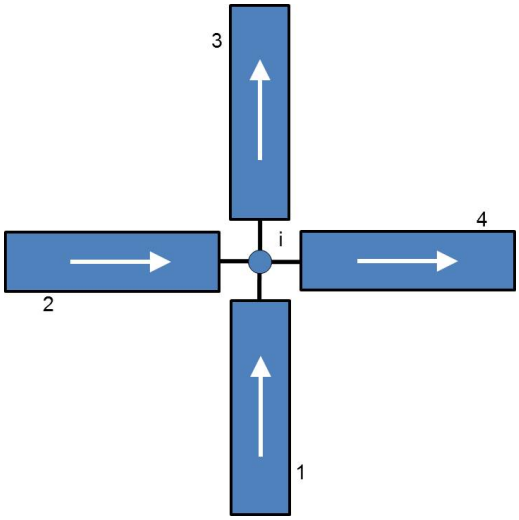

Figure 2.5: Schematic view of pore i and the neighboring throats with flow directions.

The fact that in this network geometry, nodes do not have any volume, raises the question of how to select the diffusion length. In Equation 2.11, $\frac{L_k}{2}$ is considered as the diffusion length, which is confirmed in Section 2.2.4 by a test problem.

An important consideration with regards to Equation 2.11 is the solution approach. In the entirety of this thesis we utilize an explicit solution scheme to solve the time-varying salt concentration equations. The crucial part of an explicit scheme is time-step determination, since the result could become unstable for time-steps larger than given by stability criteria. Such upper limits can be calculated separately for advection and diffusion, considering throat geometry, as follows:

$$\Delta t_{adv} \leq \frac{L}{u}, \tag{2.13}$$

$$\Delta t_{diff} \leq \frac{1}{2}\frac{(\frac{L}{2})^2}{D}. \tag{2.14}$$

Commonly, the values for stability criteria are smaller than the global time-step, hence ion transport calculations ought to be carried out in smaller steps. In this case, the minimum of the two stability criteria is selected and denoted by "salt time-step". The time is incremented using these so-called salt time-steps until a span

corresponding to the global time-step is reached. This action is possible since flow boundary conditions remain constant so long as the global time-step has not been elapsed. Table 2.1 shows a simple example of a full throat that determines the global time-step (emptying in this specific case) where a salt time-step equal to 40 percent of the global time-step is imposed.

Table 2.1: Evolution of throat saturation for salt time-step equal to 0.4 of the global time-step

current throat saturation	salt time-step	elapsed time	new throat saturation
100%	Δt_{salt}	Δt_{salt}	60%
60%	Δt_{salt}	$2\Delta t_{salt}$	20%
20%	$\Delta t_g - 2\Delta t_{salt}$	Δt_g	0%

Note: One important remark needs to be made regarding the diffusion stability criterion. As per Equation 2.14, the salt time-step is potentially proportional to the square of diffusion length which varies for moving menisci. However, as a meniscus recedes the diffusion stability criterion decreases significantly, which leads to infinite iteration of the ion transport calculation loop. To tackle this issue, we set a lower limit (in simulations of this thesis 10% throat saturation) below which any diffusion concerning the corresponding throat will be neglected. Therefore advection takes over and generally, the throats deplete in the next salt time-step.

2.2.3 Crystallization

Drying of salt solutions causes solvent evaporation which inevitably leads to crystallization as drying goes on sufficiently long. In this model, a certain degree of supersaturation is defined which serves as the limit before crystallization is initiated ($\frac{C^*+C_\epsilon}{C^*}$). Ions are tracked with respect to the salt time-step and the new concentration profile in the network is achieved; at which point salt concentration is compared to the supersaturation level defined earlier and the excess salt is crystallized in the corresponding throat. Note that we assume crystallization to continue to a point slightly below the saturation concentration (same amount as defined by supersaturation degree as deficit). The mass of crystallized salt and the new ion concentration are calculated as follows:

$$M_{salt,k}^{new} = M_{salt,k}^{old} + V_k(C_k - (C^* - C_\epsilon)), \tag{2.15}$$

$$C_k^{new} = C^* - C_\epsilon. \tag{2.16}$$

It is worth mentioning that the kinetics of crystallization has been neglected thoroughly and we treat crystallization as a thermodynamic phenomenon in this model. This assumption could be reasonable for most cases as drying time-scales are generally longer than that of crystal growth.

The entire algorithm regarding salt migration and crystallization will be recapitulated here. The aim is to track salt concentration within the throats while accounting for possible crystallization when salt concentration surpasses the limit. Initially, nodal concentrations are defined using Equation 2.12 at every liquid pore in the network, which can be done by simple matrix multiplication:

$$\mathbf{C_{nodal}} = \mathbf{A_{nodal}} \times \mathbf{C_{throat}}. \tag{2.17}$$

In Equation 2.17, the matrix $\mathbf{A_{nodal}}$ represent relevant advective and diffusive contributions from adjacent throats (obtained from Equation 2.12). This step is followed by a secondary matrix multiplication, taking into account the salt time-step, which provides throat concentration as a function of nodal concentration (incorporating Equation 2.11). This step utilizes the concept of explicit solution scheme as follows:

$$C_{throat}^{new} = C_{throat}^{old} + A_c \times C_{nodal}^{old} \Delta t_{salt}, \tag{2.18}$$

or in expanded form:

$$\begin{bmatrix} C_{throat,1}^{new} \\ C_{throat,2}^{new} \\ \vdots \\ C_{throat,Nt}^{new} \end{bmatrix} = \begin{bmatrix} C_{throat,1}^{old} \\ C_{throat,2}^{old} \\ \vdots \\ C_{throat,Nt}^{old} \end{bmatrix} + \begin{bmatrix} A_{c,1,1} & A_{c,1,2} & \dots & A_{c,1,Np} \\ A_{c,2,1} & A_{c,2,2} & \dots & A_{c,2,Np} \\ \vdots & \vdots & \ddots & \vdots \\ A_{c,Np,1} & A_{c,Np,2} & \dots & A_{c,Np,Np} \end{bmatrix} \times \begin{bmatrix} C_{nodal,1}^{old} \\ C_{nodal,2}^{old} \\ \vdots \\ C_{nodal,Nt}^{old} \end{bmatrix} \Delta t_{salt}. \tag{2.19}$$

Note: It is of utmost importance to keep in mind that if the volume of liquid in a throat is to be varied (a throat with a moving meniscus), the salt concentration acquired for these throats should be adjusted to the current volume of liquid:

$$C_{throat}^{current} = C_{throat}^{new} \frac{V_{throat}^{old}}{V_{throat}^{current}}. \tag{2.20}$$

Equation 2.20 is required due to the decoupling of ion transport and liquid motion.

Finally, crystallization is considered in throats whose concentration exceeds the supersaturation limit as shown by Equation 2.15. Depending on the values of salt

and global time-steps, such a sequence of calculations needs to be repeated until the elapsed time equals the global time-step. Keep in mind that liquid flow rate in the network is calculated before salt calculations are carried out and it remains constant until the end of the global time-step.

2.2.4 Numerical validation of the model

As briefly mentioned in Section 2.2.2, the diffusion length selected to transform Equation 2.10 to Equation 2.11 needs to be validated. To this goal, a test problem is established as follows: a long capillary, with respective length and radius of 1 mm and 1 μm, which is exposed to evaporation is connected to a reservoir from the opposite side. Initially, salt concentration in the entire system is considered uniform. This problem has been solved by the finite volume method to obtain the salt concentration profile in the capillary. The solution is then compared to the results of a pore network simulation which replicates this problem. In this simulation aqueous NaCl solution with 10 % initial saturation at 25 $^{\circ}C$ is considered (see Table A.1 for the physical properties of the materials). A schematic view of the problem is presented in Figure 2.6.

Figure 2.6: Schematic presentation of the first test problem of a capillary connected to a reservoir and open to evaporation.

The problem is solved by discretizing the capillary into 100 elements (excluding the reservoir) with the finite volume method (FVM). In order to simplify the boundary conditions, the diffusion of salt at the left boundary (entrance of the capillary) is neglected, which allows constant flow of salt as the salt concentration in the reservoir remains unchanged. The volume of liquid in the capillary is constant as all the evaporation is compensated by capillary pumping from the reservoir. Said evaporation rate is initially calculated from the PNM, using a boundary layer with a thickness equal to the capillary, and then fed into the finite volume method as the boundary condition. The ambient air is considered to be completely dry ($p_{v,\infty} = 0$). On the other hand, the problem is modeled by the throat-node pore network geometry considering 100 throats of uniform size (1 μm, equal to the number of elements in

FVM solution) connected to a large throat with the radius of 100 μm serving as the reservoir in the system (Figure 2.7).

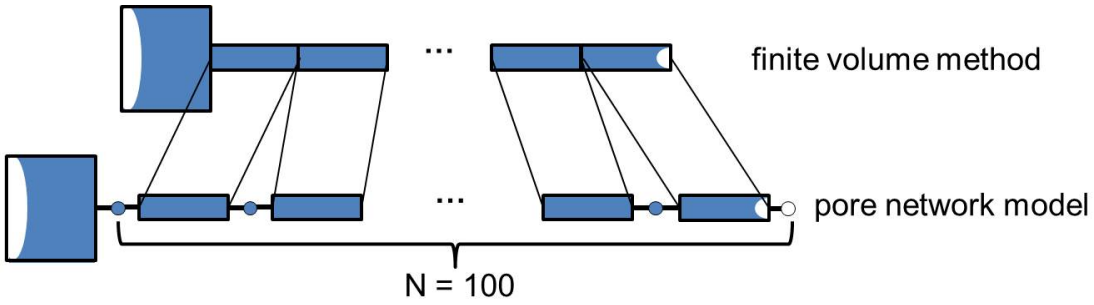

Figure 2.7: Analogy of finite volume method and pore network model of test problem 1.

Before looking into the salt concentration profiles over time for the two cases it should be pointed out that the trend regarding the results is predictable. Due to constant flow of salt (alongside liquid), salt concentration at the right hand side (open side) should increase. This induced concentration gradient acts as the driving force for ion back-diffusion in the direction of the reservoir. Thus, as time goes by salt concentration in elements (throats) towards the right hand side will be elevated. Salt concentration profiles during the course of the simulation are shown in Figure 2.8 where the trends clearly match the expectations.

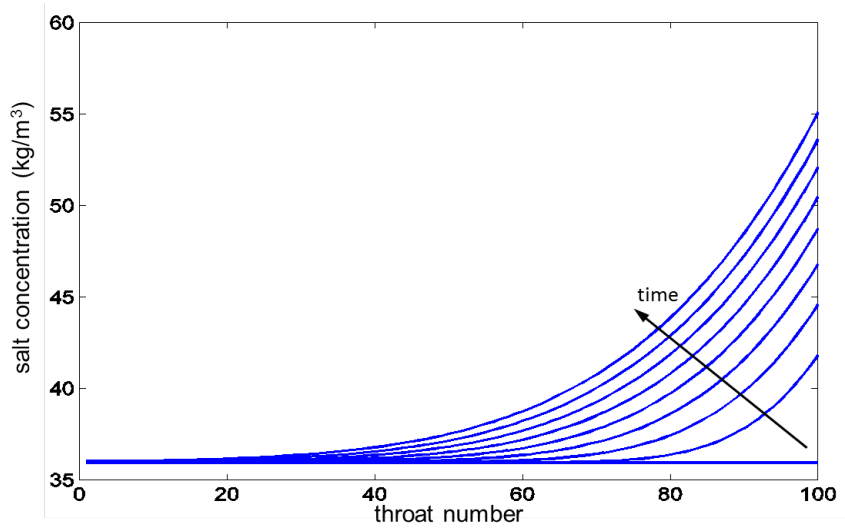

Figure 2.8: Concentration profiles over time for pore network simulation results for test problem 1. The profiles are plotted at time increments of 1000 s.

The concentration profile at the end of the simulation is compared to the solution obtained by finite volume method. The results can be mapped perfectly to one

another indicating that the two solutions are basically identical hence confirming the validity of Equation 2.11 (Figure 2.9).

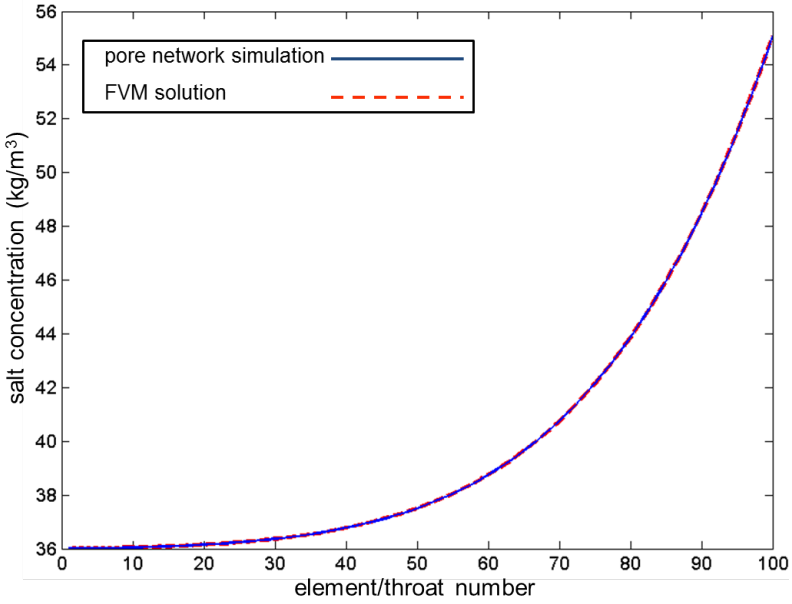

Figure 2.9: Comparison of final results from finite volume method (dashed red) and pore network simulations (solid blue) for test problem 1.

Despite the agreement of the results shown in Figure 2.9, the knowledge acquired cannot be translated to the numerical accuracy of the model. This can be clarified by the fact that both solutions depend highly on the discretization level (size of the elements), thus the finite volume method does not provide a direct measure to the numerical accuracy of the solution. For this purpose, a reference case is required to which the results could be compared. Therefore a second test problem is established for which a well-known analytical solution is available.

2.2.5 Numerical precision of the model

The second test problem is also known as "mass dispersion in a long tube with plug flow". It comprises of an infinitely long tube which is filled with pure water with a constant plug flow. At some moment a known amount of salt mass (M_{salt}) is injected in an infinitesimal length of the tube, resulting in significant rise in salt concentration (also denoted by "Dirac peak"). This point in time marks the beginning of the simulation. This problem can be solved analytically, where a unique function for the concentration of salt over time and space in the form of a Gaussian bell curve is obtained [25]:

$$C(t,z) = \frac{M_{salt}}{A\sqrt{4Dt}} \exp\Big(- \frac{(z-ut)^2}{4Dt} \Big). \tag{2.21}$$

According to Equation 2.21 the peak in salt concentration is displaced in the direction of flow depending on the flow velocity (u). Simultaneously the salt is dispersed which leads to the widening of the profile (shown with dashed red color in Figure 2.10).

This problem has been simulated using pore network geometry by considering a 1D arrangement of 1000 uniform throats, with the radius and length of 1 μm and 100 μm respectively, connected via nodes to represent the long capillary. Salt concentration in all throats is set to zero (pure water) except for the throat that intersects with the position of the Dirac peak at the beginning of the simulation. The concentration in this throat is set at 1000 $\frac{kg}{m^3}$ which considering the volume of the throat translates to ($M_{salt} = 3.14 \times 10^{-13}\ kg$). The liquid flows at a constant velocity of ($u_k = 2\ \frac{mm}{s}$) in the right direction. The results from the pore network simulation and the analytical solution are plotted in the same graph over the course of time in Figure 2.10.

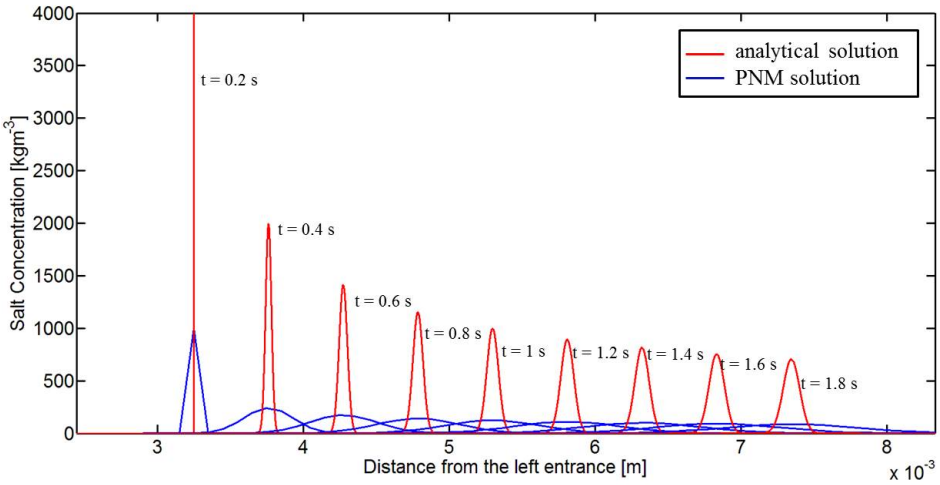

Figure 2.10: Comparison of concentration profiles during mass dispersion in a tube from analytical solution (dashed red) and pore network simulation (solid blue). Squares represent the centers of the throats.

As demonstrated, the agreement between the pore network simulation results and the analytical solution is very poor. This discrepancy is mainly attributed to the over-estimation of diffusion effect which gets more severe for higher values of the local Péclet number (in this case 200) as a function of velocity (u_k), element length (L_k) and diffusion coefficient (D):

$$Pe = \frac{u_k L_k}{D}. \tag{2.22}$$

This over-estimation is anticipated to be caused by two major issues:

• **Diffusion length:** The considerably long diffusion path between nodes and throats combined with high concentration gradients causes the diffusion effect to be more pronounced especially at the beginning of the simulation. This is particularly an issue for combined advection-diffusion problems.

• **Numerical diffusion:** The second reason is the so-called numerical diffusion caused by mixing the whole amount of salt in one element (throat) as salt flows by advection into the new elements with zero salt concentration. This is an intrinsic characteristic of difference-type methods where uniform properties are ascribed to the elements.

However, it needs to be mentioned that salt concentration values in this particular test problem do not reflect the situation in a realistic pore network simulation (or any experiment). To further clarify, in this case, the initial concentration is way above the saturation concentration of most salts in water and it is highly unlikely that this sort of highly concentrated regions and pure solvent coexist in such close proximity. Nevertheless, assessing the numerical accuracy of models generally requires investigation of extreme cases.

As mentioned before the problem is amplified with increasing Pe. Nonetheless, the local Pe number at each computational element can be reduced by decreasing the length of each element (throat). However, varying throat length is typically undesired since the throats are meant to represent the porous medium (with given porosity). Simultaneously shorter throats lead to an increase in their number (to simulate the same size of porous medium) which drastically increases the computational cost. Since this issue only concerns salt-related calculations it was decided to discretize the throats into virtual sub-elements only for those calculations. This theoretically solves the problem of high Pe while leaving the network drying algorithm intact. The concept of the finite volume method is carried over to the sub-divisions, hence uniform concentration is assumed at each sub-element.

To validate this refined model, the results are compared to the same analytical solution as in Figure 2.10. The numerical disparity between the simulation result and the analytical solution (root-mean-square error) falls below 1 % as the throats are discretized to 256 sub-elements (Pe = 0.781) (Figure 2.11).

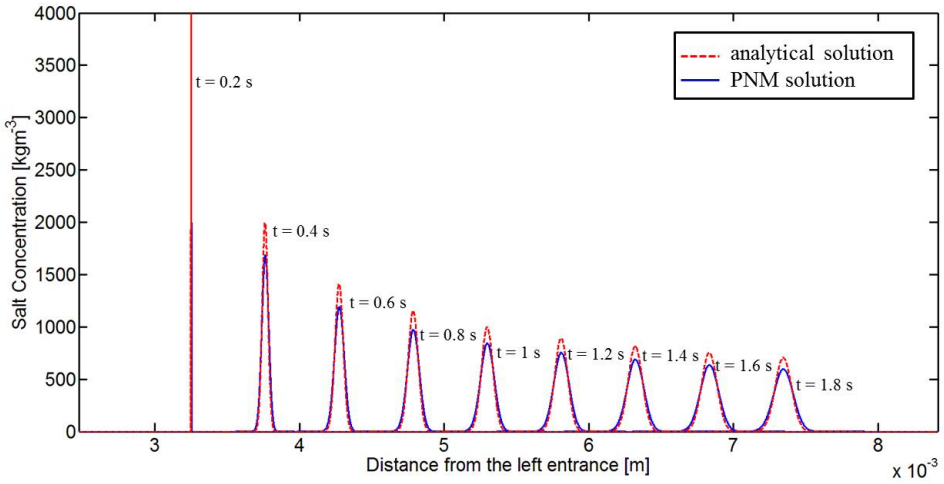

Figure 2.11: Comparison of concentration profiles during mass dispersion in a tube from analytical solution (dashed red) and pore network simulation with refined computational grid (solid blue).

Note: The dependency of numerical error on Pe is evident from the conducted comparison. However, it needs to be mentioned that the numerical error, as defined by Equation 2.23 by means of root mean square error (RMSE),

$$RMSE = \sqrt{\frac{\sum_{i=1}^{n}(C_{analytical} - C_{PNM})^2}{n}}, \tag{2.23}$$

decreases significantly as Pe values approach unity (see Figure 2.12). Further discretization of the computational grid yields diminishing returns and is therefore not justified.

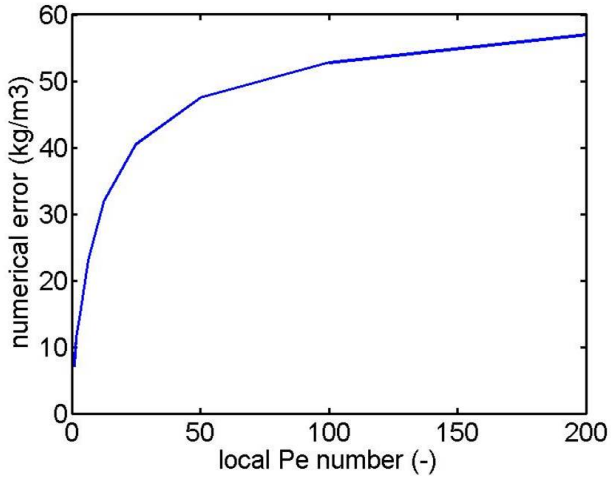

Figure 2.12: Comparison of concentration profiles during mass dispersion in a tube from analytical solution (dashed red) and pore network simulation with refined computational grid (solid blue).

2.2.6 Adaptive throat discretization

In the previous section, it was demonstrated that the numerical error in salt-related calculations is directly correlated with the local value of Pe. Nevertheless, in a pore network simulation of the drying process the sub-discretization should be adaptive based on Pe due to two reasons:

1. Many different factors define Pe in the course of drying. Most importantly, the values of Pe for specific regions constantly vary from one time-step to another. Thus, it is completely unnecessary to discretize the majority of throats in a network, since local Pe might not exceed the threshold when calculated for the entire throat length.

2. Introducing unnecessary elements in the system puts a tax on computational time. It is self-evident that to achieve the highest computational efficiency the number of sub-elements should be minimized.

Both points mentioned above can be addressed by an adaptive discretization scheme. To this goal, a simple rule is established to govern the number of sub-elements at every time-step in each throat. The rule for a specific throat is described as follows: if the local Pe number in the throat is larger than unity, it is discretized so that the Pe number in each element is below unity. However, we define levels for the number of sub-elements as the "powers of two" to avoid arbitrary number of elements within throats. On the other hand, the numerical grid can be coarsened following a similar rule: if the local Pe in one throat drops from a global time-step to another, the consecutive sub-elements in that throat need to be merged so that the Pe number in each new element is just below unity. However, this coarsening cannot be done freely since by merging two or more elements it is assumed that ions may diffuse freely between them. This may be problematic in the presence of high concentration gradient where a significant numerical diffusion is introduced. Therefore, along with local Pe, the concentration difference between consecutive sub-elements acts as a secondary criterion ($\Delta C < 0.01 C_{sat}$) which may limit the coarsening of the numerical grid. In order to help better understand this section, a flowchart is presented in Figure 2.13.

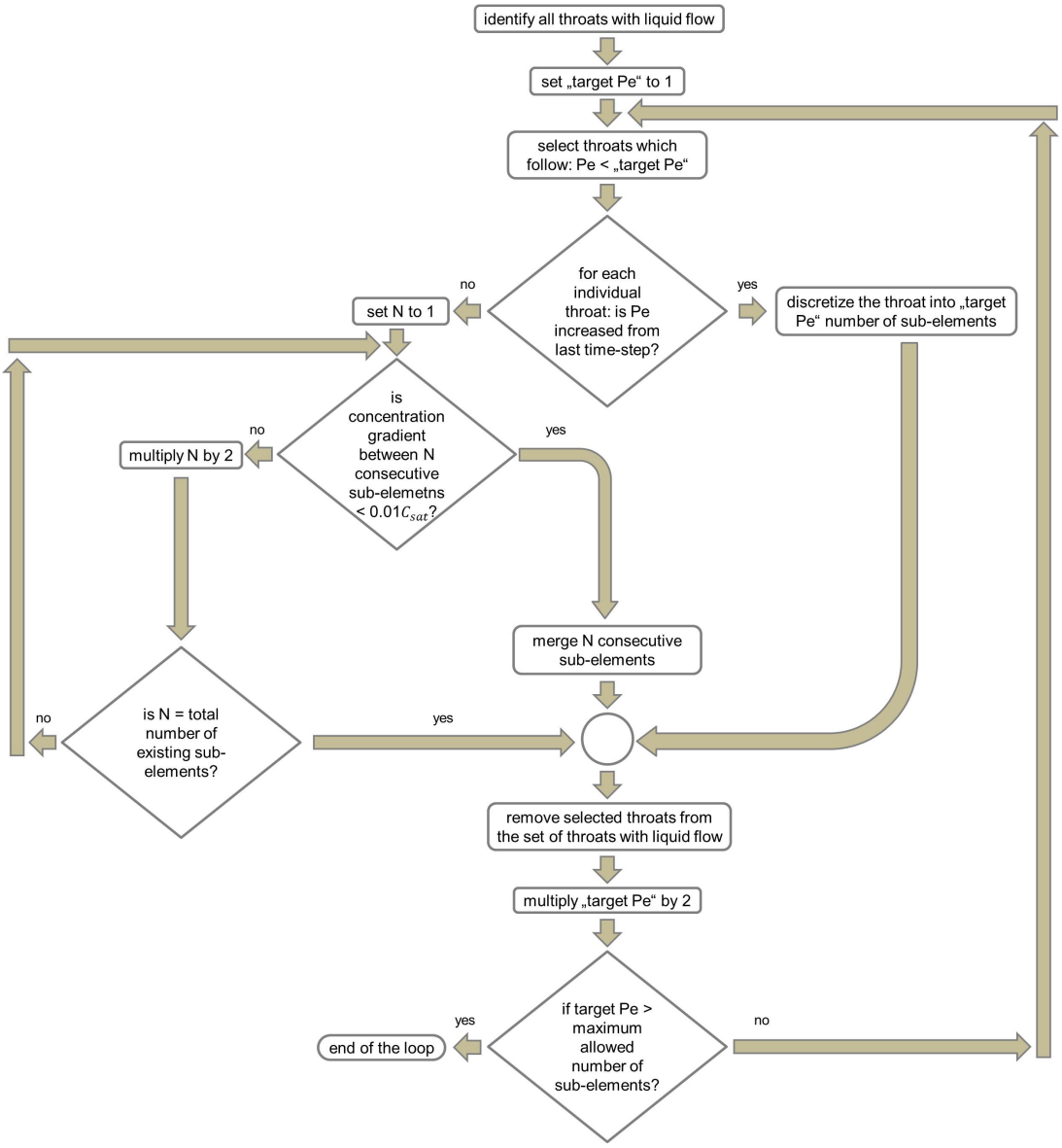

Figure 2.13: Flowchart of adaptive discretization of throats for ion transport calculations.

2.3 Simulation results

2.3.1 Introduction

In this section, the network simulations for the 2D square network with mono-modal pore size distribution will be presented. The simulations are carried out for various drying conditions and different initial concentration of salt. Note that the results of 2D pore network simulations are mainly for the purpose of understanding as they allow better visualization of phase distributions. Certain effects require careful analysis of micro-scale mechanisms (individual throats) which can be studied with more ease in 2D configuration. To keep the results consistent and for the sake of comparison, the same network is used for all simulations.

A 10 by 10 network with mono-modal radius distribution of the throats is considered for these simulations. Said throat radii are generated by a normal distribution function ("normrnd") in "Matlab 2013 software" with a mean value of 100 nm and a standard deviation of 10 nm. Throats have uniform length of 1 μm. Physical properties of the liquid are considered as pure water and physical properties of the salt are considered as NaCl at 25 $^{\circ}C$. All the parameters for the simulations can be found in Table A.1 of the appendix.

Two different drying conditions are considered. Slow drying is obtained by setting the total boundary layer thickness to 100 μm (comprised of 10 layers of boundary layer throats) and the drying air temperature at 25 $^{\circ}C$. Fast drying conditions are simulated by decreasing the boundary layer thickness to 1 μm (same number of boundary layer throats with one hundredth the length for the vertical ones compared to slow drying case) and increasing the drying air temperature to 80 $^{\circ}C$.

Two different levels of initial salt concentration are investigated here. In the first set of simulations salt concentration is set to 90 % of saturation concentration (323 $kg.m^{-3}$) whereas in the second set the initial concentration is set to 20 % of saturated solution (71.8 $kg.m^{-3}$).

Note that these values are in this entire section referred to as fast/slow drying and high/low initial concentration. The results of respective combinations will be discussed in the following subsections.

2.3.2 *Slow drying and high initial concentration*

In this scenario, the capillary fingering regime is maintained for the majority of the simulation. This means that only a handful of throats at the network surface are dried at the beginning of the drying and the liquid-gas interface invades the network as the main liquid cluster stays connected to the network surface. The role of liquid viscosity is rather limited in this case and the liquid is supplied to the network surface until the network saturation drops below 70 % at which point the surface finally dries out (Figure 2.14). This causes the drying rate to fall and the evaporation front starts to recede into the network (Figure 2.15 and Figure 2.16(b)).

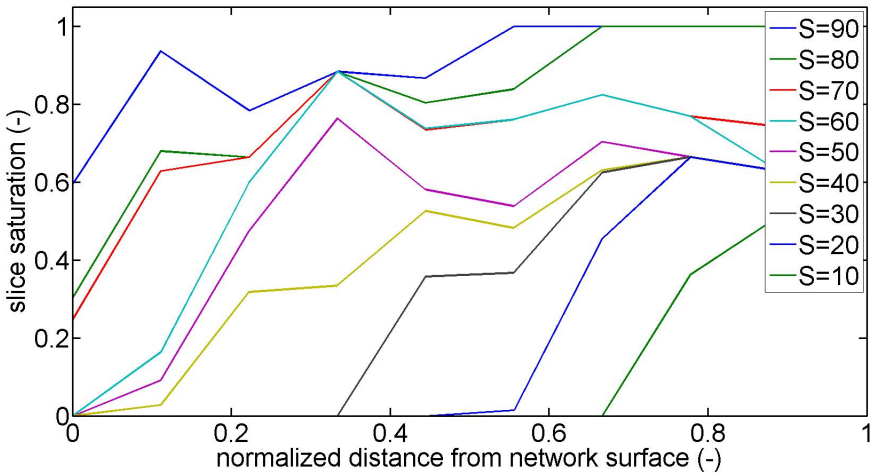

Figure 2.14: Saturation profiles in the course of slow drying of 10 by 10 network.

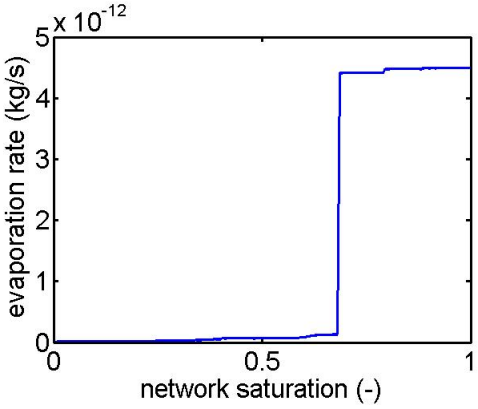

Figure 2.15: Drying curve vs. network saturation for slow drying of 10 by 10 network.

The pattern with which salt crystals are formed can be explained by following the liquid flow quite accurately. This is not always the case especially if diffusion is

dominant, which does not occur in this scenario due to high initial concentration (inhibiting high concentration gradient to be established). Therefore, as the liquid flows by capillary pumping to the surface (during the first drying period), the concentration of salt rises at the surface liquid throats and the first crystals appear at the larger throats due to higher evaporation rate (Figure 2.16(a)). However, since the smaller throats maintain the liquid connection for a longer period (due to higher capillary pressure), the throats with the maximum mass of crystals are the smaller ones at the surface (Figure 2.16(b)). As drying proceeds and the connection of liquid to the network surface is lost, crystallization will take place in the interior of the network. Note that there are some isolated liquid throats or clusters in the interior of the network in which liquid flow is halted as long as the drying front is located relatively close to the surface. Crystallization in these regions does not start until the liquid clusters above them have evaporated (Figure 2.16(c)).

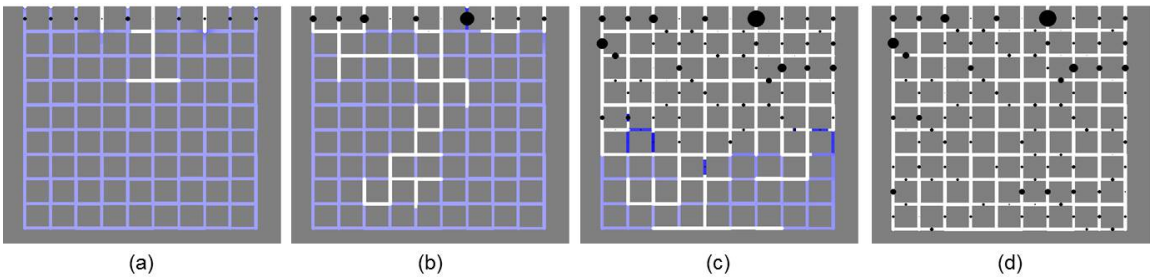

Figure 2.16: Phase distribution plots for salt solution (shades of blue) and crystals for slow drying of a 10 by 10 network with high initial salt concentration: (a) 95.5 %, (b) 75.1 %, (c) 25.2 % and (d) 0 % saturation. Darker blue colors represent higher concentration. The radius of the disks corresponds to the mass of crystals per throat by the whole salt mass.

At the end of drying, as shown in Figures 2.16(d) and 2.17, the majority of the crystals is located at the network surface. To summarize, this is mainly due to the capillary fingering regime which is responsible for transporting a significant amount of liquid and thus dissolved salt to the network surface.

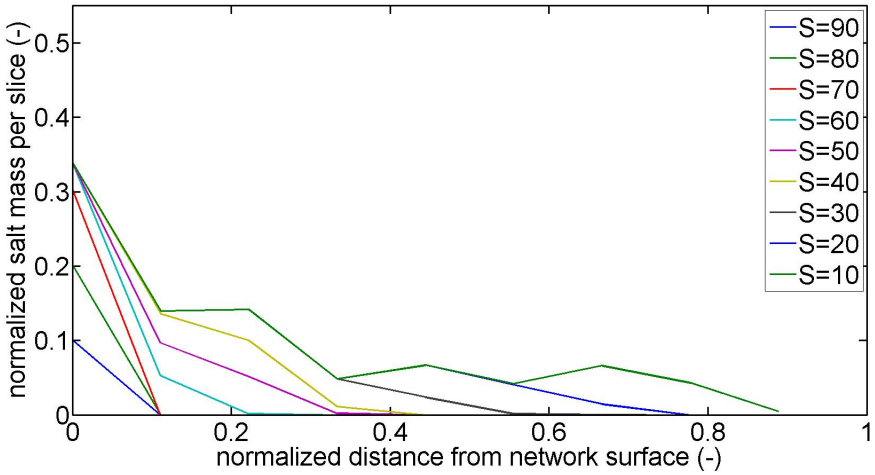

Figure 2.17: Crystal mass vs. network height for slow drying of 10 by 10 network filled with highly saturated solution.

2.3.3 *Fast drying and high initial concentration*

As mentioned before, fast drying is obtained by decreasing the boundary layer thickness and simultaneously elevating the drying temperature. A viscous stabilization regime is observed at the beginning of the simulation in this case, as the drying front recedes into the network (Figure 2.20(a)). This stage takes place rapidly; the liquid connection to the network surface gets lost and the drying rate falls significantly early in the process (Figures 2.18 and 2.19). As a result, the liquid flow pattern in the network is altered and the capillary force starts to be dominant. Therefore, the evaporation front stagnates beneath the network surface and liquid is transported to that region for evaporation. This leads to a similar liquid flow pattern as in the slow drying case from middle stages of the drying towards its end (Figures 2.20(b) to (d)).

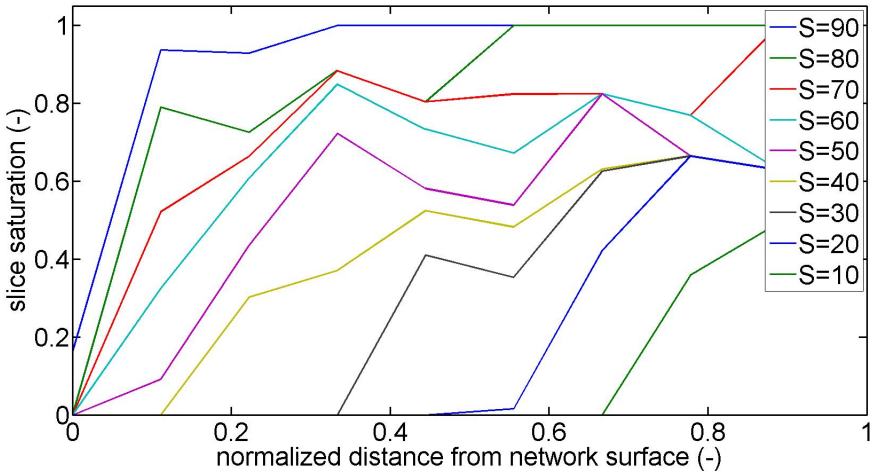

Figure 2.18: Saturation profiles in the course of fast drying of 10 by 10 network.

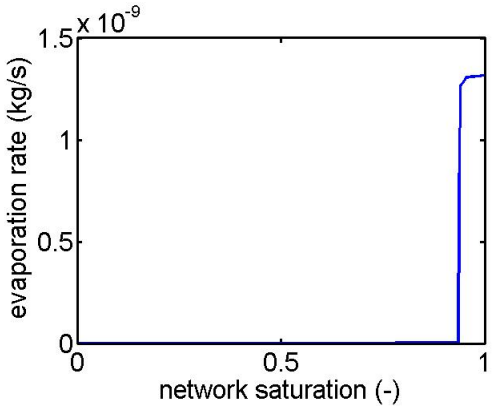

Figure 2.19: Drying curve vs. network saturation for fast drying of 10 by 10 network.

As initial salt concentration is, similarly to the previous case, at a high level, ion transport is dominated by advection and can be described following the liquid flow pattern. In the first stage of the simulation, liquid evaporates locally indicating that the transport of ions is basically nonexistent in this period. Hence, crystals are formed locally in each corresponding throat (Figure 2.20(a)). Later on, stagnation of the drying front beneath the network surface and establishment of capillary fingering regime leads to ion transport and crystallization to the region beneath the network (Figure 2.20(b)). Continuation of drying yields a similar flow pattern to the case of slow drying, leading to similar crystallization pattern in the interior of the network (Figure 2.20(c)).

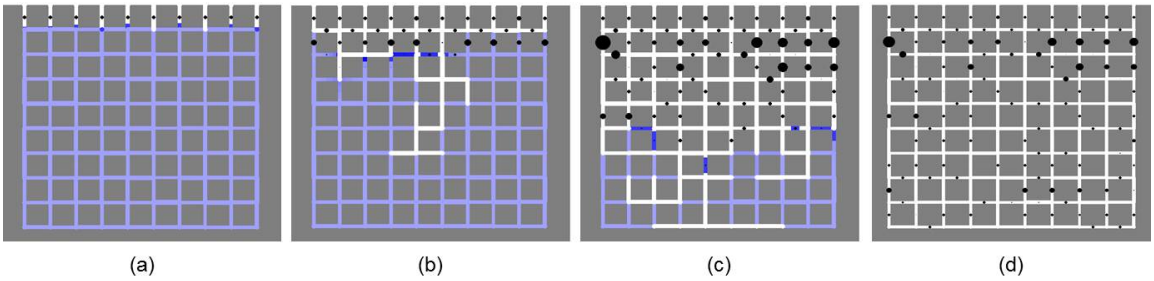

Figure 2.20: Phase distribution plots for salt solution (shades of blue) and crystals for fast drying of a 10 by 10 network with high initial salt concentration: (a) 95 %, (b) 75 %, (c) 25 % and (d) 0 % saturation. Darker blue color represents higher concentration. The radius of the disks corresponds to the mass of crystals per throat by the whole salt mass.

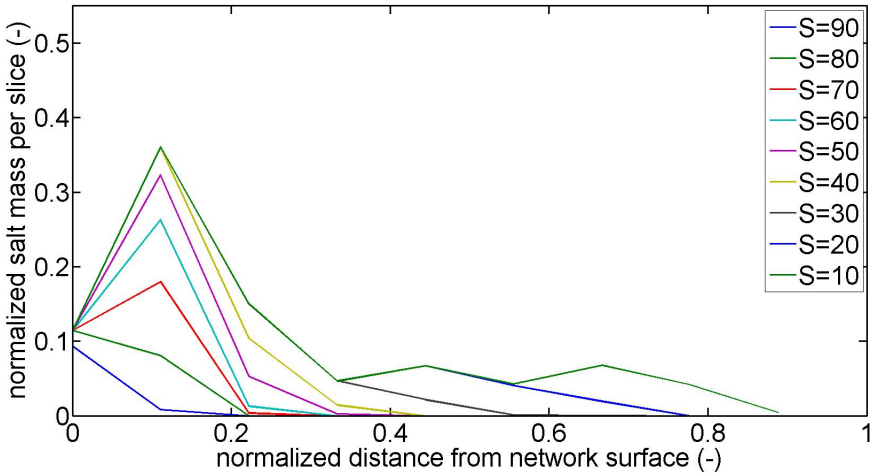

Figure 2.21: Crystal mass vs. network height for fast drying of 10 by 10 network filled with high saturated solution.

Looking at the final crystal distribution in the network, it can be deduced that the major crystallization zone is located beneath the network surface or at the position of the second slice (Figure 2.21). The crystals formed at the network surface are of uniform size, as a result of rapid crystallization (Figure 2.20(d)).

2.3.4 *Slow drying and low initial concentration*

In this section, in order to avoid repetition, only the final crystal distribution at low initial concentration is shown side by side to that of the high initial concentration to compare the effect of ion diffusion on final crystal distribution in the network in case of slow drying. For slow drying, the effect of ion diffusion is expected to be more

pronounced. Note that the size of black disks in the figures represents the relative mass of crystals (mass of crystals per throat divided by total salt mass), which makes the side by side comparison relevant.

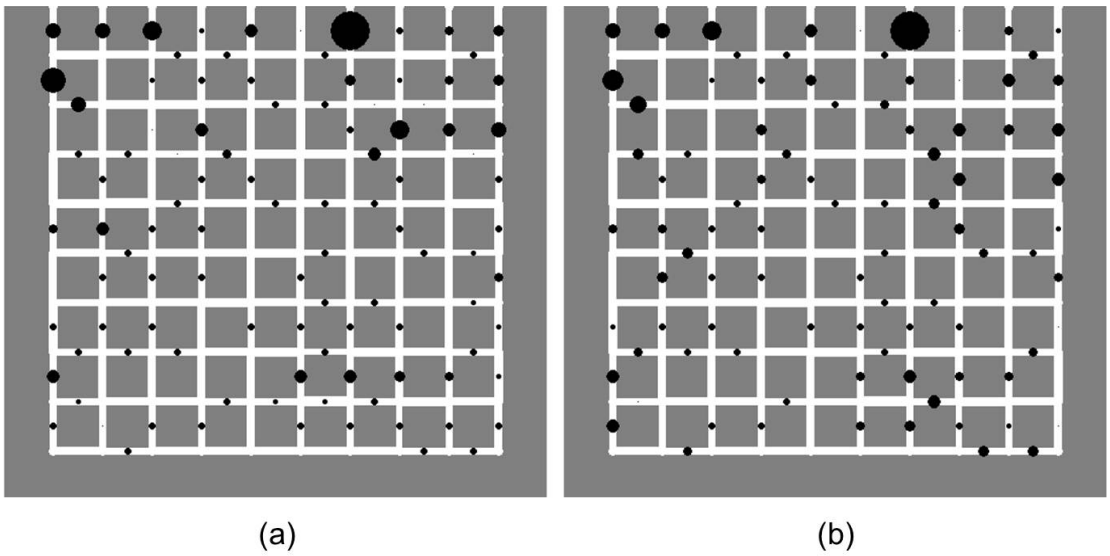

Figure 2.22: Final crystal distribution in the network after slow drying for: (a) high initial concentration and (b) low initial concentration.

There are several points which can be mentioned regarding the similarity and the slight differences between the two figures. Firstly, due to lower initial concentration more liquid needs to be evaporated before the onset of crystallization. Moreover, despite low drying rate, diffusion is still slow especially in the first drying period which means the concentration difference is not leveled out. This allows a high concentration gradient to build up, because of the low initial concentration, which elevates the diffusion rate significantly. However, as liquid is evaporated the average salt concentration increases thus decreasing the potential for diffusion. This in combination with the fact that higher concentration is closer to the saturation level means that it is unlikely for crystallization to take place at the beginning of the drying. This explains the lack of crystals in several throats which generally dry out at the beginning of cluster evaporation. Furthermore, the crystals are more homogeneously distributed within the throats with more salt in this case. This is due to retardation of the onset of crystallization due to strong diffusion as opposed to early crystallization before diffusion can redistribute the ions.

2.3.5 *Fast drying and low initial concentration*

Fast drying of low concentrated solution results in opposing effects. On one hand by decreasing the initial concentration the room for diffusion grows, on the other hand, fast drying limits the time available for diffusion to take place. It can be observed in Figure 2.23 that the lower initial concentration has not been effective in changing the crystallization pattern at the beginning of drying. Later on, due to the reduction of evaporation rate caused by recession of the drying front, similar effects as in the previous comparison (Figure 2.22) can be observed.

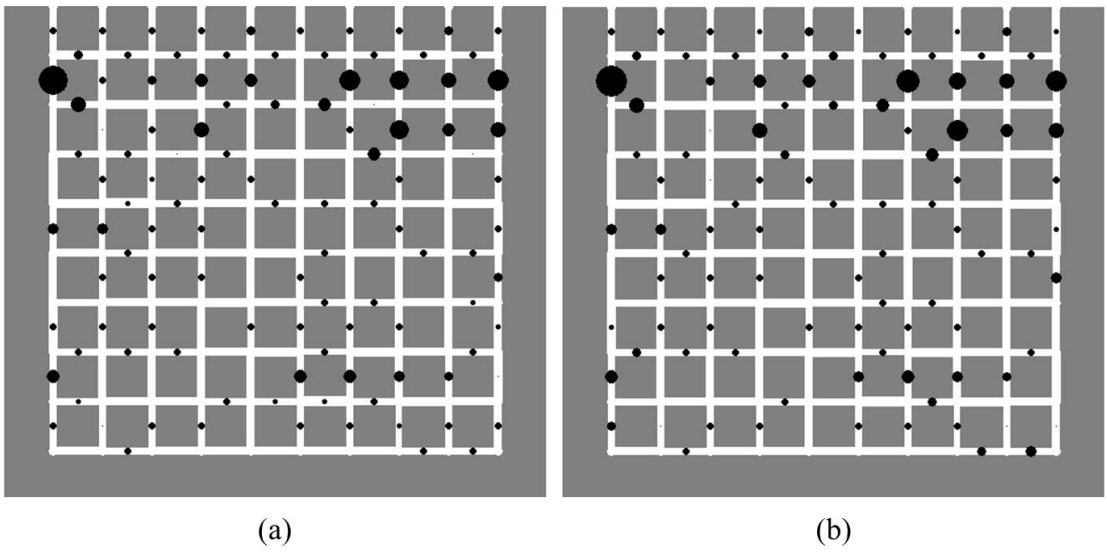

Figure 2.23: Final crystal distribution in the network after fast drying for: (a) high initial concentration and (b) low initial concentration.

There are two points to be noted in regard to this comparison. At the beginning of drying (first 5-10 % of network saturation loss) the significance of the increase in drying rate is much larger compared to the effect of larger concentration gradient. This also implies that at initial drying rate, the diffusion can only be increased if the binary diffusion coefficient is elevated since it is the only other parameter influencing the diffusion rate in the model. For the rest of the drying, due to the significant drop in the evaporation rate diffusion becomes more important. The diffusion effect is certainly less pronounced compared to the previous case of slow drying; nonetheless, there is noticeable influence of diffusion due to low initial concentration when compared side by side to the case of high initial concentration.

2.3.6 General remarks

Before wrapping up this chapter one important finding needs to be mentioned. As shown in Figures 2.15 and 2.19 the drying rate has a very sharp drop in the transition period between the first and second drying period. This does not agree with the general understanding of drying process. Through further investigation, we realized that the porosity of the simulated networks is too low to be indicative of a real porous media. This can be resolved by lowering throat length which requires increasing the number of throats to replicate the same overall size. This is not the optimal solution as it hugely impacts the computational time that grows exponentially with increasing number of throats. In Chapter 4 a solution is proposed aimed at tackling this issue which involves utilizing information regarding network porosity.

The 2D pore network simulations have proved helpful in providing insight and understanding of the crystallization process in porous media during drying. However, the 2D pore network model falls short in several aspects, which further motivates the transition to 3D configuration. The 3D variant of the model will include some modifications, the most important of which is directed at improving the drying curve caused by low network porosity.

2.4 Conclusion

In this chapter, a pore network model has been presented which can simulate the drying of porous media saturated with salt solutions. Vapor transfer in the system has been modeled by diffusion in the gas-filled part of the network and the diffusive boundary layer, whereas liquid transfer in the network has been modeled by viscous-capillary flow. Quasi-stationary conditions have been assumed during global time-steps.

Ion transfer in the liquid phase has been modeled by a 1D advection-diffusion equation. This equation has been solved by an explicit solution scheme in the given network geometry. The discretized equation has been validated by a test problem in the form of a capillary connected to a reservoir and exposed to evaporation from the other side. Furthermore, the accuracy of the model has been assessed by comparing the results of pore network simulations to the analytical solution of the problem of mass dispersion in a tube. This comparison reveals that in order to achieve good numerical accuracy, the local Pe number in each computational element should be preferably less than 1. Therefore, the numerical grid for ion transfer calculation has been refined by dividing throats into several sub-elements depending on the local Pe

number.

2D simulation results have been presented for various conditions which help understanding the mechanisms involved. In these simulations, the same network has been used for all different cases which makes identification of the effects and comparison easier. It has been observed that slow drying leads to crystallization at the surface (efflorescence) as the strong capillary flow provides the means to transfer ions to the network surface. On the other hand, fast drying leads to rapid evaporation of the liquid at the network surface with moderate local crystallization in the surface throats. As the drying front recedes into the network drying rate slows down dramatically, which results in a capillary fingering regime being established leading to a major crystallization zone beneath the network surface. In the depth of the network very similar crystallization pattern is observed for the fast and the slow drying cases, which is due to the drastic drop in the evaporation and capillary flow being dominant no matter how high the evaporation rate is. In order to study the effect of ion diffusion, initial salt concentration has been reduced which allows the build-up of higher concentration gradients in the network. However, apart from a few minor variations, we were not able to capture significant disparity for this case in which diffusion should be more pronounced. This effect will be further studied in Chapter 4 with 3D simulations, as it is expected that increasing liquid connectivity might enhance some effects.

The shortcomings of the 2D model can be summarized in a few points as follows:

1. The porosity of the network is very low (the network used in the above simulations has a porosity of 16 %). In order to increase the porosity, the length of the throats has to be reduced, which means more throats are required to produce the same size of porous material.

2. Drying rate drops significantly at the very beginning of the second drying period. This limits the establishment of viscous stabilization regime, which is otherwise expected in the case of fast drying. As a result of this limitation liquid flow patterns, in the region of medium and low global saturation, for both slow and fast drying are very similar to one another. This leads to similar crystallization patterns in the interior of the networks. It is believed that adjusting porosity to more realistic values should lift said limitations and tackle the rapid drop in drying rate.

3. The connectivity of liquid is rather limited in a 2D network. This effect leads to early isolation of clusters of liquid from the main cluster which provides access for liquid capillary flow to the drying front. Therefore, the capillary fingering regime is not as pronounced as it is expected.

We are convinced that these shortcomings can be tackled by a model extension to 3D configuration which will be presented in Chapter 4.

Chapter 3

Combined wetting, drying and crystallization in a pore network model

Impregnation of porous media comprises of two stages: the wetting stage and the drying stage. In Chapter 2, the drying-crystallization pore network model assumes the porous material is filled with a uniformly saturated salt solution. This assumption is only plausible if the material is prepared by sinking it in a bath of salt solution for enough time. Although such a preparation procedure is certainly included in some processes, there are also other methods of infiltration of liquid. Sometimes, the wetting stage is not isolated from drying, such as in spray agglomeration processes or in ink-jet printing. Other examples, in nature, may include the contamination of building materials with groundwater. Therefore, it is essential to develop a model that can simulate the entire process starting with an unsaturated material.

In this chapter, we aim to utilize the algorithm of Rahimi et al. [87] and incorporate salt in the reservoir to model infiltration of a salt solution droplet and drying. This model revealed several shortcomings during previous parametric studies which were then resolved pragmatically. Here the opportunity is used to address such issues by modifying the pore geometry. In this endeavor throat intersections which were modeled by nodes with no volume are replaced by spherical pores. This modification brings about great benefits both in algorithm improvement and simulation efficiency. A detailed discussion will be presented in Section 3.2.3.

In the model for combined wetting and drying, the reservoir contains the entire mass of salt which is transported to the network by capillarity. The ion transport and crystallization algorithm presented in the previous chapter are adopted here.

However, since the pore network models of the previous and current chapters are intrinsically different from each other, some aspects need to be revisited. Moreover, the new pore elements, namely the spherical pores, require specific treatment as their function is fundamentally distinct from the throats.

Prior to exploring the model's algorithm and presenting the results, it is important to briefly mention some of the previous work regarding the modeling of imbibition (infiltration) of porous media. Similarly to drying, various continuous and discrete models are available, each with distinct benefits and disadvantages. Next section summarizes the findings of these studies.

3.1 Literature study

As mentioned in the previous chapters, approximating the void space of porous media by capillaries has been used traditionally in modeling the liquid flow in such materials. In respective models, the flow is driven by capillarity which builds up the necessary pressure gradient. In the 19th and 20th centuries many attempts have been made resulting in empirical models, the most well-known of which is Darcy's law (Equation 1.6). Darcy's law and similar equations require the representation of pore level physics by effective parameters, such as liquid conductivity, effective diffusivity, etc. The volume averaging method is generally used to obtain these effective parameters. In general, Darcy's law, as well as Lucas-Washburn equation (Equation 1.7), have been used to describe wetting physics in porous media.

The source from which liquid is provided to the porous material is very important in model development. In this work, we consider a droplet at the surface of the medium as the reservoir which supplies liquid to a number of surface pores. Thus, in the following, some of the literature on the infiltration of droplets into porous media is discussed. Generally, the fate of the droplet is determined by a variety of mechanisms such as phase change, physical bonding, chemical reaction, etc. [72]. In the presence of non-reactive and low-volatile liquid, the infiltration process is narrowed down to a momentum transport problem [61]. Many factors may contribute to this problem such as influence of terminal (deposition) velocity [44], spreading speed of the liquid on the surface [98], and capillary force within the material [34].

After droplet relaxation on the porous medium, the flow can be broken down into a lateral component (along the surface or spreading) and a normal component (vertically downward or infiltration). On that note, two different regimes have been proposed for the time evolution of the droplet shape, namely constant drawing area

or receding drawing area as denoted by [19]. Constant drawing area refers to the case that the droplet maintains the size of its footprint and the contact angle at the droplet boundary decreases as liquid is imbibed. This stage generally takes place at the beginning of infiltration. The second stage is defined as the period in which the droplet shrinks in size (area) while a constant contact angle is maintained. This period usually describes the final stages of the droplet's life. Sometimes these conditions are fixed (outer problem) which enables the solution to focus on the transport phenomena within the porous medium (inner problem) [60]. The effect of the interaction of capillary and drag forces on droplet drawing area is shown in a detailed study by Starov et al. [97] [98].

A 2D model of viscous spreading and imbibition of a droplet placed on the surface of a porous substrate has been developed by Davis and Hocking [16] [17]. Initially, the droplet is located on a partially saturated substrate. The properties of the liquid droplet may be different from those of the residue in the porous medium [16]. The main purpose of this study was to determine the lifetime of the droplet and the evolution of contact lines. For this reason, the model only captures the macro-scale mechanisms namely imbibition and spreading, neglecting physical parameters such as wettability and wetting contact angle in capillaries. However, on continuation of that work a second model was proposed where the porous material can be initially dry [17]. This model was aimed at infiltration of the droplet into the voids of the material which are described as vertical capillaries. The cross-sectional area of these pores is constant along the axial direction and no horizontal connection is present in the substrate. Thus, no lateral flow of liquid in the porous medium is to be considered. As decreasing drawing area regime has been assumed for the droplet, the liquid slip velocity is defined. The shape of the sessile droplet and the imprint in the porous material are determined over time from this variable.

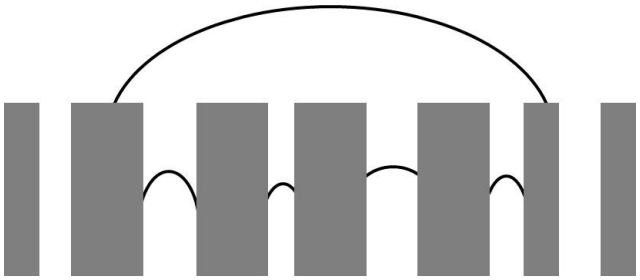

Figure 3.1: Schematic view of a liquid droplet and vertical capillaries representing the void space of porous substrate [17].

Darcy's law has been used to describe liquid flow in the framework of lubrication

theory for droplet infiltration [1]. The porous material comprises of two regions (saturated and unsaturated) which are separated by a discontinuous front. In this theory, the volume of the droplet is chosen such that it can be described by a thin film at the surface. The problem has been solved numerically by the finite element approach. Unlike most models, in this case, the droplet does not strictly follow only one of the aforementioned regimes (constant or receding drawing area). At the start of the simulation, the droplet exhibits a constant drawing area which is followed by a mixed regime where both contact angle and drawing area recede simultaneously.

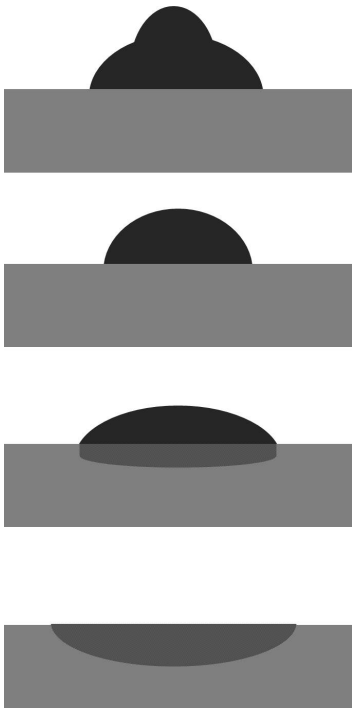

Figure 3.2: Evolution of a sessile droplet as it arrives at the substrate surface until full imbibition, as proposed by Clarke et al. [13].

The process of ink-jet printing has been modeled by Clarke et al. [13], including validation by experiments. Their model suggests that the droplet behavior (whether it will splash or not) as it comes in contact with the surface can be predicted by the value of Weber number (the ratio of inertia to capillary force),

$$We = \frac{\rho r u^2}{\sigma}, \tag{3.1}$$

where r refers to droplet radius. The common values of We in this application revolve around unity (it is alleged that values of around 50 are required for splashing). It is argued that as the droplet comes in contact with the surface of the substrate,

the contact angle reaches a static value followed by expansion of drawing area. As the process continues, the droplet infiltrates into the paper, initially with a constant drawing area, then with a constant (minimum) contact angle. The section regarding relaxation of the droplet has been adopted from a model for non-permeable solid material which was validated by experiment [8].

The aforementioned studies handle the imbibition as single-phase flow, assuming the porous material as a rigid body unaffected by the liquid. Nonetheless, sometimes due to the flow of liquid within the micro-structure the medium is altered to various extents. For example, experiments with various fluids reveal how wetting properties deviate from that predicted by the Lucas-Washburn equation [80]. The porous media in this case were constructed as compacts of carbon black or silica powders. This topic has also been studied numerically by a continuum approach to the porous medium [62]. MRI experiments conducted by Mantle et al. [59] suggest that liquid infiltration should be considered as multiphase flow. These experiments demonstrate that according to wetting properties of the liquid, various partially saturated zones might be formed. Single- and multiphase flow have been studied both experimentally and numerically by sessile droplet spread and sorption in medium grain-size sand [20]. Experiments reveal that multiphase flow dominates as the free liquid on the surface depletes.

The discrete modeling approach has also been applied to the wetting problem. In the absence of evaporation, liquid infiltration may be divided into two distinct stages: primary and secondary infiltration [63]. These two steps are differentiated by whether a free sessile droplet can be found on the surface, or not. The process has been modeled by a capillary network model where heterogeneity of pores determines liquid capillary flow in the network. During primary infiltration a sharp propagating front of the wetting phase is maintained, representing single-phase flow. The shape of the front becomes ramified in the secondary infiltration step, establishing multi-phase flow. The fate of the liquid cluster in the second step is to split up into ganglia until the entire body of liquid has been distributed in the network, at which point secondary infiltration terminates. Primary and secondary infiltration are illustrated schematically in Figure 3.3.

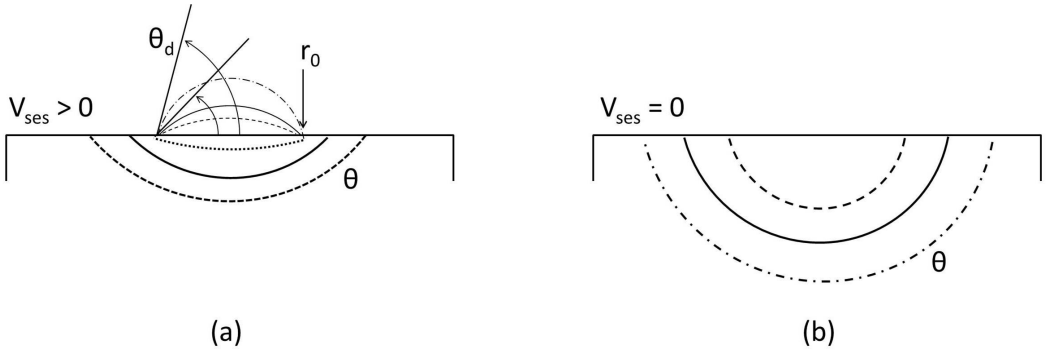

Figure 3.3: Droplet penetration into porous materials during: (a) primary infiltration and (b) secondary infiltration (adopted from D'Onofrio et al. [20]). V_{ses} is current liquid volume in the droplet, θ_d and θ, dynamic and liquid-solid contact angles respectively, and r_0 the base radius of the sessile droplet.

Secondary infiltration in wet wipes has been modeled by liquid migration algorithm in a pore network model [101]. The multi-layer fibrous materials have been mapped to pore network models based on X-ray microtomography scans of wet and dry wipes. A layered pore network represented the void space of the substrate, with each layer having distinct properties. Simulations were carried out until liquid distribution in the network had reached equilibrium. The effect of contact angle and liquid viscosity has been analyzed in a parametric study. Qualitative agreement between experiments and simulation results has been achieved. Similar pore-level liquid transport rules have been later adopted to develop a pore network model which also captures the primary infiltration step [102]. This new pore network model has been validated by spontaneous imbibition of liquid into a micro-model made of etched silicon-glass. During the course of experiments, binarized images were captured which approved the results of pore network simulations. Furthermore, bimodal pore size distributions have been implemented in the network with three different spatially correlated patterns. These simulation results demonstrated how capillary flow in the network is influenced by the macro-throats. Such results cannot be predicted by the classic approach of Lucas-Washburn equation.

The aforementioned imbibition algorithm of Sun et al. [102] [101] has been coupled with the drying algorithm of Metzger et al. [66] to develop a combined wetting-drying pore network model in [87]. In that model, the liquid was supplied to the network by a droplet (modeled as a reservoir) with the aim of simulating spray agglomeration process (as shown in Figure 3.4). The effect of various factors such as drying rate, pore size distribution and multiple droplet deposition has been studied using this pore network model. During multiple depositions of droplets, according to the time interval between consecutive depositions, several liquid clusters may form which can

merge or split depending on various conditions. Parameters such as droplet lifetime, liquid penetration depth, and maximally wetted area are of importance in these simulations.

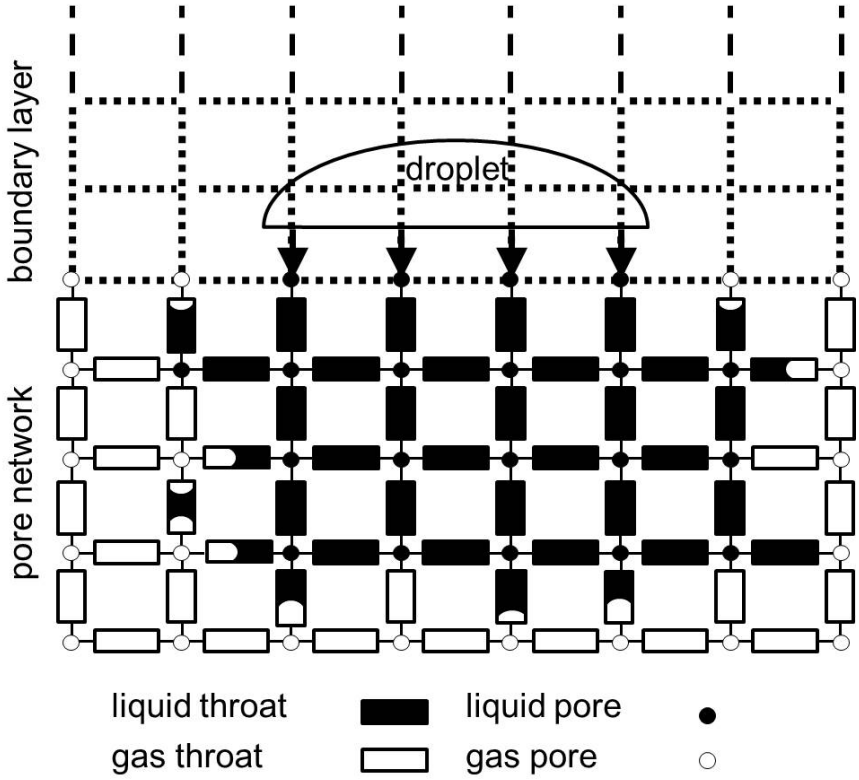

Figure 3.4: Schematic of a partially saturated network with a reservoir supplying liquid to the surface pores as used in Rahimi et al. [87].

3.2 Model description

So far in this thesis, we focused on drying of porous media already saturated with salt solution. The entire procedure leading up to this point has been neglected and at the start of the simulations uniform salt concentration throughout the network has been assumed. This is plausible in some industrial applications where porous media are filled by submerging them into a liquid basin. Nonetheless in many applications, such as spray agglomeration process, particles that are being sprayed by a solution are simultaneously exposed to evaporation. Therefore the second part of the process (i.e. the drying stage) may differ significantly compared to the previous chapter. The main points of difference concern initial network saturation and initial salt concentration.

The goal in this section is to include the said missing effects by modeling simultaneous wetting and drying starting with a dry network. Similar to the previous Chapter 2, the liquid and vapor transport algorithm is discussed initially. Later on, ion transport and crystallization algorithm is implemented. Treatment of new elements (spherical pores) requires several modifications which should be explained. At the end of this section, several aspects of the developed model are compared with other pore network models. Firstly, the improved wetting-drying model (without dissolved salt) is compared to the model of Rahimi et al. [87]. The goal here is to characterize the effect of pressure barrier generated by spherical pores versus the volumeless nodes. Furthermore, the crystallization pattern predicted by the current model, which accounts for liquid migration, is compared to that of the drying-crystallization model of Chapter 2. It is expected that, since in the current model dried regions may be subject to rewetting, the final crystallization pattern can differ for the two models. Simulations carried out for various cases by this model will be presented in Section 3.3.

3.2.1 Combined wetting-drying model

The pore network geometry used for this model has been slightly modified compared to that of Chapter 2. The main modification concerns the junctions of the throats which in this case are represented by spherical pores (as opposed to volume-less nodes). Therefore the void space consists of a network of horizontal and vertical cylindrical throats (similar to the network of Chapter 2) and spherical pores in between. In this square network, the distance between the centers of two consecutive pores is predefined and uniform. Throat radii vary across the network and are generally randomly distributed. The radius of the pores is defined according to the radius of the largest neighboring throat multiplied by a constant factor denoted as "radius multiplier" ("1.1" throughout this thesis unless it is deliberately varied for the sake of comparison as in Section 3.2.3). Therefore, a random distribution of pore radii in the network is obtained. Note that due to this distribution throat lengths are to be adjusted to avoid the spatial overlap of the throats and pores, leading to nonuniform throat length throughout the network.

The equations which govern transport phenomena used in this model are identical to those of Chapter 2. However, the rules and assumptions are slightly altered and new possibilities are accounted for. The addition of a new pore geometry enables improvement of the model in some areas which will be discussed below. Due to the obvious similarities of the two models, the general concepts of the new model are only briefly mentioned to leave more room for the intricate parts of the algorithm.

Evaporation is only from the top leading to the establishment of a diffusive boundary layer at the surface. Vapor diffusion in the network and the boundary layer is modeled by Stefan's law (Equation 2.1) following a quasi-steady approach. On that note, the vapor pressure field is calculated by solving a system of algebraic equations obtained from mass conservation at the relevant pores. Contrary to the previous chapter, vapor pressure at the pores is not automatically equated to the saturation vapor pressure when there is liquid in the neighborhood. Instead, the vapor transfer resistance in partially filled throats has been accounted for, which results in two types of boundary conditions as follows:

1. Gas pore next to stationary menisci: If a throat is fully saturated with liquid but has a meniscus at one end the corresponding pore is assumed to maintain saturation vapor pressure. The resulting boundary condition is similar to the typical boundary conditions of Chapter 2.

2. Gas pores with no adjacent stationary menisci: Presence of liquid causes gas at the immediate interface to be saturated with vapor. This idea is implemented for partially filled throats (containing moving or isolated menisci) to impose a boundary condition over their neighboring gas pore. In this case, the empty length of the throat defines the gas conductance for vapor transfer.

Following the aforementioned steps, a matrix formulation of the system of algebraic equations is adopted. Using a matrix inversion technique this system of equations is solved providing the vapor pressure field in the system.

Liquid viscous-capillary flow in the network is modeled by Poiseuille's law. At the beginning of the simulation, liquid is supplied to the network by a reservoir connected to a number of surface pores. These pores remain wet as long as the reservoir contains liquid and contribute to the evaporation in the boundary layer. This evaporation is then attributed to the reservoir instead of direct evaporation from a droplet cap (an abstract representation of a sessile droplet). The reservoir width, by which these surface pores are determined, is assumed to remain constant throughout the process ($W_d = W_{d,0}$), whereas droplet height and contact angle decrease (constant drawing area assumption). These values are calculated according to the initial liquid volume ($V_{d,0}$) and contact angle ($\theta_{d,0}$ chosen as 30 ° for the simulations of this chapter):

$$H_{d,0} = \Big(\frac{3V_{d,0}(1-\cos(\theta_{d,0}))}{\pi(2+\cos(\theta_{d,0}))}\Big)^{0.33}, \tag{3.2}$$

$$W_{d,0} = 2H_{d,0}\Big(\frac{\sin(\theta_{d,0})}{1-\cos(\theta_{d,0})}\Big). \tag{3.3}$$

The liquid pressure in the surface pores contacting the reservoir is considered to be equal to atmospheric pressure as the curvature of the droplet is assumed to be sufficiently large. Liquid flows, by capillarity, into the network as menisci are formed in the adjacent throats to the wet surface pores. As the liquid cluster grows the pressure is calculated by holding mass conservation at every fully saturated pore. Coupling said equations for every full pore in a cluster leads to a system of algebraic equations for the liquid pressure field. Before introducing two discrete events that determine the liquid flow path in the network the boundary conditions for the aforementioned system of equations are presented:

1. Pores connected to the reservoir: As stated before, the pressure at these pores is directly set to atmospheric pressure (reservoir pressure). Thus, these pores always provide boundary conditions for the main liquid cluster. This type of boundary condition is set as the product of liquid conductance of the adjacent throats and the pressure at the respective pores.

2. Stationary menisci: Liquid pressure at stationary menisci cannot be directly determined (in-depth discussion in Section 2.2.1) whereas the evaporation rate is. In this model stationary menisci may be located in either throats or pores which are fully saturated with liquid. Therefore, the liquid flow rate, identical to the evaporation rate, is defined as the boundary condition.

3. Moving menisci: It is assumed that the curvature at moving menisci is maintained at the minimum possible, irrespectively whether the meniscus is receding or advancing. This assumption enables computation of liquid pressure at the menisci as a function of radius. Similar to the stationary case, moving menisci can be located in either throats or pores. Nevertheless, it is essential that these bodies are not fully saturated, else the meniscus becomes stationary.

Note: Stationary menisci need to be identified sequentially as explained in Section 2.2.1. However, this liquid retraction loop works in tandem with "liquid invasion" events. This sequence will be explained with a flowchart later on.

Note: In order to comprehend the implementation of boundary conditions regarding pores several remarks need to be pointed out:

Pressure at pores: Perfect mixing assumption has been adopted for the pores. This means that each variable (vapor or liquid pressure and salt concentration) attributed to pores is spatially constant in a given time-step. A direct consequence of

this assumption is that in parameters such as liquid conductance the length of liquid within the pores is neglected.

Constant meniscus pressure: The liquid pressure caused by curvature at menisci is considered to be constant with pore saturation. Consequently, the pressure assigned to moving menisci in the pores can be represented according to sphere radii using Equation 2.6.

Liquid retraction-liquid invasion loop

Calculation of vapor pressure field and, consequently, evaporation at menisci is carried out as the preliminary part of this loop. Afterward, fully saturated throats and pores with menisci are identified as stationary. Using the proper boundary conditions, the liquid pressure field is calculated. The initial assumptions are validated by calculating whether enough liquid is being supplied to all stationary menisci to compensate for evaporation. Upon discovering evaporating menisci to which sufficient liquid is not provided, the one with the highest flow deficit changes its status to receding (moving). Each cluster needs to be treated separately. Liquid pressure computation is repeated assigning the correct boundary conditions as long as no liquid retraction is necessary.

Liquid invasion refers to the sudden advancement of stationary menisci into a neighboring pore or throat. The liquid flow path in the network is defined by liquid invasion during wetting. According to the position of stationary menisci two different scenarios for invasion require different conditions. Each case is briefly explained as follows:

Liquid invasion into pores: The pores act as a buffer against free flow of liquid in the network due to their larger radii. This implies that as a meniscus reaches the end of a throat some rise in the pressure is generally required to sustain the flow into the neighboring pore. Referring to the example of Figure 3.5, the condition required is defined as follows:

$$P_{w,6} > P_{w,5} + \frac{\sum_{i=2}^{4} \dot{M}_{v,i}}{g_{w,1}}. \tag{3.4}$$

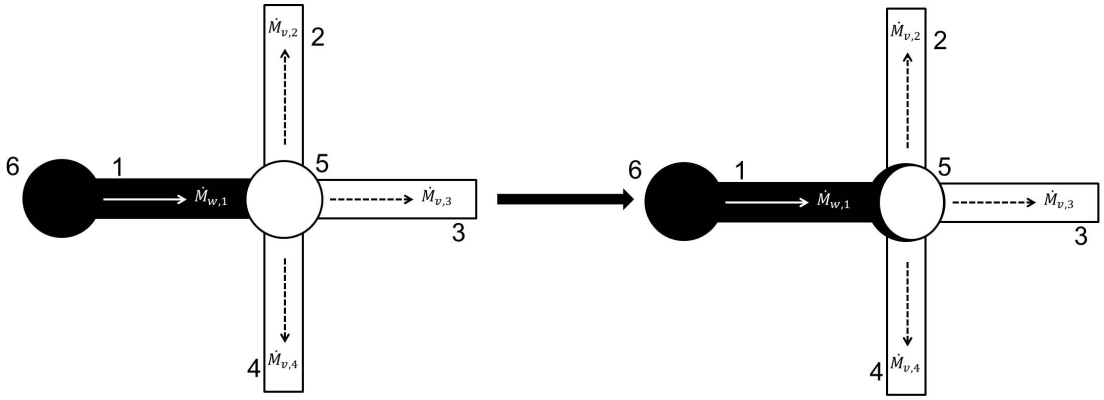

Figure 3.5: Liquid invasion event from a stationary meniscus (throat 1) to an empty pore (pore 5).

Liquid invasion into throats: On the contrary liquid invasion from fully saturated pores into adjacent throats does not require a rise in the pressure. Since the liquid pressure level in the pores is generally higher than in the throats the pressure level should be enough to sustain liquid flow. The respective condition, see Figure 3.6, is:

$$P_{w,5} > P_{w,3} + \frac{\dot{M}_{v,3}}{g_{w,1}}. \tag{3.5}$$

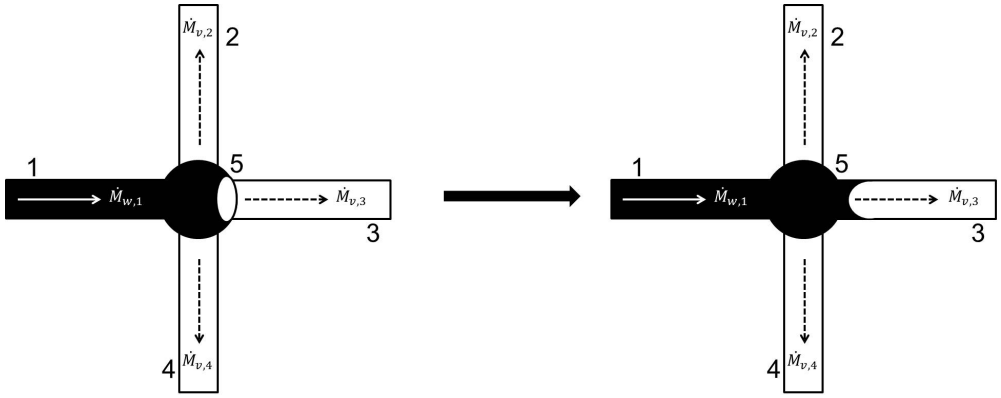

Figure 3.6: Liquid invasion event from a pore with meniscus (pore 5) to a throat (throat 3).

Using these conditions all invasion candidates are identified. However, only one liquid invasion event per cluster at a time should be allowed since invasion is generally followed by important changes in the boundary conditions. This indicates that a single liquid invasion might lead to a significant pressure drop such that the cluster cannot support any further invasions. Therefore, only the most urgent invasion event

(highest pressure difference) per cluster is carried out. Further invasion candidates are investigated only after recalculation of liquid pressure.

Note: As shown by the two equations (Equations 3.4 and 3.5) describing the conditions for a successful invasion, liquid pressure should be sufficient to ensure that the evaporation loss in the new throat is compensated. However, due to the formation of a new meniscus (usually in a small throat), the average liquid pressure in the cluster drops considerably. As a result, the anticipated outcome may not always appear, meaning that a newly formed advancing meniscus will recede. This is an important issue whose main cause is evaporation and which occurs more frequently at higher drying rates. These unsuccessful invasions are dubbed as "unsustainable invasions". They imply that the liquid cluster does not have high enough liquid pressure to sustain further invasion in the current time-step. A solution is proposed below.

Note: In rare cases liquid invasion leads to merging of clusters which were separate in the previous time-step. To understand this effect it should be noted that the new invading menisci are supported by a tiny amount of liquid (in this thesis 10^{-6} of the respective geometry's volume). In case the invaded throat or pore has an empty volume of less than the specified amount, the invasion event leads to the connection of liquid phase from potentially two different clusters. Thus it is essential to relabel liquid clusters after each invasion event.

Recovery

Ideally, in order to predict successful liquid invasion, knowledge of liquid pressure after an invasion event is required. This is due to the fact that the formation of menisci has a strong impact on liquid pressure in the entire cluster. To this goal, immediately after an invasion, liquid pressure is calculated. If the pressure at the nearest liquid pore is not sufficient to sustain this invasion the whole process should be reversed. Then, not only the liquid phase distribution is adjusted but also the liquid pressure is restored to its previous value.

Another important role of the recovery is to prevent further unsustainable invasion in the current time-step. As explained before, during each invasion check the most urgent case per cluster is selected indicating that if that specific liquid invasion cannot be sustained, other invasion events will not be sustainable as well in this time-step. Therefore, upon encountering an unsustainable invasion recovery is carried out and the corresponding cluster is prohibited from further invasion in the current time-step.

Note that liquid invasion provides new menisci (consequently new boundary conditions) in liquid clusters. It is essential that liquid pressure is updated after all

invasion events have taken place. However, a mandatory part of the liquid pressure field calculation is to identify the stationary menisci since the introduction of new menisci by invasion could force the prior stationary menisci to change their state. Therefore four steps need to be carefully followed to calculate liquid pressure and detect future invasion possibilities. These steps are recapitulated in the flowchart of Figure 3.7.

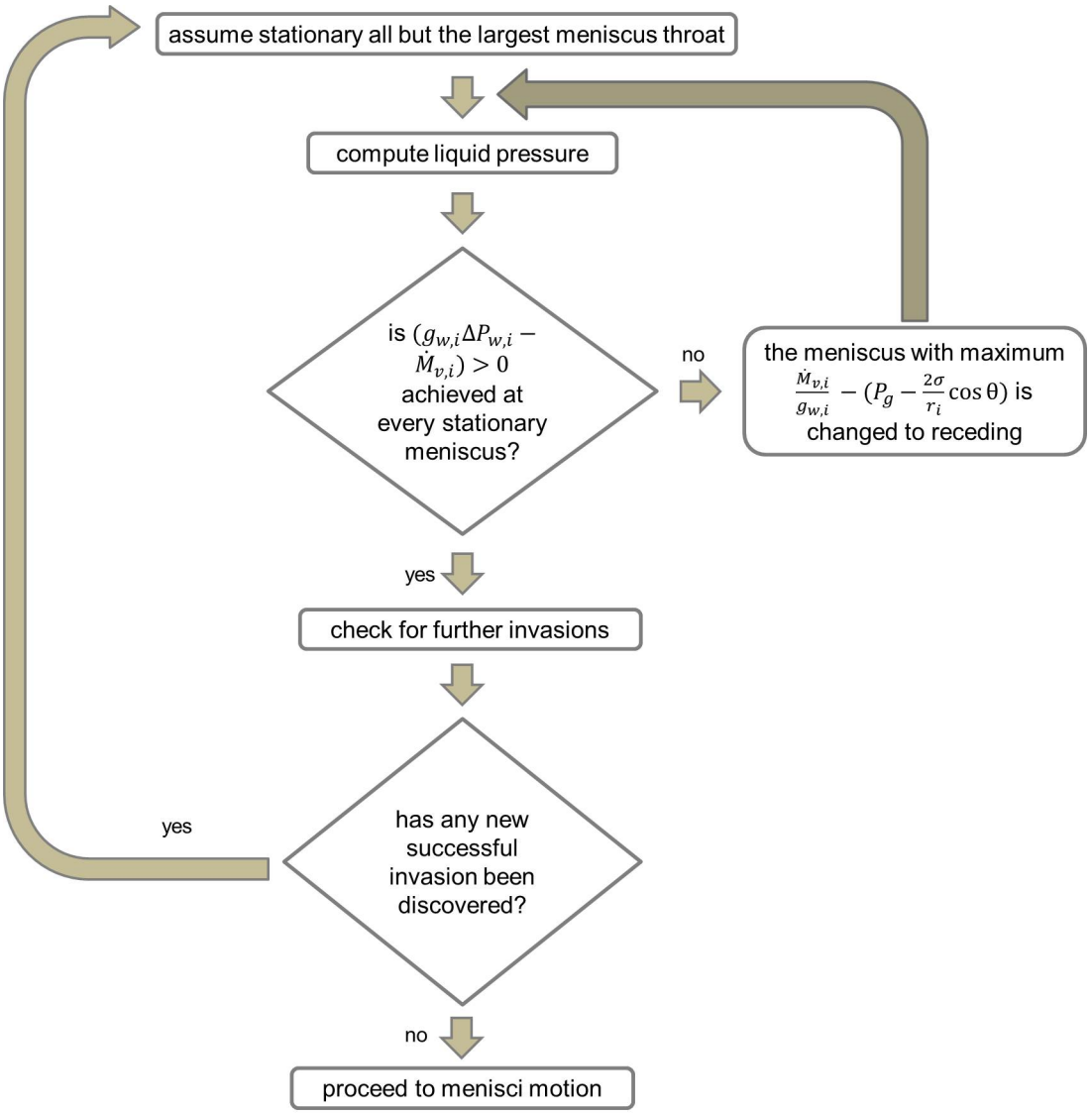

Figure 3.7: Flowchart of liquid invasion-liquid pressure calculation sequence.

As discussed in Chapter 2, a global time-step ends when the boundary conditions for either the system of equations 2.3 and/or the system of equations 2.7 change. In this model due to the introduction of pores, time-step calculations should account for filling or emptying of pores with menisci, in addition to that of throats. In this

case, since liquid phase in pores may be connected to several throats the net liquid flow in the pores should be calculated. Simultaneously, evaporation rate in empty adjacent throats is supplied by pores which can contribute to the time-step (Figure 3.8). Depending on whether the amount of liquid in a specific pore is increasing or decreasing one of the following equations is applied to define time-step corresponding to that pore:

$$\Delta t_5 = \frac{(1 - S_{p,5})V_{p,5}\rho_l}{\sum_{i=incoming} \dot{M}_{w,i} - \sum_{j=outgoing} \dot{M}_{w,j} - \sum_{k=empty} \dot{M}_{v,k}}, filling \tag{3.6}$$

$$\Delta t_5 = \frac{S_{p,5}V_{p,5}\rho_l}{\sum_{i=incoming} \dot{M}_{w,i} - \sum_{j=outgoing} \dot{M}_{w,j} - \sum_{k=empty} \dot{M}_{v,k}}, emptying \tag{3.7}$$

where S_p is saturation state of the corresponding pore.

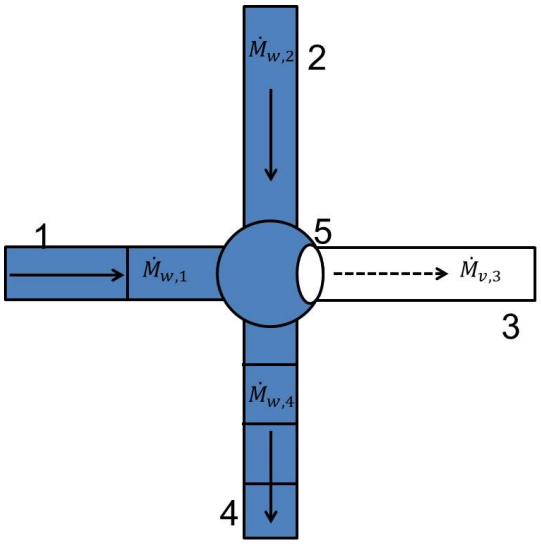

Figure 3.8: Schematic of a partially filled pore exposed to evaporation.

Global time-step is defined as the minimum time required for the first pore or throat to be emptied or filled. In the case that the elements are emptied the meniscus recedes to the adjacent element and new boundary conditions are assigned accordingly in the subsequent time-step.

3.2.2 Salt migration and crystallization model

An identical approach to the ion transport model as in Chapter 2 has been adopted here. In the throats a 1D advection-diffusion equation describes ion transport.

The computation grid has been adaptively discretized by utilizing the finite volume method for each sub-element in the throats. An explicit solution approach provides salt time-steps according to advection and diffusion stability criteria. The final equation for a generic sub-element (located in the middle of a throat see Figure 3.9) is:

$$\frac{C_i^{new} - C_i^{old}}{\Delta t} = u\frac{C_{i-1}^{old} - C_i^{old}}{L_i} + D\frac{C_{i+1}^{old} - 2C_i^{old} + C_{i-1}^{old}}{L_i^2}. \tag{3.8}$$

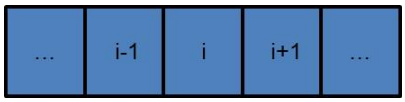

Figure 3.9: Schematic of sub-elements for salt computations within a throat.

Note: The factor "2", which was identified to be necessary for diffusion between a throat with no sub-divisions and volumeless nodes (see Equation 2.11), should not be applied if the two subsequent elements have volume. This factor appears when half the length of the sub-element and the radius of the respective pore are added together to calculate the diffusion path as shown in Equation 3.10.

On the contrary, ion transport in the pores is neither a 1D problem nor can it be described by plug flow. However, considering the assumption of perfect mixing made about pores, mentioned in Section 3.2.1, a separate governing equation for the pores can be proposed. Said perfect mixing assumption allows for attribution of homogeneous concentration to each pore. Equation 3.9 gives the variation of salt concentration within pore 5 in Fig. 3.10 as function of advection and diffusion:

$$\frac{C_5^{new} - C_5^{old}}{\Delta t} = \frac{3}{4\pi r_5^3}\Big(\sum_{i=1}^{2} u_i A_i C_{i,1}^{old} - C_5^{old}\sum_{j=3}^{4} u_j A_j + \sum_{k=1}^{4} D A_k \frac{C_{k,1}^{old} - C_5^{old}}{\frac{L_{k,1}}{2} + r_5}\Big). \tag{3.9}$$

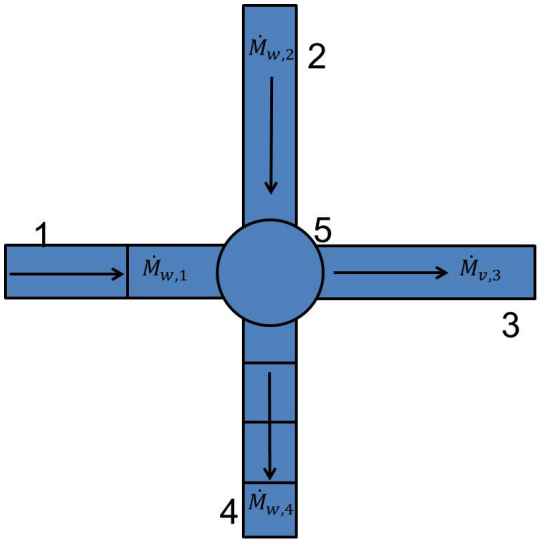

Figure 3.10: Schematic of a spherical pore 5 with neighboring throats divided into sub-elements for salt calculations.

Note: Pores are not discretized in ion transport calculations. They act as single numerical elements which theoretically may have up to 4 neighboring sub-elements. The governing equation for the mentioned sub-elements, at the entrance of throats, is defined differently. For example, the concentration at sub-element 1 of throat 4 from Figure 3.10 reads:

$$\frac{C_{4,1}^{new} - C_{4,1}^{old}}{\Delta t} = u\frac{C_5^{old} - C_{4,1}^{old}}{L_{4,1}} + D\Big(\frac{C_{4,2}^{old} - C_{4,1}^{old}}{L_{4,1}^2} + \frac{C_5^{old} - C_{4,1}^{old}}{L_{4,1}(r_5 + \frac{L_{4,1}}{2})}\Big). \tag{3.10}$$

Note: Pores with neighboring empty throats are exposed to evaporation (Figure 3.11). Salt concentration in such pores is affected by evaporation as an extra factor. Since the volume of liquid in these pores is not constant during the time-step, the change in pore saturation should be accounted for, thus transforming Equation 3.9 to Equation 3.11:

$$\frac{C_5^{new} - C_5^{old}\frac{S_5^{old}}{S_5^{new}}}{\Delta t} = \frac{3S_5^{new}}{4\pi r_5^3}\Big(\sum_{i=1}^{2} u_i A_i C_{i,1}^{old} - C_5^{old} u_3 A_3 + \sum_{k=1}^{4} D A_k \frac{C_{k,1}^{old} - C_5^{old}}{\frac{L_{k,1}}{2} + r_5}\Big), \tag{3.11}$$

where Equation 3.12 gives the value of S_5^{new}:

$$S_5^{new} = S_5^{old} + \frac{3(\sum_{i=1}^{2}\dot{M}_{w,i} - \dot{M}_{w,4} - \dot{M}_{v,3})\Delta t}{4\pi r_5^3}. \tag{3.12}$$

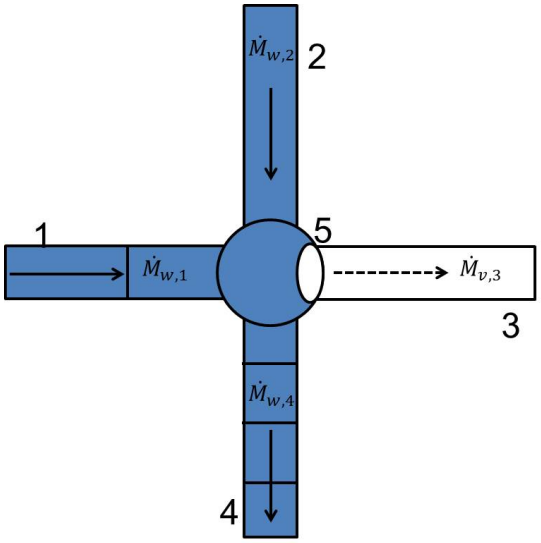

Figure 3.11: Schematic of a partially filled pore 5 exposed to evaporation and neighbor to throats divided into sub-elements.

Salt time-step calculations should account for pores as new elements. Defining salt time-step for pores based on the stability criterion is not as apparent as for throat sub-elements. Therefore we resorted to the basic definition of stability criterion. According to this definition, the time must not exceed what is required for concentration to be replaced by the neighboring element. Thus salt time-step for the pores is formulated as the minimum of the two following values (refer to Figure 3.10):

$$\Delta t_{i,adv} = \frac{\frac{4}{3}\pi r_i^3}{\sum_{j=1}^{2} u_j A_j}, \tag{3.13}$$

$$\Delta t_{i,diff} = \frac{(r_i + \frac{L_{4,1}}{2})^2}{4D}. \tag{3.14}$$

Note that the shortest diffusion length (the throat with most sub-elements $L_{3,1}$) is selected to ensure stability for diffusion case.

Coupling equations for all throat sub-elements and pores, a system of algebraic equations is established. The explicit solution scheme provides new values of salt concentration as a function of current values and salt time-step:

$$\begin{bmatrix} C_{t,1}^{new} \\ C_{t,2}^{new} \\ \vdots \\ C_{t,Nt}^{new} \\ C_{p,1}^{new} \\ C_{p,2}^{new} \\ \vdots \\ C_{p,Np}^{new} \end{bmatrix} = \begin{bmatrix} C_{t,1}^{old} \\ C_{t,2}^{old} \\ \vdots \\ C_{t,Nt}^{old} \\ C_{p,1}^{old} \\ C_{p,2}^{old} \\ \vdots \\ C_{p,Np}^{old} \end{bmatrix} + \begin{bmatrix} A_{c,1,1} & A_{c,1,2} & \dots & A_{c,1,Nt+Np} \\ A_{c,2,1} & A_{c,2,2} & \dots & A_{c,2,Nt+Np} \\ \vdots & \vdots & \ddots & \vdots \\ A_{c,Nt+Np,1} & A_{c,Nt+Np,2} & \dots & A_{c,Nt+Np,Nt+Np} \end{bmatrix} \times \begin{bmatrix} C_{t,1}^{old} \\ C_{t,2}^{old} \\ \vdots \\ C_{t,Nt}^{old} \\ C_{p,1}^{old} \\ C_{p,2}^{old} \\ \vdots \\ C_{p,Np}^{old} \end{bmatrix} \Delta t_{salt}. \tag{3.15}$$

Matrix A_c contains all the contributions from adjacent elements which can be obtained from equations 3.8 and 3.9.

After the new salt concentration profile in the network has been obtained, supersaturation values must be checked in order to discover the potential crystallization zones. This part of the model is identical to that of the previous chapter (see Section 2.2.3 and Equation 2.15). However, the important point to be made here concerns the reservoir at the network surface. Since the evaporation from the wet surface pores is attributed to the reservoir (instead of direct evaporation from the sessile droplet surface which is not included in this model), ion enrichment due to this evaporative loss should be accounted for. This rise may continue to the point of exceeding saturation concentration, which leads to crystallization in the reservoir. But as per abstract representation of the reservoir, the total mass of crystals formed here is distributed uniformly among all adjacent throats.

3.2.3 Comparison

The current wetting-drying model is based on the previous model of Rahimi et al. [87]. Although the two models look very similar in concept, the new algorithm is distinctly different from the old one. Addition of spherical pores instead of nodes with no volume has assisted enormously in improving the algorithm in several areas which will be mentioned in this section. These improvements range from difficulties in modeling to more smooth liquid flow pattern in the network. Moreover, the new model captures some effects which could not be captured by the previous model due to its geometry, and some unwanted effects have been eliminated. These improvements are discussed alongside some simulation results in this section.

Introduction of salt to the wetting-drying network model provides the possibility to

simulate the impregnation process starting with an initially dry network. The same model can be utilized to model spray agglomeration processes by assigning relevant operating parameters. The second part of the comparison is focused on the disparity between the wetting-drying-crystallization model and the drying- crystallization model of Chapter 2. The said drying-crystallization model requires simulations to start with a pre-saturated network. Therefore, instead of a reservoir supplying the liquid to the network, simulations need to be modified to initiate with a saturated network. The two models have theoretical similarities, yet depending on simulation conditions they may vary significantly in results. The wetting-drying model has higher versatility in the application, needless to say, that many more effects are captured in this model.

Addition of spherical pores

The distinctions between the current model and the previous model of Rahimi et al. [87] are separated into two categories: a) model and algorithm improvements, b) simulation results and various effects.

Improvements in modeling and algorithm had the purpose of tackling several issues observed in the model of [87]. These difficulties would not have been resolved if not using the new geometry which includes volume at throat junctions in the form of spherical pores. Different areas where the algorithm has been significantly changed are as follows:

1. Liquid invasion: In Section 3.2.1 two scenarios for liquid invasion have been introduced, namely from partially filled pores or from a stationary meniscus in a throat. The issue here concerns the latter case. The presence or absence of volume at the junctions leads to different scenarios for each model. In the new model, the meniscus propagates forward into the adjacent pore and later on the liquid may branch into the adjacent throats after the pore is filled (Figures 3.5 and 3.6). In the old model, due to lack of volume at nodes, the meniscus springs over the node and into a relevant throat where liquid pumping can be sustained (Figure 3.12). The scenario of the new model seems more realistic and helps to sustain the continuity of the liquid phase which is entangled with the next point that shall be mentioned.

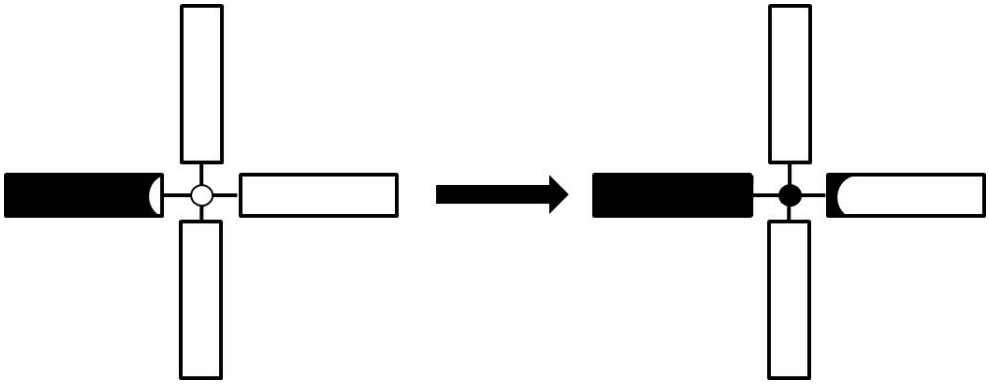

Figure 3.12: Illustration of liquid invasion from a stationary meniscus for the model of Rahimi et al. [87].

2. Liquid breakage: This discrete event refers to the splitting of continuous liquid phase which takes place at partially filled nodes (liquid nodes with gas in the vicinity) forming a meniscus in the neighboring throat (Figure 3.13). Liquid breakage is an essential part of the old model which has been scrapped altogether by addition of spherical pores. In the old model, the criterion for a liquid breakage event was defined by liquid pressure and evaporation. If the liquid flow could not be sustained, by careful comparison of all possible scenarios, the most urgent cases were selected for breakage. Presence of liquid volume in the pores of the current model renders liquid breakage events obsolete. In the new model, if a pore with a meniscus exhibits lack of liquid flow, the meniscus recedes to the point that potentially the pore dries out completely and menisci are formed in the adjacent throats. This may take place during one or few time-steps (since it is not a discrete event anymore) as shown in Figure 3.14.

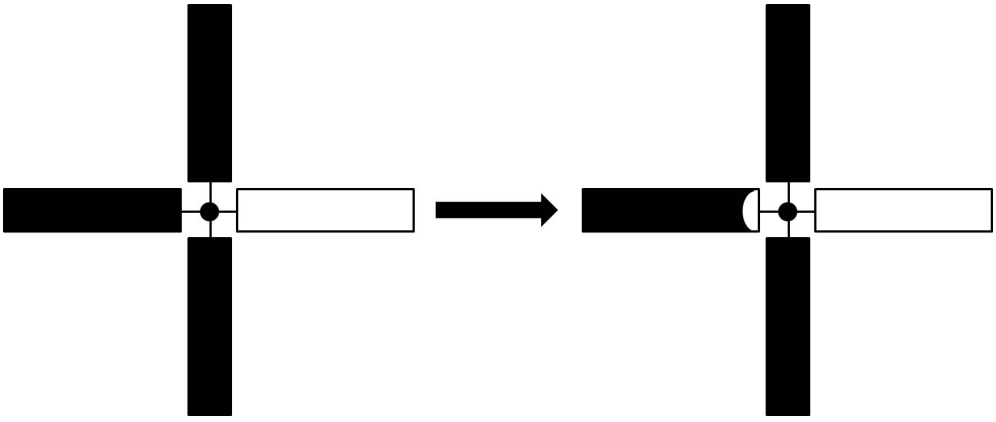

Figure 3.13: Illustration of liquid breakage at a so-called partially filled pore for the model of Rahimi et al. [87].

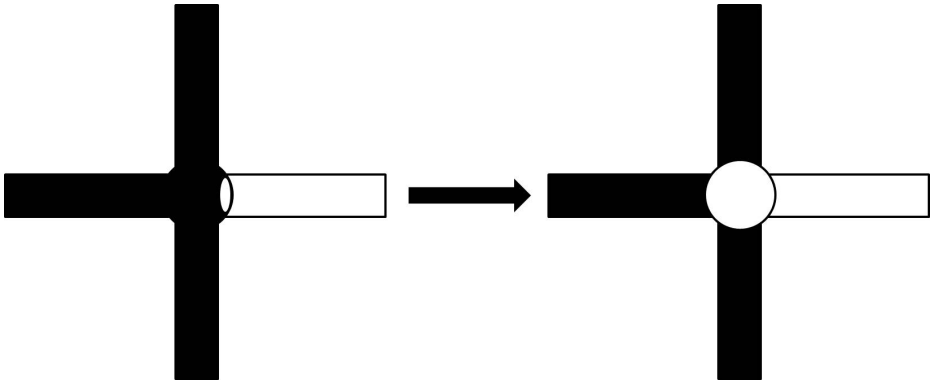

Figure 3.14: Schematic of emptying a meniscus pore within the span of one or several global time-step.

3. Unsustainable events: Unsustainable events refer to discrete events (liquid invasion or liquid breakage) which are reversed at the same or next time-step. An example of this case was presented in Section 3.2.1, and the procedure denoted by "**Recovering**" is designed to tackle the issue. However, countering unsustainable events, in the old model, proved to be a challenge for which no direct solution could be found. In a pragmatic approach to solve the problem, the specific cases responsible for these unsustainable events were identified and blocked for several time-steps (either invasion or breakage). The goal was to allow for the liquid cluster to readjust the pressure level in a manner that said events can be sustained. Nonetheless, this pragmatic solution raises two issues. Firstly, the number of time-steps needed for blocking specific events is completely arbitrary, with no criterion to determine whether too many blocking time-steps have been chosen. The second issue is related to computational time. With each appearance of an unsustainable event, all the calculations regarding the corresponding time-step are rendered irrelevant. As a result, frequent occurrence of unsustainable events significantly affects the efficiency of the model.

4. Networks with bimodal size distribution: In previous work on pore network modeling of drying, various simulations were carried out using networks with predefined patterns of macro-throats in order to study certain effects [65] [66]. In the old model, we encountered a problem while attempting to run such simulations. As menisci are capable of moving across to other throats, it is not possible to capture the expected effect of macro-throats from these simulations. Figure 3.15 illustrates how vertical macro-channels are supposed to inhibit horizontal movement of liquid. However, liquid invasion events enable the liquid to spring over the nodes in the old model, essentially connecting the clusters (Figure 3.15 (a)).

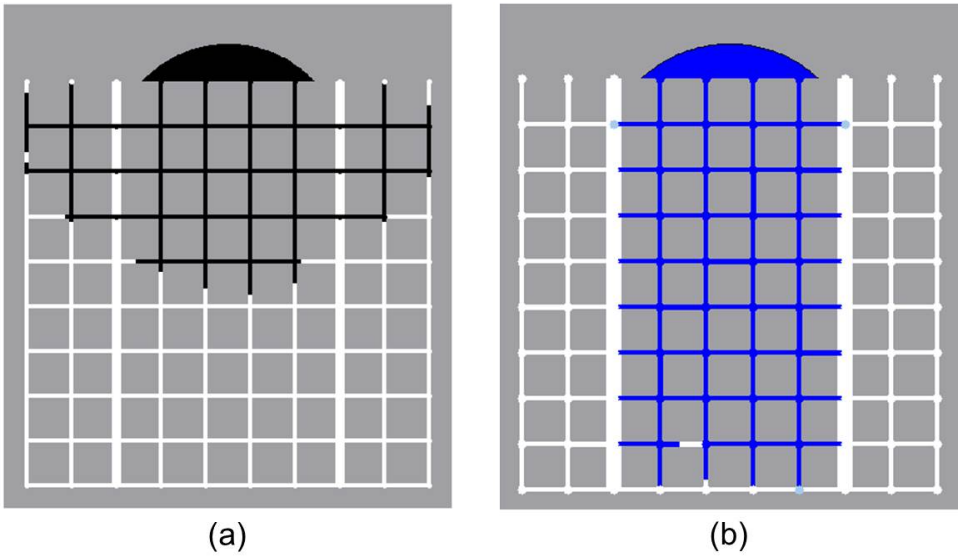

Figure 3.15: Phase distribution for networks with vertical macro-channels for: (a) no volume at throat intersections, and (b) spherical pores connecting adjacent throats.

This flaw in the model was first addressed by implementing two rows of macro-throats which are connected by other macro-throats, as shown in Figure 3.16. The connected macro-throats act in this case as a pressure buffer which prevents the liquid to simply jump over and connect neighboring micro-porous regions and respective liquid clusters.

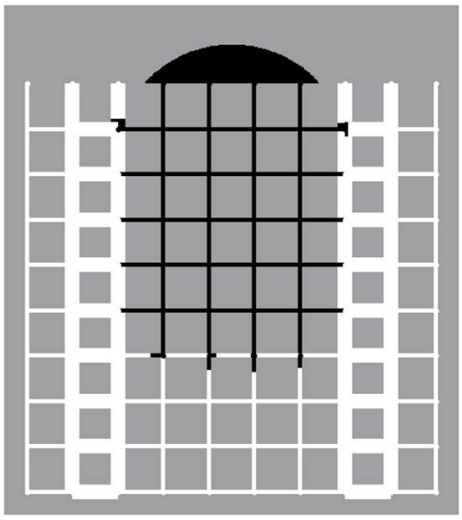

Figure 3.16: Phase distribution for network from the model of [87] with two parallel vertical macro-channels.

However, this issue is automatically solved in the current model, by introduction of volumes at the pores (Figure 3.15 (b)). So long as the pore radius is larger than the

radius of the largest neighboring throat (in this case macro-throat), the pore will act as a barrier against liquid flow. The invasion event will only take place after the liquid pressure has risen high enough to overcome this higher level.

Now that we have established the improvements and benefits regarding the algorithm in the current model, some comparison with the simulation results of the old model will be carried out. The aim is to run simulations on close to identical networks to make the comparison as fair as possible. To this goal, the physical radius of the pores will be decoupled from the capillary pressure they exert. In this way, the volume of the pores can be reduced to a minimum (due to time-stepping pore volume cannot be completely neglected), which is insignificant numerically. As a result, the total void volume for the two networks is nearly identical, so that network porosity is expected to have no significant role in the comparison of the two models. Side by side phase distribution plots for identical network saturations are shown for the sake of comparison in Figure 3.17. The radius multiplier for capillary pressure values at pores, for the illustrated simulation results in Figure 3.17 (d) to (f), is set to 1.1. The network size has been considered 10 by 10, and other simulation parameters are identical to those of Table A.1 and A.4. The parameters defining the drying rate are identical to those of slow drying from Table A.2.

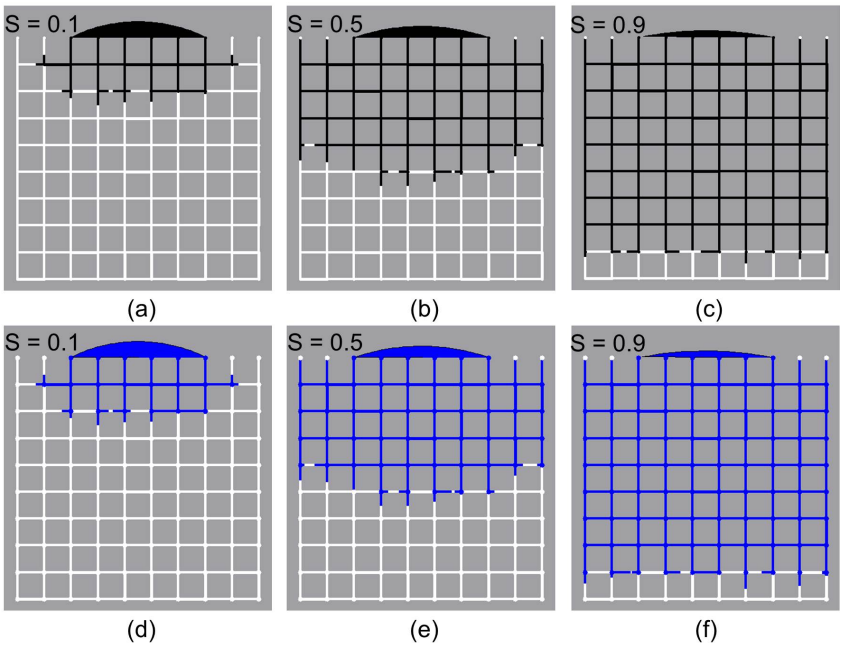

Figure 3.17: Phase distributions in the wetting stage for similar networks by application of the wetting-drying algorithms with: (a) to (c) nodes with no volume, and (d) to (f) spherical pores.

It can be observed that during the wetting stage, phase distributions for the two algorithms look very similar (Figure 3.17). It is expected that due to the strong effect of the droplet (high liquid pressure compared to that of the menisci) the role of pores as pressure barrier is minimized. This means that as the droplet depletes and no more free liquid is available at the network surface, the influence of pores should increase. Therefore, more diverse phase distributions are obtained in Figure 3.18.

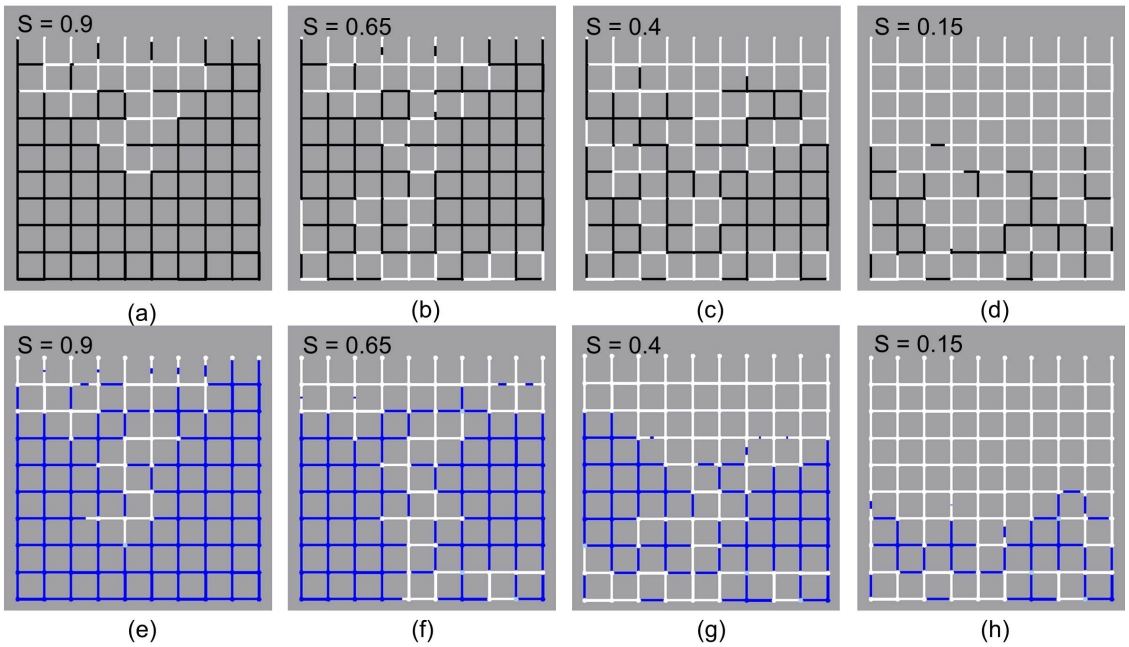

Figure 3.18: Phase distributions during the drying stage for similar networks by application of the wetting-drying algorithms with: (a) to (d) nodes with no volume, and (e) to (h) spherical pores.

Phase distributions computed by the old and the new models, in the drying stage, indeed appear to be very different (Figure 3.18). Generally, the liquid is scattered all over the network in the case of the old model with volume-less nodes which may be attributed to the deficiency of the breakage event. In this case, the liquid clusters are less dense and the liquid has spread which is attributed to the ease of liquid movement due to lack of stabilizing pressure at throat junctions. The formation of a much larger number of gas pockets as shown in Figures 3.18 (b) and (c) is a testament to this analysis. However, the most striking dissimilarity between the two models is the liquid remaining connected to the surface until late stages of drying (in case of the old model). This effect is due to the fact that throats are not isolated from the main cluster in a proper way. In the old model, liquid connection along the nodes with neighboring empty throats can be maintained for a long period of time (until breakage event separates the liquid phase); whereas inclusion of higher pressure

at the throat junctions (pores in the new model) leads to the emptying of menisci pores to be prioritized. For example, following liquid connection from the surface to the depth of the network (main liquid cluster) in Figure 3.18 (c), a considerable number of pores with empty neighboring throats can be seen. This unrealistic high connectivity of liquid does not seem to be reasonable.

In order to further investigate the effect of pores as a pressure barrier, the induced pressure by these pores has been increased in a step-wise manner. The aim is to quantify how the liquid penetration height (the minimum distance from the bottom that liquid is found) and width of the main liquid cluster (the maximum distance for lateral liquid spreading) evolve as more resistance against liquid flow is exerted. The network size, as well as the droplet volume, have also been increased to 50×60 and 3×10^{-17} m^3 to reach more reliable conclusions. The rest of the parameters have remained constant as in the simulations of Figures 3.17 and 3.18 (found in Tables A.1 and A.4).

It can be seen that the physical time required for same liquid penetration depth and the main liquid cluster width are elevated with increasing pressure barrier at the pores. This effect is very important as the droplet and network size are enlarged since the longer free liquid is present at the surface, the more liquid is lost due to evaporation. This effect is potentially more substantial as drying rate increases leading to much less penetrated liquid. In order to keep the details in the graphs visible only three cases are plotted in Figures 3.19 and 3.20. The time needed to reach the largest size of the cluster for all simulations is shown in Table 3.1.

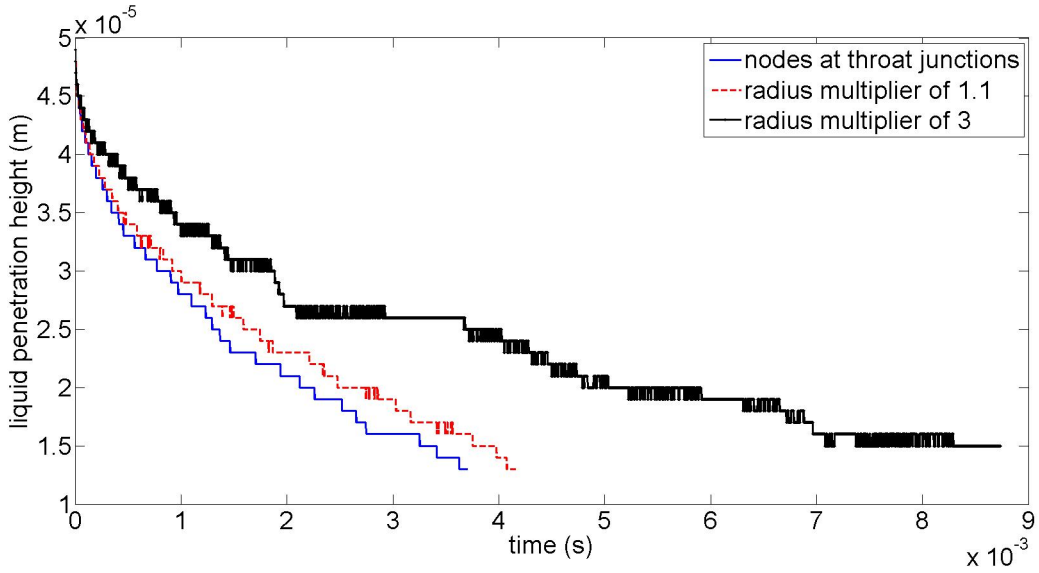

Figure 3.19: Penetration depth over time for increasing pressure at throat cross-sections.

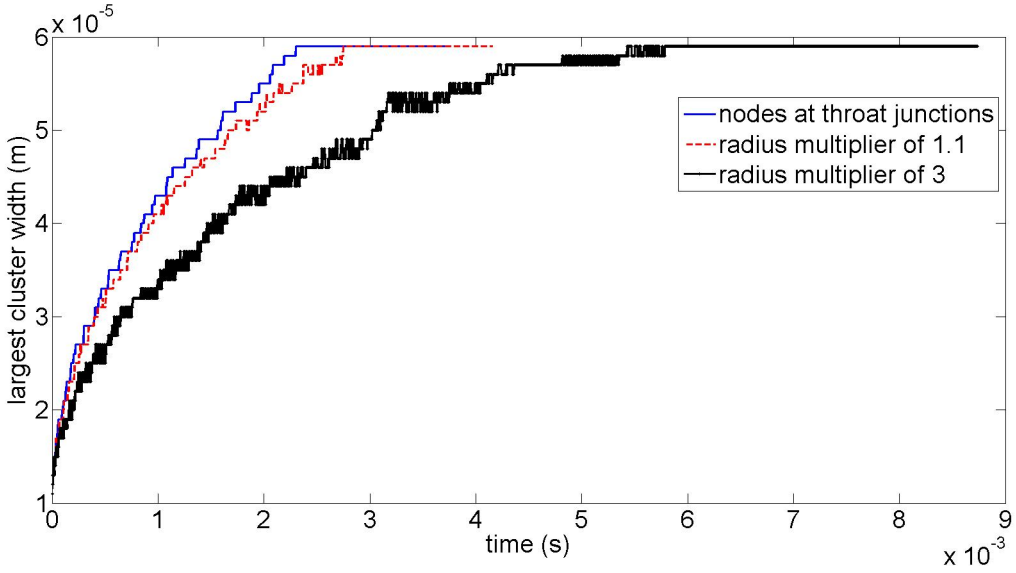

Figure 3.20: Width of main liquid cluster over time for increasing pressure at throat cross-sections.

Table 3.1: Minimum time required to reach the maximum cluster width for increasing pressure at the pores.

radius multiplier	0 (old model)	1.1	1.2	1.3	1.4	1.5	1.7	2	2.5	3
time (ms)	2.3	2.8	2.8	2.8	2.7	3	2.7	3.3	4.5	5.4

As the data (Table 3.1) suggests, the inclusion of pressure barrier at pores increases the imbibition time (from 2.3 to 2.8 ms). Despite increasing pressure at pores, the physical time for liquid imbibition, then reaches a plateau before it starts to rise again for radius multipliers larger than 2 according to Table 3.1). This finding suggests that unless the pores are sufficiently large, their effect on imbibition remains constant.

Effect of liquid migration on crystallization

Salt solution infiltration from a reservoir exposed to evaporation has direct effects on crystallization pattern. However, in this section, we aim to investigate the influence of allowing liquid migration to dry regions of the network (enabled by the wetting-drying algorithm) on crystallization pattern via comparison of the new wetting-drying-crystallization model and the drying-crystallization model of Chapter 2. As shown in Section 2.3, simulations with the drying-crystallization model

always start with a saturated network. In that model, liquid may flow between different regions within the same liquid cluster but throats that dry out can never be refilled again. This also implies that liquid clusters cannot merge once they split into smaller ones. In short, the liquid flow in that model is more restricted compared to the wetting-drying model presented in this chapter. At the same time, the improvements discussed in the previous section, due to the addition of spherical pores, allow the new wetting-drying algorithm to be more realistic. Please note that from this point on, the notation wetting-drying model only refers to the new model (which includes spherical pores at throat junctions) presented in the current chapter in Section 3.2.1.

Considering that the initial settings for simulations with the two models are different, some modifications are required for the sake of running comparable simulations. Firstly, the wetting-drying model is modified to start simulations with an initially saturated network. The second point, namely the lack of volume at throat junctions, also encountered in the previous comparison in this section, is caused by the difference in pore geometries between the two models. Decoupling of pore radii and their induced capillary pressure shall address that issue and leads to almost identical pore geometry for both cases. Values for simulation parameters are selected identical to those used in simulations earlier in this section (see Tables A.1 and A.4). The radius multiplier for pore induced pressure, corresponding to the wetting-drying model, is set to 1.1 .

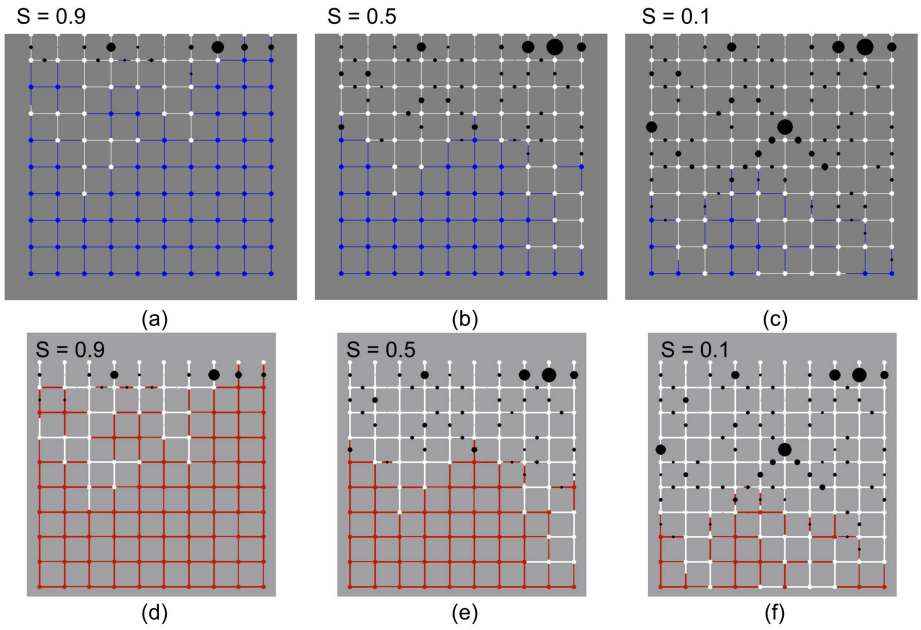

Figure 3.21: Comparison of phase distributions for identical networks and saturations between: (a) to (c) drying-crystallization model of Chapter 2, and (d) to (f) wetting-drying-crystallization model of Chapter 3.

It can be observed that barring slight disparity, due to the excess salt solution at pores as pore volume cannot be set to zero (see Section 3.2.3), the results look essentially identical for the same network saturation as shown in Figure 3.21. Salt mass profile at the end of the simulations is plotted for both cases, showing very close qualitative agreement (Figure 3.22). Note that slices are defined by summing up the values for one row of vertical and horizontal throats, adjacent to each other, starting from the bottom of the network. This similarity between the results of these two models indicates the necessity of the inclusion of a pressure barrier at throat junctions for the wetting-drying model, judging from the significant disparity between the old wetting-drying model and the new one.

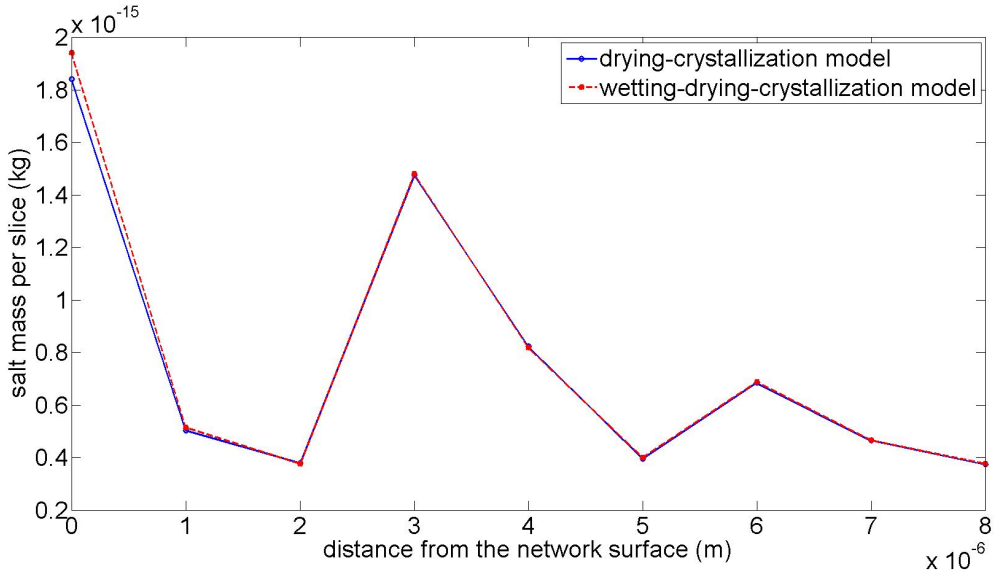

Figure 3.22: Salt mass profile at the end of simulation for drying-crystallization model of Chapter 2 (solid line) and wetting-drying-crystallization model of Chapter 3 (dashed line).

More in-depth analysis of the data is possible through statistical representation of salt mass per throat. Table 3.2 shows the mean and variance of the mass of salt per throat, as well as the total amount of salt at the end of each simulation. Note that, as mentioned in the former paragraph, the total mass of salt in the simulation with the wetting-drying model is slightly higher (by around 2 %) compared to the other case, which is due to the extra initial volume of the liquid provided by pores.

Table 3.2: Statistical representation of salt mass distribution at the end of the simulations for drying-crystallization model and wetting-drying-crystallization model.

simulation	mean salt mass (kg)	salt mass variance (kg)	total salt mass (kg)	computation time (s)
drying	4.06×10^{-17}	7.36×10^{-33}	6.94×10^{-15}	14.9
wetting-drying	4.14×10^{-17}	7.66×10^{-33}	7.08×10^{-15}	42.1

It is worth mentioning that for normalized results, the mean value of salt mass per throat will be identical (5.85×10^{-2}) for both simulations whereas the wetting-drying model has a higher variance of data (1.08×10^{-19}) compared to the model of Chapter 2 (1.06×10^{-19}). This indicates that the salt is more dispersed in that simulation. One might argue that as the ratio of liquid volume in the pores and throats varies,

the distribution pattern may be altered significantly. However, the only approach to quantify such effects is through simulations with enough realizations as the networks will be intrinsically different if physical pore volume is considered. This is a difficult task given the long computational time of the wetting-drying model at least with the current setup. The computation times reported are for simulations run with Matlab 2013 on a computer with processor Intel Core i7 5820K over-clocked at 4.2 GHz.

3.3 Simulation results

In this section, the capabilities of the current model will be demonstrated by various simulations. In Chapter 2, we obtained a basic understanding of the drying of networks initially saturated with salt solution. However, the infiltration process may alter some effects as well as further complicating previous scenarios. The influence of various parameters on simulation results will be presented in this section. Similar to Chapter 2, for the sake of comparison all simulations are carried out using the same network. Additionally, the effect of pore geometry has been studied via a network with bimodal pore size distribution in Section 3.3.4. It should be mentioned that all simulations use 2D networks due to relatively long computational time.

3.3.1 *Fast drying and high initial concentration*

Fast drying generally leads to a shorter lifetime of the reservoir which results in less penetration of liquid into the network in total. Simultaneously, salt concentration in the reservoir increases due to evaporation from the connected surface pores as discussed at the very end of Section 3.2.2. Figure 3.23 (c) shows that a significant amount of crystals is formed in the reservoir at the end of the wetting stage. Similarly, other surface throats exhibit crystallization during the wetting stage even earlier than the reservoir (Figure 3.23 (a)). This phenomenon takes place due to comparatively less liquid volume in the throats (than reservoir) leading to faster enrichment of the ions at the same evaporation rate. The wetting stage ends with liquid in the network having a decreasing concentration gradient towards the depth (see Figure 3.25).

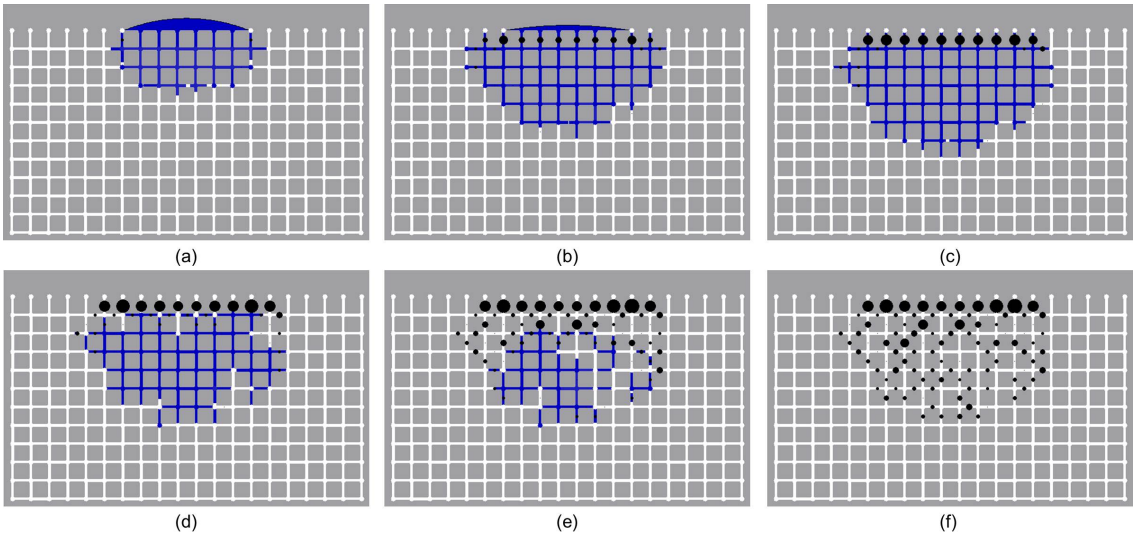

Figure 3.23: Phase distribution for fast drying and high liquid concentration obtained from simulation with wetting-drying-crystallization algorithm for network saturations of: (a) 15 %, (b) 30 %, (c) 41 % in wetting stage and (d) 30 %, (e) 15 %, (f) 0 % in drying stage.

The drying stage starts with a quick recession of the drying front at the very beginning as a result of fast drying. Therefore, crystals are formed only due to local evaporation of liquid with limited capillary pumping. A Significant amount of crystals is observed at the network surface as ions, in the supplied liquid, are already concentrated during the wetting stage. Liquid cluster shrinks rather homogeneously from different sides demonstrating the degree to which capillary pumping is limited. In the end, a homogeneous distribution of the salt in the interior network is obtained due to strong viscous resistance, limiting advective transport of ions to the evaporating zones, leading to local crystallization.

3.3.2 *Slow drying and high initial concentration*

Slow drying allows significantly more liquid volume to infiltrate the network due to less evaporative loss. This is directly tied with the enrichment of the liquid that is supplied to the network by the reservoir. As shown in Figure 3.24 (a) to (c) no crystallization takes place during the wetting stage which also indicates that the concentration gradient is smoother than in the fast drying case as demonstrated by the solute concentration profiles in Figure 3.25.

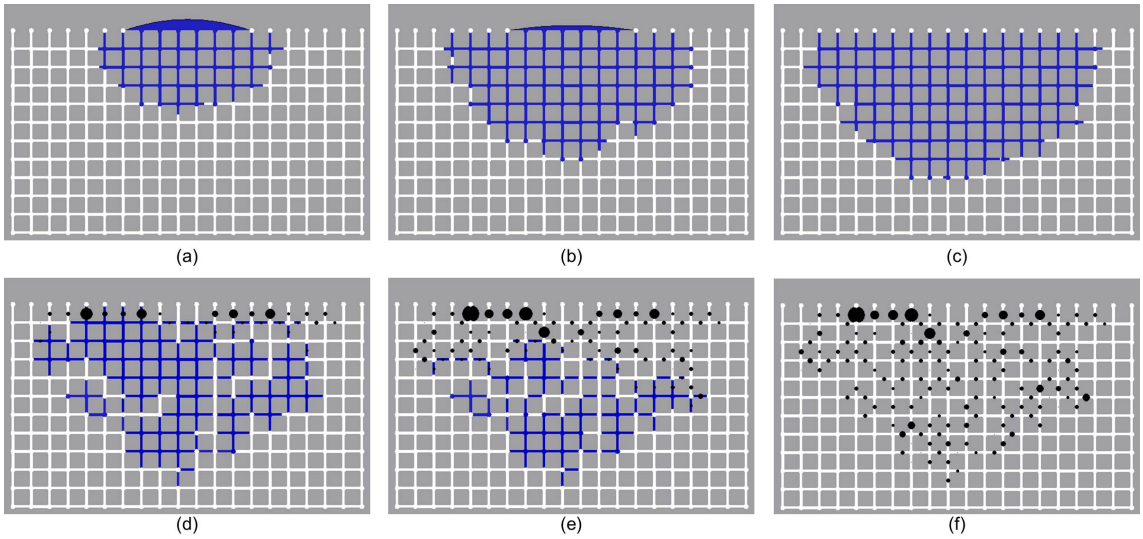

Figure 3.24: Phase distribution for slow drying and high salt concentration obtained from simulation with wetting-drying-crystallization algorithm for network saturations of: (a) 15 %, (b) 30 %, (c) 41 % in wetting stage and (d) 30 %, (e) 15 %, (f) 0 % in drying stage.

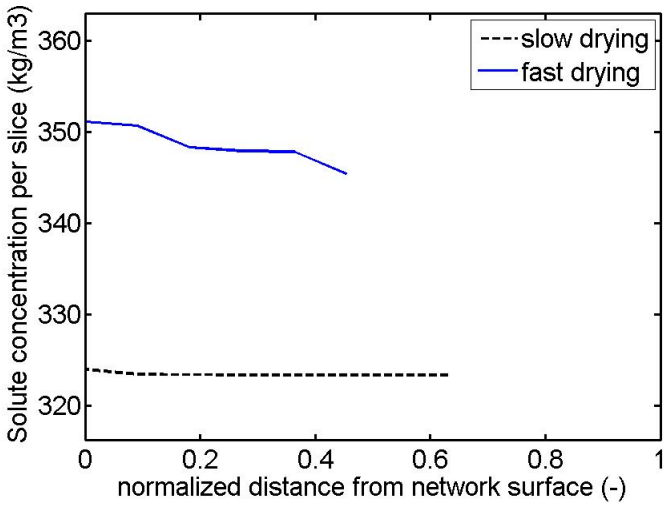

Figure 3.25: Solute profiles over the normalized network depths.

Capillary fingering regime is established at the beginning of the drying stage. A significant amount of ions is transported to the network surface which is well expected in the capillary dominated regime. As liquid breaks down into more clusters, capillary pumping is limited and network surface starts to dry out. However as liquid migration may still redistribute the liquid, the penetration depth increases (secondary infiltration) and salt crystals are formed deeper in the interior network. The final crystallization pattern illustrates how a significantly larger region is impregnated as

a result of slow drying. Subflorescence is homogeneously distributed in the network depth while the surface contains the highest portion of the crystals.

3.3.3 *Slow drying and low initial concentration*

Liquid flow pattern is identical in this case (Figure 3.26) compared to that of the previous simulation results in Section 3.3.2 (Figure 3.24) which allows for a fair assessment of the role of diffusion. Salt is initially less concentrated in the reservoir (lighter shades) allowing for a higher concentration gradient to build up before the saturation limit is reached. Consequently, crystallization is postponed until almost halfway through the drying stage.

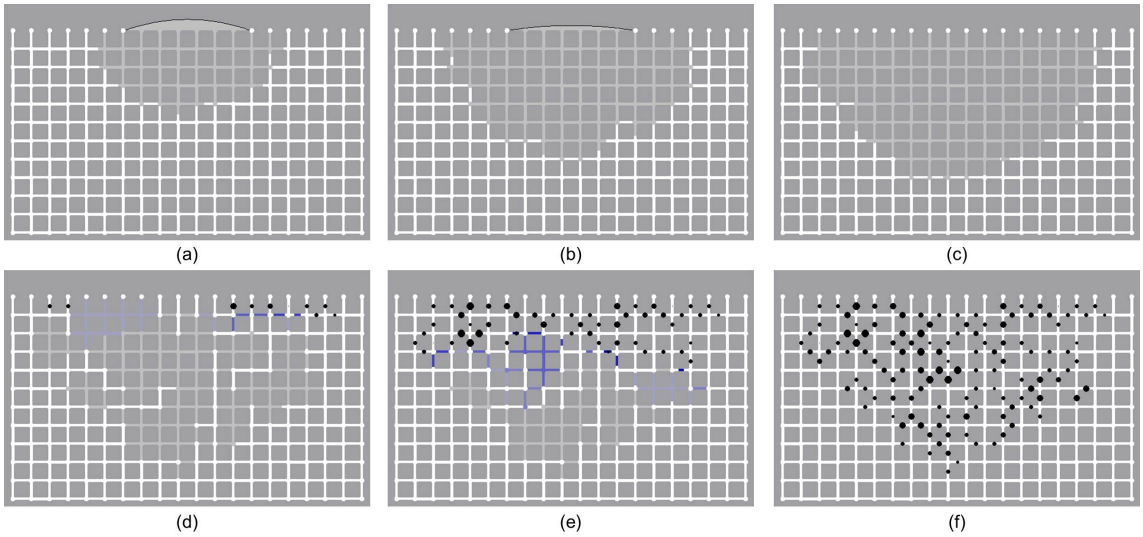

Figure 3.26: Phase distribution for slow drying and low salt concentration obtained from simulations with wetting-drying-crystallization algorithm for network saturations of: (a) 15 %, (b) 30 %, (c) 41 % in wetting stage and (d) 30 %, (e) 15 %, (f) 0 % in drying stage.

Less crystal mass is found at the network surface with even fewer throats exhibiting crystallization. The majority of the salt is crystallized in the interior of the network (subflorescence) since back-diffusion transports the ions to the deeper regions of the liquid cluster. These simulation results show the most homogeneous salt distribution throughout the entire network almost entirely resulting from more significant role of diffusion.

3.3.4 *Network with vertical and horizontal macro-channels*

One of the most important novelties of the wetting-drying model, compared to the model of Chapter 2, is the opportunity of rewetting of dry regions of the network. This effect, which could not be demonstrated in the comparison in Section 3.2.3, due to minimizing liquid volume at pores, is best displayed in simulations where significant variation in spatial pore size is present. For example, comparison of Figures 3.27 (c) and (d) highlights that at the end of the wetting stage, the area covered by liquid clusters is much smaller than at the beginning of drying as liquid from the macro-region invades the smaller throats. As long as high pressure in the liquid cluster is maintained by the reservoir, liquid can remain in the macro-channels and propagates into the network (Figures 3.27 (b) and (c)). As soon as the reservoir depletes, lack of a sustaining pressure causes the liquid at large menisci of the macro-throats to escape that region (Figure 3.27 (d)). Therefore, the microporous region between macro-channels is invaded by liquid, leading to much larger liquid cluster area.

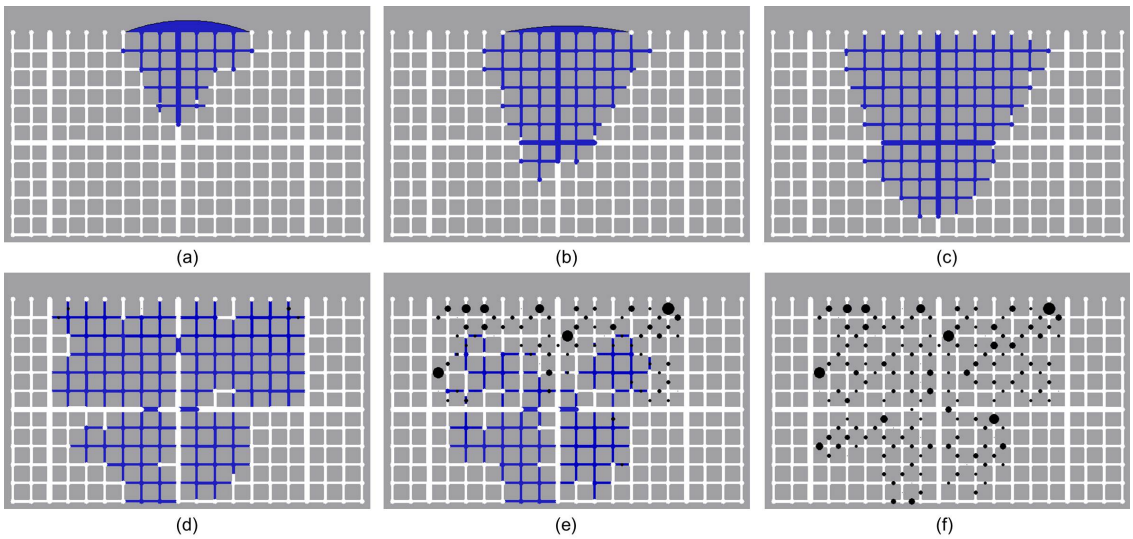

Figure 3.27: Phase distribution for slow drying and high initial salt concentration produced by wetting-drying-crystallization algorithm. Network comprises of microporous regions separated by vertical and horizontal macro-channels. Results are shown for network saturations of: (a) 10 %, (b) 20 %, (c) 31 % in wetting stage and (d) 30 %, (e) 15 %, (f) 0 % in drying stage.

It is worth mentioning that liquid infiltration is significantly enhanced for this case since the reservoir is connected to a macro-channel with much higher liquid conductivity than the micro-throats. Consequently, the liquid flows a lot faster into the network by capillary pumping as shown in Figure 3.28 for the wetting stage and the slow drying case.

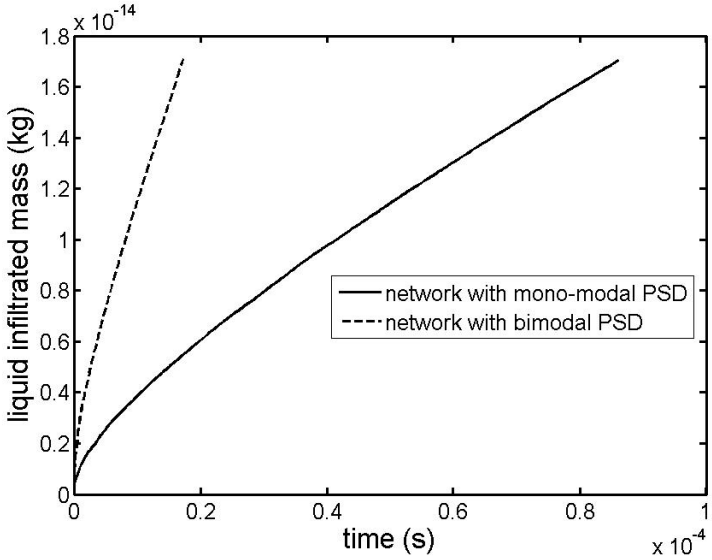

Figure 3.28: Mass of infiltrated liquid during the wetting stage for networks with mono-modal and bimodal PSD.

Figure 3.27 suggests that despite the effect of macro-channels in the formation of segregated liquid clusters, the largest portion of crystal mass is still found in the first slice. However, the amount of subflorescence is significantly increased compared to that of the network with mono-modal pore size distribution (Figure 3.29). It is also important to notice the lack of crystallization within the macro-channels as the liquid is generally pumped away before exposure to evaporation and ion enrichment.

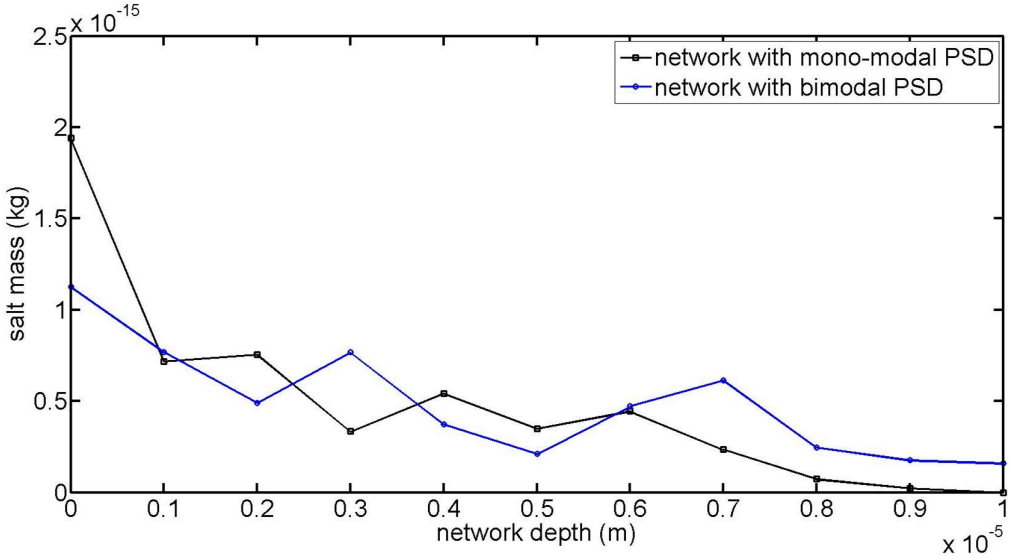

Figure 3.29: Salt mass profiles for slow drying of highly saturated salt solution in networks with bimodal and mono-modal PSD.

Decreasing the initial salt concentration has drastic results for this specific pore network. It is shown that salt crystals distribution is much more homogeneous with a decrease in the variance of normalized crystal mass in throats being reduced by 60 % (Table 3.3). The phase distribution plots for said low initial concentration are shown in Figure B.5.

Table 3.3: Statistical presentation of final salt mass distribution for simulations with high and low initial concentration of networks with vertical and horizontal macro-channels.

initial concentration ($kg \cdot m^{-3}$)	mean crystal mass (kg)	variance of crystal mass (kg)	mean normalized crystal mass	variance of normalized crystal mass
323.4	8.29×10^{-18}	5.47×10^{-34}	0.0015	1.78×10^{-5}
71.9	1.84×10^{-18}	1.69×10^{-35}	0.0015	1.11×10^{-5}

These simulations can very well recapitulate the novelty and findings of this model for various cases. In order to avoid repetition, phase distribution plots for more simulations of networks with bimodal pore size distribution are presented in the appendix B.

3.4 Conclusion

In this chapter, a 2D pore network model has been developed that couples the algorithms for wetting, drying, and salt transport-crystallization. The void space of the material has been approximated by cylindrical throats which are connected through spherical pores. The addition of volume at throat intersections helps to better track the liquid-gas interface inside the network and significantly improves the algorithm. Ion migration in the throats is modeled by a 1D advection-diffusion equation whereas perfect mixing is assumed inside the pores (finite volume method). Throats are discretized with respect to the local Pe number and the ion transport equation addresses each sub-element individually. These equations are coupled and solved using an explicit solution scheme and time-stepping. Crystallization occurs at the end of each salt time-step in case the salt concentration exceeds the saturation concentration.

The merits of this model are highlighted by comparison with two other models. Improvements in the wetting-drying algorithm are explained by comparison to the model of Rahimi et al. [87]. The main point of difference between the two models is

the inclusion of spherical pores as opposed to nodes with no volume. The comparison is kept consistent by decoupling capillary pressure at the spherical pores and pore radii. Simulations have been carried out more smoothly and the results appear more consistent for the new model. Moreover, simulations with networks of bimodal pore size distribution are much more flexible in this case. Furthermore, the current model has been compared to the drying-crystallization model of Chapter 2. Although the wetting-drying-crystallization model proves capable of simulating more effects, the increased computational time limits the reachability of this model compared to the simpler drying-crystallization model.

Pore network simulations are carried out for various drying rates, initial salt concentration, and pore size distributions. It is observed that slow drying leads to a rather homogeneous crystal distribution in the network with slight accumulation at the exterior. On the contrary, in the case of fast drying, a considerable amount of crystals are formed in the reservoir before the primary infiltration comes to an end. This mass of crystals is distributed among the throats beneath the reservoir. As the initial salt concentration in the reservoir decreases, the crystallization pattern becomes more uniform. The influence of pore size distribution is studied by introducing macro-throats with a distinct hierarchical pattern in the network. The tendency of crystals not to grow within macro-channels is demonstrated in these simulations. Diffusion effect is a predominant factor for cases that a number of liquid clusters are isolated due to horizontal macro-channels and not evaporating. As a result, clusters which are not exposed to evaporation (in the depth of the network) are provided with enough time for concentration gradients to level out by diffusion. Moreover, it is shown that within each microporous region few larger crystals are formed in the vicinity of macro-channels.

Interesting results have been obtained from these simulations. Nevertheless, it is transparent that the size chosen for these networks is not ideal; needless to say, that all simulations are in 2D configuration. It has been mentioned that due to the addition of many new effects in this algorithm (compared to that of Chapter 2), the efficiency of the model should be affected. Indeed at the end of Section 3.2.3 a comparison between computational times shows an increase by around 3 times. In that section, it was concluded that this model is a lot superior to the old wetting-drying model of Rahimi et al. [87], with a significant discrepancy between the phase distributions, especially in the drying stage. However, later in the same section, the model of Chapter 2 was compared to this new model and the results were in good agreement with each other. It is, therefore, concluded that unless certain effects, such as rewetting of dry regions, are pronounced in the system (e.g. bimodal PSD), the more efficient model of Chapter 2 can produce acceptable results. The model

has room for improvement in several areas such as cluster labeling algorithm and solution scheme for ion transport equations.

Chapter 4

Modified 3D drying-crystallization pore network model

In Chapter 2, 2D simulation results have been presented for several cases which help to explain the mechanisms involved in crystallization during drying of porous media. Few points as to why these results deviate from expectations, suggested by experiments and the literature, have been mentioned at the end of Section 2.4. In this chapter, our aim is to tackle those issues, as well as possible, and to present results that are more representative of real porous materials. To this goal, the drying-crystallization model of Chapter 2 (nodes at throat junctions) is adopted due to its significantly higher computational efficiency compared to the model of Chapter 3. However, the first and most important modification is to extend the pore network to three dimensional configuration. It is also crucial that the porosity of the network matches that of common porous materials. Additionally, the effects of network size can be minimized to a great extent by implementing periodic boundary conditions in both lateral directions. These points are shortly discussed below and the expected effects are introduced:

1. Coordination number: The main difference between 2D and 3D pore network models is the coordination number for the nodes (in case of regular pore networks). It needs to be mentioned that the throats maintain the same function since they establish connection between the nodes. However, increasing the coordination number for the nodes enhances liquid connectivity within the liquid clusters significantly. A direct result of this change is the formation of fewer liquid clusters as network saturation drops. As discussed in Sections 2.3.2 and 2.3.3 liquid connectivity is the most important factor in crystallization pattern.

2. Periodic boundary conditions: another important modification to the model is the addition of periodic boundary conditions in the two lateral directions which essentially eliminates the effect of network sides. On that note, an additional set of throats is added which connect the pores on the opposite sides of the network. It needs to be mentioned that in simulations of 3D pore networks, the maximum size of the network is rather limited due to the increased computational time. Using periodic boundary conditions aids greatly in opposing some of the effects caused by the small network size.

3. Porosity and evaporation rate: Two major issues mentioned in Chapter 2 are yet to be addressed, namely the small porosity of the network and the huge drop in drying rate at the beginning of the second drying period. While both of the aforementioned issues are improved to some extent in the 3D structure, drastic improvements are not expected. As a result, it was decided to hold the porosity as a criterion and work with the pore size distribution to construct the required geometry. As a result, the void volume occupying the space between two adjacent nodes is now represented by a bundle of throats (instead of a single capillary). All throats in one bundle have uniform size, as shown in Figure 4.2, but the radius distribution between various bundles (the characteristic radius for each bundle) is sampled from a normal distribution function as explained in Section 2.3.1. Said bundles have the same void volume as required by the constant porosity assumption laid before. Consequently, few parameters need to be adjusted and a recipe should be followed so that without introducing new elements to the system the effects may be captured. The step-wise recipe is presented as follows:

- The porosity of the network is defined. The porosity is considered uniform throughout the network.
- The network is divided into Nt number of sections (equal to the number of throats for the same network size when compared to the model of Chapter 2).
- The characteristic radius for each bundle is either selected from a distribution function or sampled from experimental data obtained for a real porous material (e.g. mercury porosimetry).
- Since the porosity and the length of all bundles ought to be uniform throughout the network, the volume is adjusted by increasing the number of throats per bundle to match the desired void volume given by porosity.

Note: The addition of bundles leads to a significant increase in the available area for evaporation compared to the case of single throats. According to Equation 2.1 the cross-sectional area is directly proportional to the vapor transfer rate. Therefore,

it is expected that evaporation rate is, first of all, enhanced during the first drying period; and second, the greater cross-sectional area available for vapor diffusion is expected to prevent the drying rate to suffer from great drop during the transition to the second drying period. These effects are confirmed in fast and slow drying of similar networks with bundles and with single throats as shown in Figure 4.1 for the second effect. The parameters regarding these simulations are listed in Tables A.1, A.2, and A.5 found in the appendix.

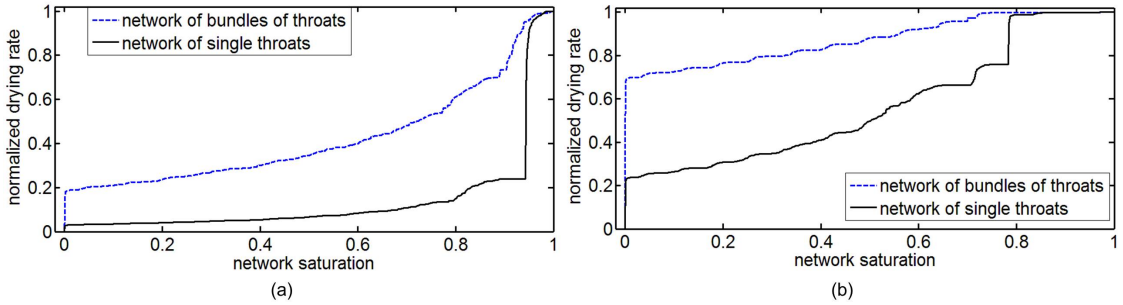

Figure 4.1: Comparison of drying curve between pore network models with bundle of capillaries and with single throats for: (a) fast drying and (b) slow drying.

It can be observed that in both cases, the first drying period is prolonged by the inclusion of bundles in the network. At the same time, the transition from first to second drying period is much smoother for the new network. Therefore, it can be concluded that addition of bundles has greatly improved the issues related to the drying simulations of Chapter 2. The most anticipated effect of the lack of significant drop in drying rate is to see whether the crystallization pattern in the interior part of the network will vary between fast and slow drying rate simulations, as stabilization of drying front should continue until later stages of drying.

Another important effect of the inclusion of bundles, which should not be overlooked, is the improvement of the liquid flow in the network. It has been explained above how vapor transfer is improved in the modified model, but a comparison between bundles with different characteristic radius is missing. Since all bundles have uniform length and void volume, it is evident that the total cross-sectional area, for all the bundles in a given network, is equal. However, the radius of the throats and consequently their number differ for each bundle. Equation 2.1 (Stefan's law) suggests that vapor diffusion rate is directly proportional to the area, i.e. identical total cross-sectional area between bundles leads to equal vapor transfer conductance. On the contrary, the Hagen-Poiseuille equation (Equation 1.5) shows a dependency of the liquid flow rate to the power of four of the capillary radius. As a result, the bundles with larger throats will inherently have higher liquid flow conductance. It is inferred that viscous

effects will drop drastically in the bundles containing larger capillaries. Figure 4.2 shows an example of three different bundles to illustrate the effect of decrease or increase in the characteristic radius of each bundle.Gas conductance is the same for each of the three bundles,

$$g_{v,i} = A_i \frac{\delta}{L_i} \frac{P\tilde{M}}{\tilde{R}T} \propto r_i^2 \quad \Rightarrow \quad g_{v,a} = g_{v,b} = g_{v,c}, \tag{4.1}$$

whereas liquid conductance increases with capillary size,

$$g_{w,i} = \frac{\pi r_i^4}{8\mu_w L_i} \propto r_i^4 \quad \Rightarrow \quad g_{w,a} = 2g_{w,b} = 4g_{w,c}. \tag{4.2}$$

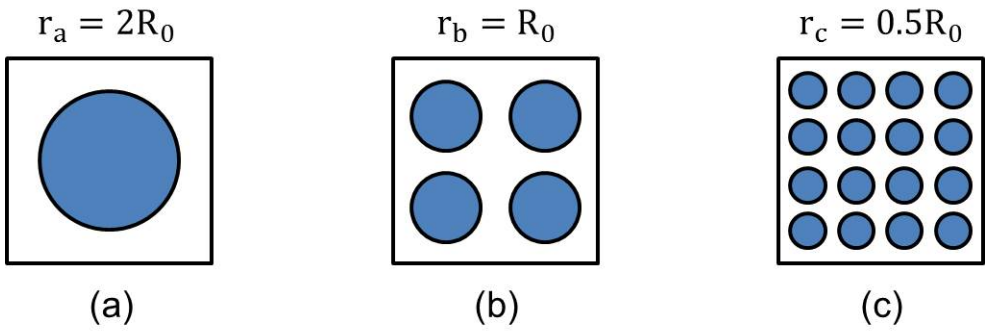

Figure 4.2: Illustration of cross-sectional area of bundles of capillaries with various characteristic radii.

4.1 Monte-Carlo approach

In this part, 3D pore network simulations for different cases will be presented. According to the conclusions drawn from Chapter 2, three different conditions for simulations are selected. The competition between viscous and capillary forces can be investigated by a change in the drying conditions and pore size distribution, which have significant effects on the crystallization pattern. Additionally, as concluded from Chapter 2 and Chapter 3, the initial concentration of the salt plays a strong role concerning ion diffusion in the liquid phase. However, this is only relevant for the slow drying as the diffusion time-scales far exceed those of the fast drying. This fact is especially relevant now that the significant drop between the first and the second drying period is mitigated by model modification, leading to shorter drying times for the fast drying case. Therefore, it is decided to neglect simulations with

low initial concentration and fast drying conditions. On that note, three different conditions for the pore network simulations are selected which are found in Table 4.1. The rest of the simulation parameters, which remain constant for all simulations in this chapter, are presented in Tables A.1, A.2, and A.5 in the appendix section.

Table 4.1: Parameters defining various cases for Monte-Carlo simulations.

case	boundary layer thickness (μm)	drying temperature ($^{\circ}c$)	initial concentration ($kg \cdot m^{-3}$)
(a)	10	80	$0.9C^* = 323.4$
(b)	100	25	$0.9C^* = 323.4$
(c)	100	25	$0.2C^* = 71.8$

It is well established that the results of individual pore network simulations with otherwise identical conditions can vary noticeably among stochastically different realizations of network generation. This implies that in order to generalize and validate some of the conclusions, drawn in Chapters 2 and 3, it is necessary to run simulations with several realizations. For each of the conditions shown in Table 4.1 three sets of Monte-Carlo type simulations, each with ten realizations, are carried out. Characteristic throat radii for each bundle are generated by a normal distribution function (similar to that of Section 2.3). We believe that if network size is sufficiently large, which is denoted as "representative size", the variation between the results of simulations with different networks reaches a minimum. Hence, the network size has been varied for each set of simulations and the variance of the data has been quantified to investigate whether an increase in network size has any meaningful effect.

Within each set of simulations, standard deviation of throat radii is varied which affects capillary flow. It is expected that a wider radius distribution (large standard deviation) produces more capillary effect whereas a narrow distribution is limiting. All the information regarding network geometry is presented in Table 4.2. Network size has been considered as $15\times15\times21$ for large networks and $9\times9\times15$ for the small networks; the first two numbers correspond to the lateral directions (with periodic boundary conditions at both ends) and the third defines the network height.

Table 4.2: Information regarding void space for Monte-Carlo simulations.

distribution	mean throat radius (nm)	throat radii standard deviation (nm)	throat length (μm)	porosity
narrow	200	10	1	0.7
reference	200	20	1	0.7
wide	200	50	1	0.7

Please note that from this point on, the simulations in which the standard deviation for throat radius is 20 nm are denoted as reference for each set of simulations for the sake of comparison. The results are shown in the form of final mass of crystals per slice which is averaged between all the Monte-Carlo type realizations. Slices are defined for the 3D configuration as one row of vertical throats and the adjacent horizontal throats, in both lateral directions, located beneath them. As in Chapters 2 and 3, the first slice is considered at the network surface.

4.1.1 *Fast drying and high initial concentration, case (a)*

Fast drying in 3D pore network configuration, especially considering the addition of bundles, leads to viscous stabilization of the drying front as the network surface dries out at around 90 % global saturation (Figure 4.3). It is therefore inferred that capillary flow of liquid should be very limited, leading to a rather homogeneous distribution of the crystals between vertical slices. However, capillary flow of the liquid is still present to a very small extent which produces a gradient in crystal mass towards the interior of the network in Figure 4.4.

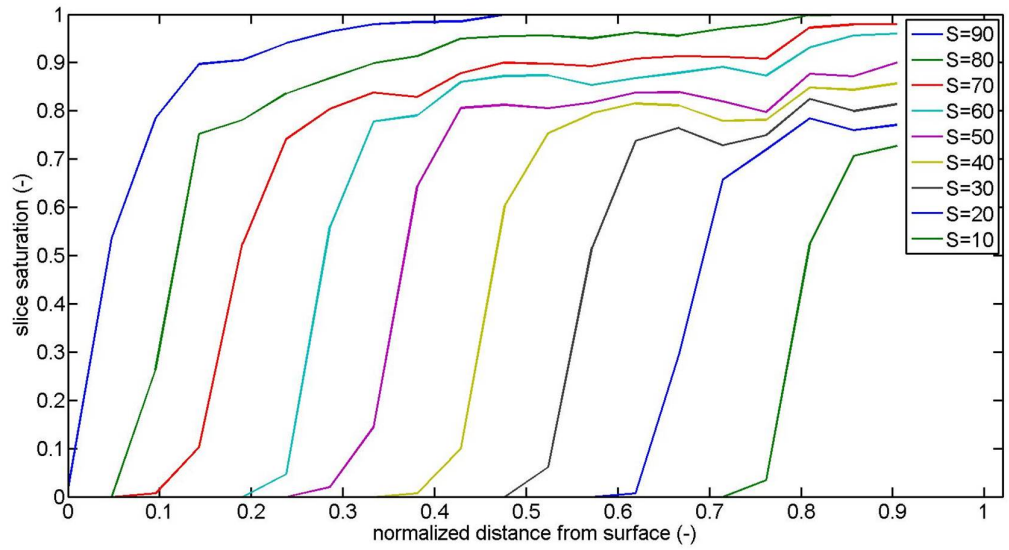

Figure 4.3: Saturation profile in the course of drying for case (a) with throat radii standard deviation of 20 nm.

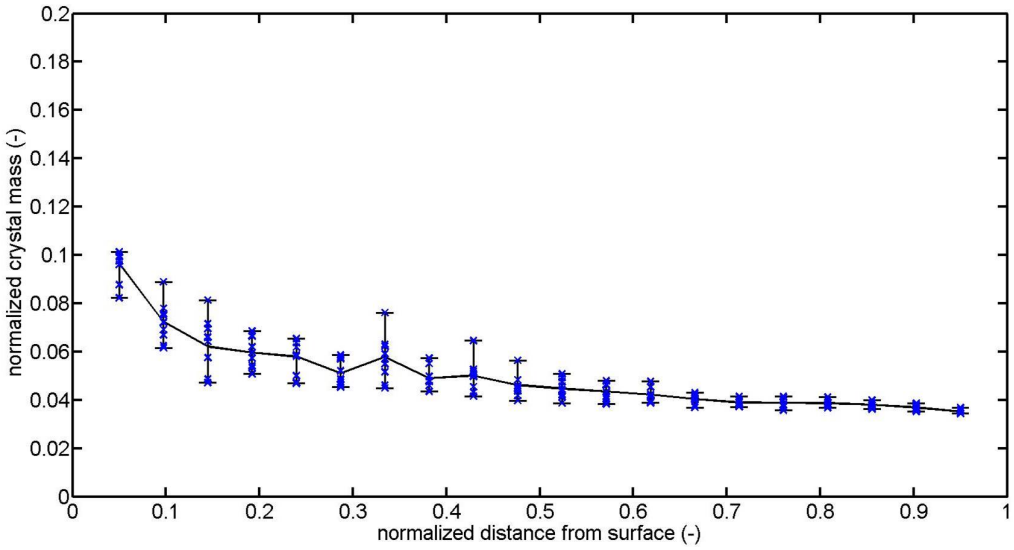

Figure 4.4: Normalized salt mass profile at the end of drying for case (a) with throat radii standard deviation of 20 nm.

Decreasing throat radii standard deviation leads to a more homogeneous network and consequently, capillary pumping will be limited. This effect can be explained by capillary pressure, which depends on throat radius. Capillarity is driven by the pressure gradient in the liquid phase. As the difference between the maximum and minimum throat radii decreases the said driving force, and consequently capillary

flow, becomes smaller. As a result, viscous stabilization should be even more pronounced than the previous case. In Figure 4.5 it is shown that the mass of crystals in the slices is even more homogeneous and the gradient is smoother compared to the previous case.

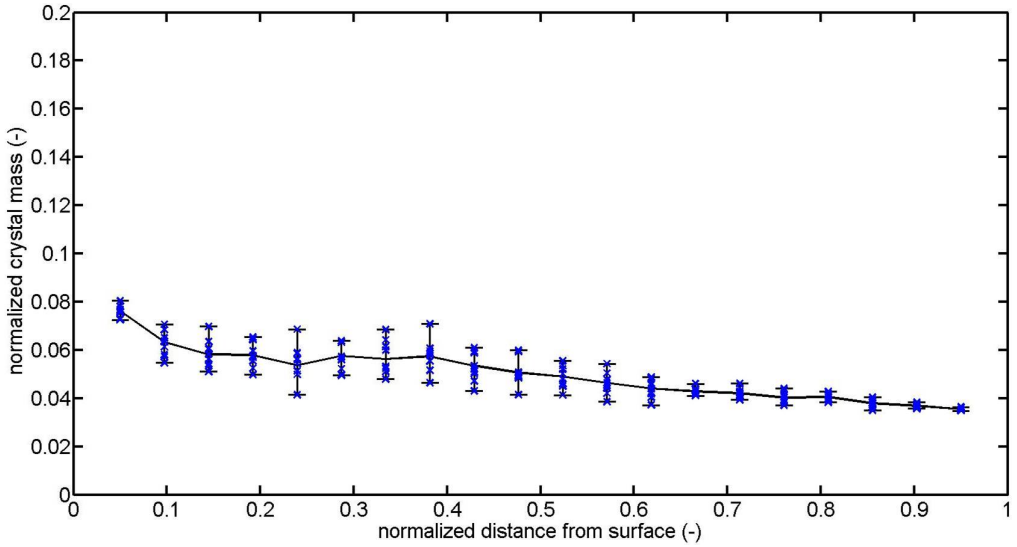

Figure 4.5: Salt mass profile at the end of drying for case (a) with throat radii standard deviation of 10 nm.

Widening the pore size distribution should enhance capillary flow in the system. Opposite to what was explained above, having a wider range of throat radii leads to higher driving force for capillary pumping. As a result, the ion transport in the system should be enhanced and crystals are expected to form at the evaporating regions. These effects can be observed in Figure 4.6. Steeper gradient of salt mass per slice is produced towards the interior of the network and a higher mass fraction of crystals is formed at the network surface.

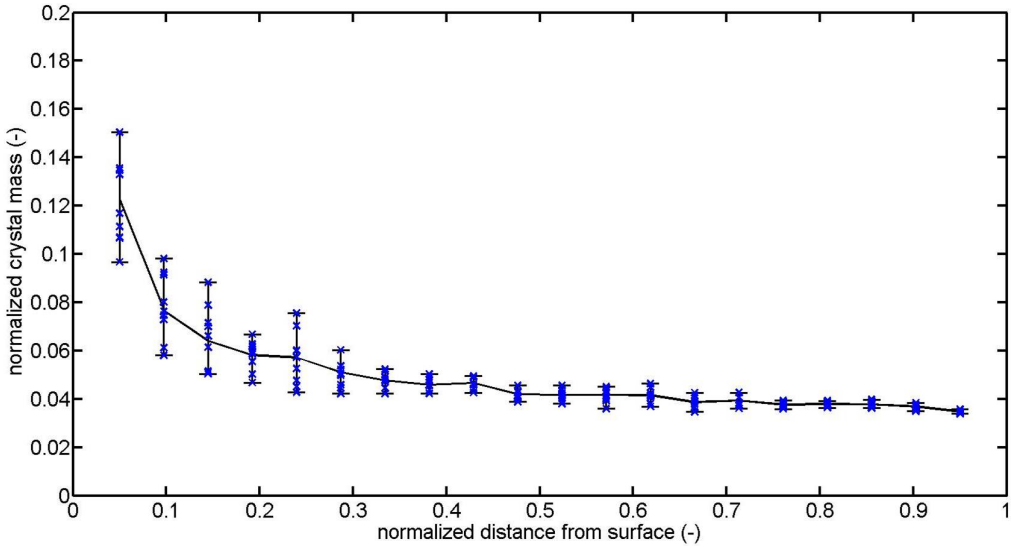

Figure 4.6: Salt mass profile at the end of drying for case (a) with throat radii standard deviation of 50 nm.

The simulation results with wide pore size distribution correlate closely with those found in [10]. The large networks selected in this chapter are more than 4 times larger than what was used in that study. However, the trend shows good agreement in both cases with the surface slice containing almost 3 times more crystal mass as the bottom slices. However, instead of the near surface gradient observed in Figure 4.6, in that study, several slices below the surface show an elevated crystal mass. The profile reported by simulations in this thesis shows slightly better agreement with the relevant experiments from [10].

The reference case (Figure 4.4) shows a significant reduction in the variance of the results as the network size is increased as compared to Figure 4.7 (a). Especially near the network surface there is a big reduction in the randomness of the results for the simulations with larger networks. In the bottom half of the network low variance is observed for both sets of simulations which is probably the result of crystallization in isolated throats.

Similarly to the reference case, decreasing the network size for the narrow throat size distribution leads to an elevation of the variance of results. For this case, the set of simulations with large networks (Figure 4.5) shows the most consistent results, whereas the variance is elevated rather significantly for simulations with smaller networks (Figure 4.7 (b)). in It needs to be mentioned that the variance of the result, in this case, is generally lower than in the reference case where capillary pumping was stronger. The effect of limited capillary pumping is nicely observed for

the smaller networks (see Figure 4.7(b)) where there is a depletion at the network surface. Once again, in a similar fashion to the reference case, the discrepancy among the Monte-Carlo realizations diminishes for the slices in the interior of network.

Wide throat size distribution shows the most randomness when compared to the other sets of simulations for large networks, as seen in Figure 4.6. Therefore, it can be concluded that as capillary pumping is enhanced by widening the range of capillary pressure in the network, the crystallization pattern becomes less predictable. Note that, since the initial concentration of salt is high (90 % of saturation concentration) the crystallization pattern can be analyzed based solely on advection that results from capillary pumping. Similar to both previous cases, simulations with smaller networks have an increased variance in data. We conclude that increasing the network size for case (a) has helped to achieve more consistent results and move to a network size that may be considered representative.

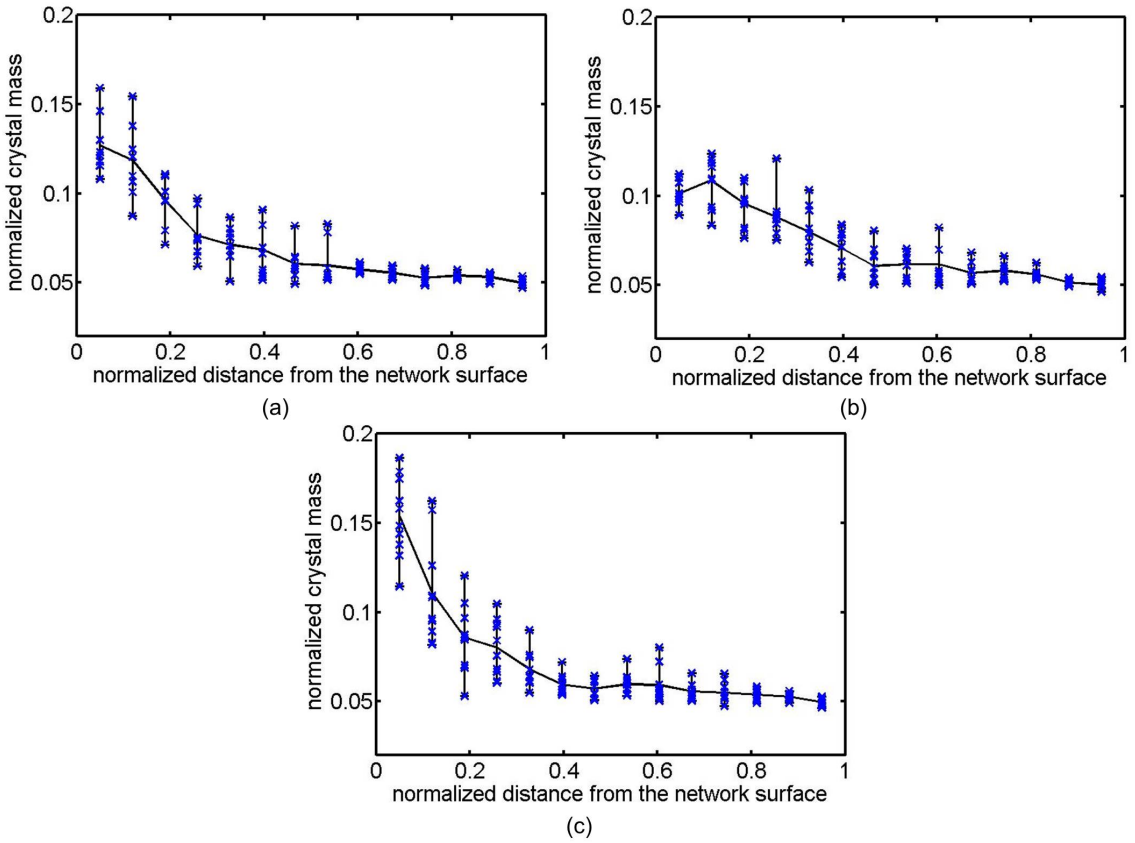

Figure 4.7: Salt mass profile at the end of drying for: (a) reference case, (b) narrow throat radii distribution, and (c) wide radii distribution for case (a) with smaller network size of $9 \times 9 \times 15$.

The mean and variance of the mass of salt among all throats, for the three sets of simulations with large networks are presented in Table 4.3. It can be observed that

the crystals are more dispersed (higher variance) as pore size distribution is widened. This indicates that the width of the pore size distribution is also an important variable to determine the representative size for given simulation variables.

Table 4.3: Statistical presentation of salt distribution at the end of drying for case (a).

throat radii standard deviation	mean mass of salt (kg)	variance of mass of salt (kg)
narrow (10 nm)	7.54×10^{-17}	2.89×10^{-33}
reference (20 nm)	7.54×10^{-17}	3.82×10^{-33}
wide (50 nm)	7.54×10^{-17}	5.24×10^{-33}

4.1.2 *Slow drying and high initial concentration, case (b)*

It has been established so far that decreasing the drying rate significantly enhances the ability for capillary pumping in the network to the point that the capillary fingering regime is obtained. Saturation profiles shown in Figure 4.8 demonstrate that the network surface is kept wet until later stages in the simulation (just below 70 % total saturation). This fact implies that, in the absence of diffusion, around 30 % of the total salt mass should accumulate at the network surface. In fact, this value is around 25 % since the initial concentration is below saturation and back diffusion plays a small role in delaying the crystallization in this case (see Figure 4.9). Homogeneous distribution of the crystals in every slice beneath the surface is also observed for all three sets of simulations in this case. In order to understand this effect, we need to pivot the discussion towards liquid connectivity in the network. It has been mentioned that one of the advantages of 3D pore networks is the higher connectivity of the liquid which can be explained using the information from Figure 4.8 and 4.9. Saturation profiles reveal that after the network surface dries out, the drying front starts to propagate into the network in a pseudo-linear fashion (network saturation of below 70 %). In other words, not too many large clusters of liquid are found. This directly contributes to limiting capillary transport of liquid in the network and crystals are formed locally as a result of direct evaporation of liquid.

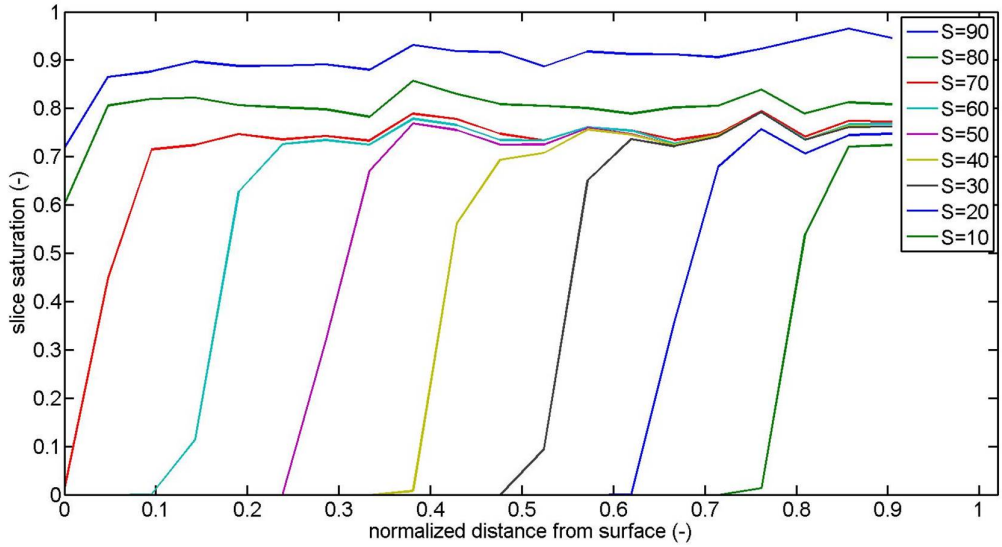

Figure 4.8: Saturation profile in the course of drying for case (b) with throat radii standard deviation of 20 nm.

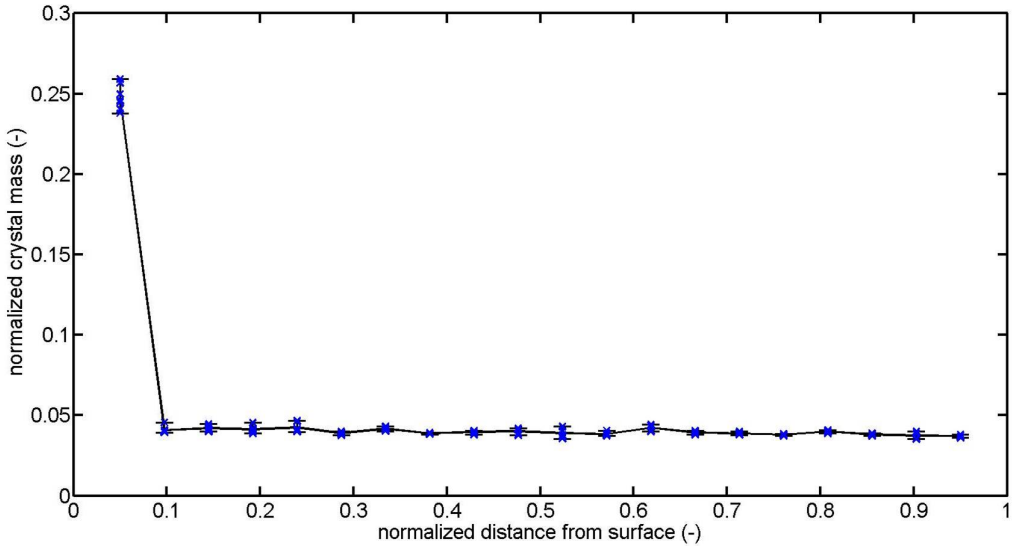

Figure 4.9: Salt mass profile at the end of drying for case (b) with throat radii standard deviation of 20 nm.

Additionally, it should be mentioned that the variance of the results is significantly lower for these sets of simulations hinting that increased capillary pumping makes the crystallization pattern more predictable. Simulations with smaller networks show more disparity between realizations of the same set of simulations (see Figure 4.13).

Since capillary pumping is very strong in this case, narrowing the pore size distri-

bution of the network does not play as strong of a role as in the case of fast drying (Figure 4.10). It can be seen that the network saturation at which the surface dries out is still around 70 percent and a very similar crystallization pattern is observed in this case according to Figure 4.11. The variance of the data is also similar to the previous case showing that the results can be reproduced easily.

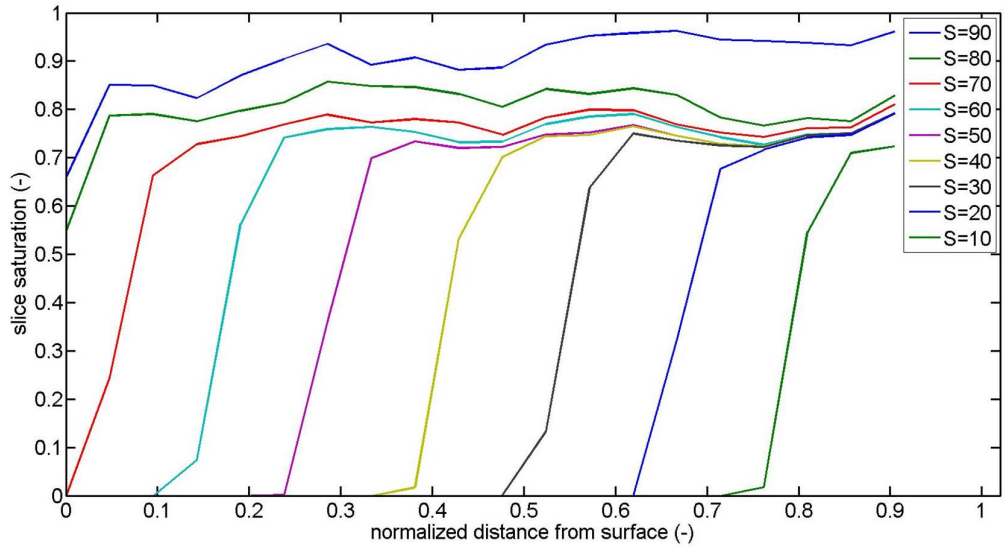

Figure 4.10: Saturation profile in the course of drying for case (b) with throat radii standard deviation of 10 nm.

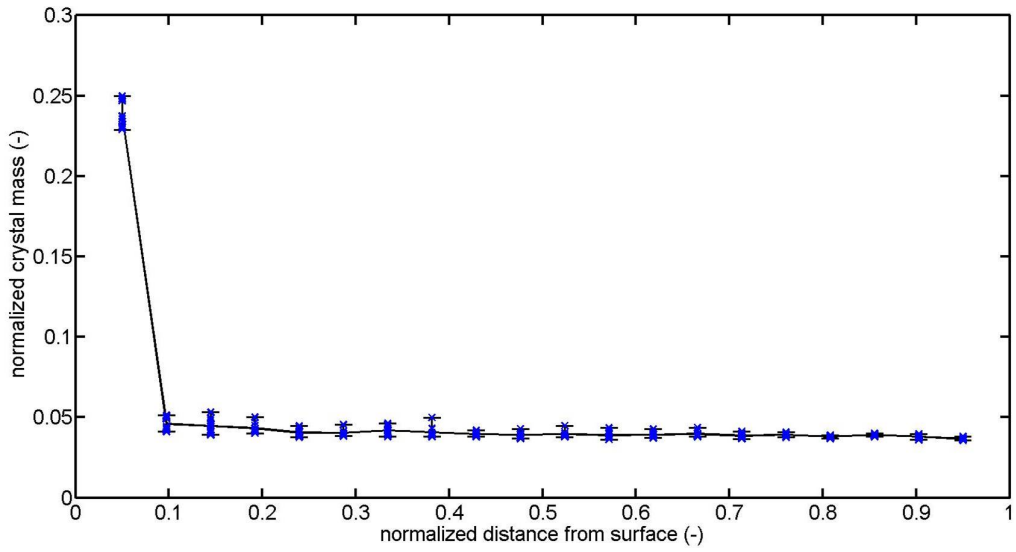

Figure 4.11: Salt mass profile at the end of drying for case (b) with throat radii standard deviation of 10 nm.

Before issuing the final verdict on the dominant effect of slow drying on capillary pumping, the standard deviation of throat radii is increased to 50 nm. The results look almost identical to the reference case, demonstrating the diminishing return of the influence of pore size distribution. It is concluded that since capillary pumping has already been at (or close to) its limit in the previous sets of simulations, for this case no meaningful deviation is observed by changing the width of the pore size distribution.

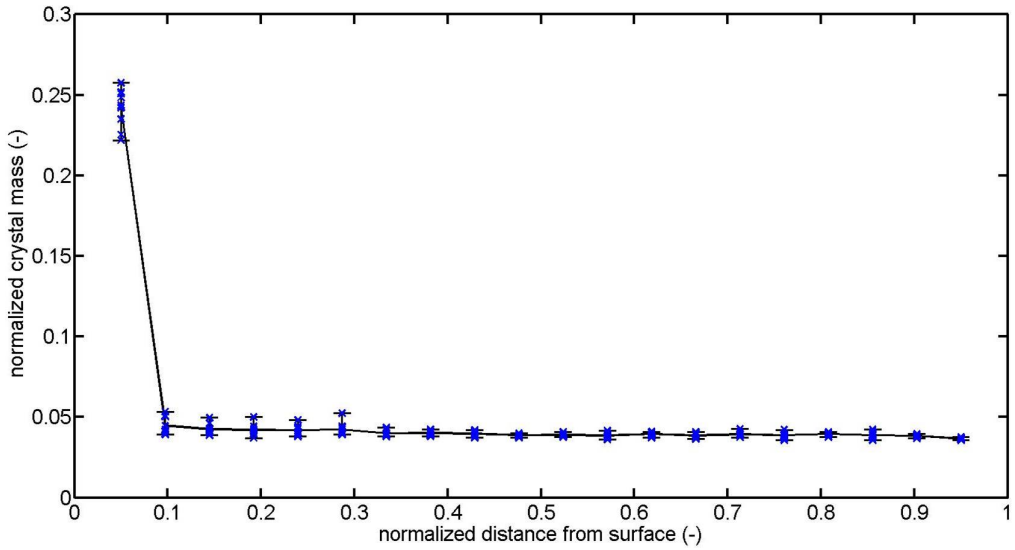

Figure 4.12: Salt mass profile at the end of drying for case (b) with throat radii standard deviation of 50 nm.

A very similar trend has also been reported by Börnhorst et al. [10]. The simulations and experiments conducted in that work for a similar PSD suggest that the mass fraction of the crystals found in the very top slice (or layers) are almost 5 times of those of the interior slices. Similarly, the uniform distribution of the salt crystals in the interior network is a testament to the accuracy of the model.

Similarly to case (a), simulations with smaller network show an increase in the variance of data for each set of simulations. For example, Figure 4.13 shows one simulation in which a near surface slice exhibits a significant accumulation of salt. This is an anomaly when compared to other realizations of the same simulation set data. This effect is a good example of randomness in network generation influencing simulation results, where on further repetition it is shown to be not representative. Such unique cases are far less likely to occur for simulations with larger networks.

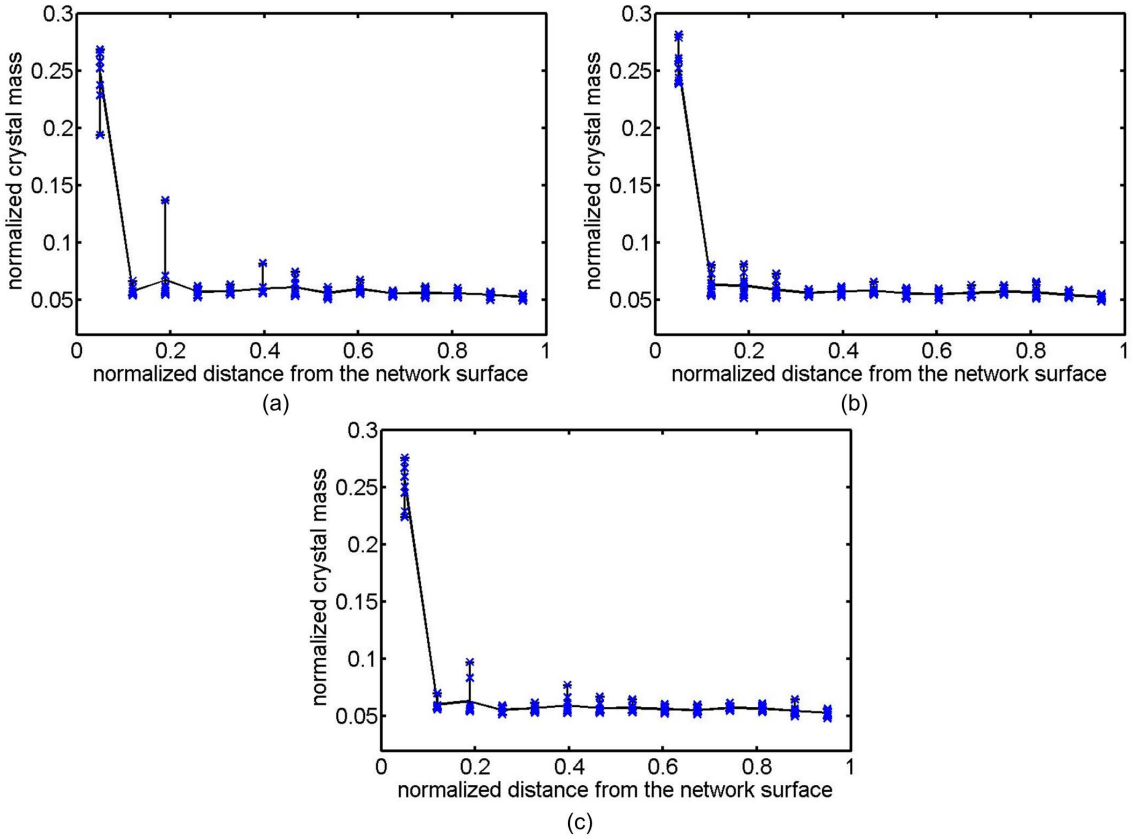

Figure 4.13: Salt mass profile at the end of drying for: (a) reference case, (b) narrow throat radii distribution, and (c) wide radii distribution for case (b) with smaller network size of $9 \times 9 \times 15$.

The results of the Monte-Carlo simulations of this section are summarized in Table 4.4. The quantitative representation of the results approves the conclusion drawn earlier that the change in pore size distribution has minimal effect in the case of slow drying. However, it is interesting to point out that salt is the most dispersed in the reference case which is counter-intuitive. However, it should be mentioned that the variance of the salt mass per throat is rather skewed due to significant accumulation of salt at the surface. Neglecting the surface throats reduces this variance by an order of magnitude pointing at the homogeneity of crystal mass within the interior throats. This example demonstrates that in pore network simulations, always sufficient information regarding the results should be presented to avoid false conclusions.

Table 4.4: Statistical presentation of salt distribution at the end of drying for case (b).

throat radii standard deviation	mean mass of salt (kg)	variance of mass of salt (kg)	mean mass of non-surface salt (kg)	variance of non-surface salt (kg)
narrow (10 nm)	7.54×10^{-17}	1.89×10^{-33}	5.98×10^{-17}	3.01×10^{-34}
reference (20 nm)	7.54×10^{-17}	2.07×10^{-33}	6.11×10^{-17}	3.43×10^{-34}
wide (50 nm)	7.54×10^{-17}	1.92×10^{-33}	6.13×10^{-17}	3.29×10^{-34}

4.1.3 *Slow drying and low initial concentration, case (c)*

The dominant effect of capillary pumping was demonstrated by a combination of saturation and salt profiles for case (b). The analysis regarding liquid transport by capillarity is also valid for case (c) as only the initial concentration is changed. Decreasing initial salt concentration is expected to counteract the advective effect of capillary pumping by increasing the diffusive potential. Not only reaching saturation concentration requires more evaporation of the liquid, but also diffusion is much stronger as a larger concentration gradient ($C^* - C_0$) is achieved. For this reason, salt profiles (Figure 4.14) show a much smoother decrease in crystal mass towards the interior of the network as the mass of crystals at the very top slice is not more than twice larger than in the slices at the bottom. This effect is clearly attributed to back-diffusion which delays crystallization at the surface and transports more salt to the network interior. The aforementioned ratio is between 5 to 6 times when looking at case (b) such as in Figure 4.9.

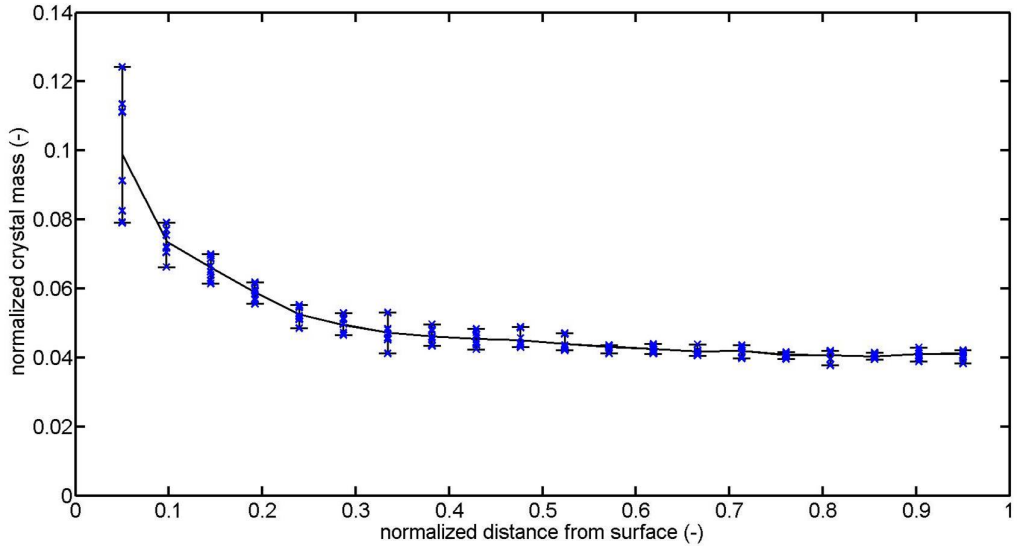

Figure 4.14: Salt mass profile at the end of drying for case (c) with throat radii standard deviation of 20 nm.

The results of simulations with different throat radii standard deviations are almost identical to the reference simulation as per negligible effect on capillarity which was demonstrated for case (b) that had the same drying conditions. These two cases are plotted next to each other in Figure 4.15. This similarity between all three sets of simulations indicates that the diffusion effect is not affected by variation of standard deviation in throat radii distribution.

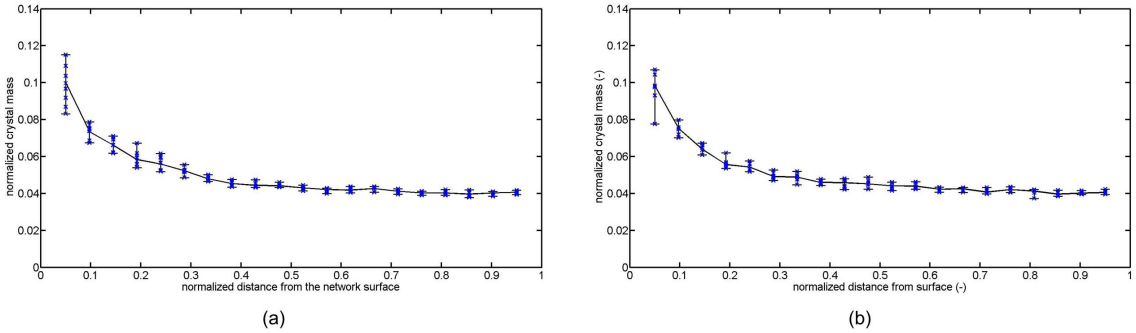

Figure 4.15: Salt mass profile at the end of drying for case (c) with throat radii standard deviation of: (a) 10 nm and (b) 50 nm.

In a similar fashion to case (b), the variance of the data is not affected significantly for variations of throat radii standard deviation. Said variance is highest in the surface slice. This is attributed to the moment the surface completely dries out which varies for each realization to a relatively small but in this case noticeable degree.

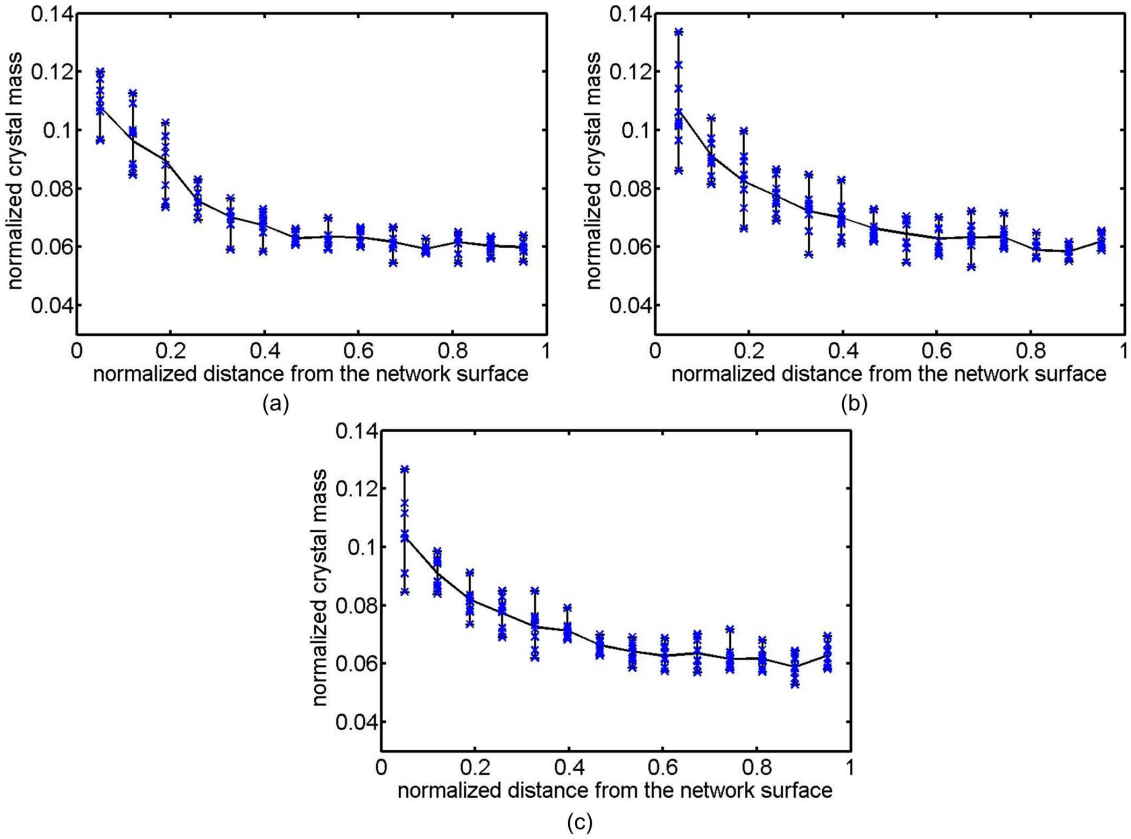

Figure 4.16: Salt mass profile at the end of drying for: (a) reference case, (b) narrow throat radii distribution, and (c) wide radii distribution for case (c) with smaller network size of $9 \times 9 \times 15$.

The effect of network size is very substantial for case (c) as shown in Figure 4.16. The effect of random network generation is very pronounced in this case as the disparity within each set of simulations goes up significantly. It can be argued that in this case, the increase in network size has significantly helped to move toward a representative size as only the network surface exhibits large variance among the results (see Figure 4.14).

Statistical representation of the results shows that the salt becomes more dispersed as the pore size distribution is widened. This implies that although capillary effect is very dominant, in this case, increasing the standard deviation of throat radii leads to more accumulation of salt in certain throats and depletion of others. This conclusion is based on the understanding that a wider distribution of throat radii leads to fewer throats that stay wet for a prolonged duration as the number of small (and large) throats is increased.

Table 4.5: Statistical presentation of salt distribution at the end of drying for case (c).

throat radii standard deviation	mean mass of salt (kg)	variance of mass of salt (kg)
narrow (10 nm)	1.68×10^{-17}	1.18×10^{-34}
reference (20 nm)	1.68×10^{-17}	1.18×10^{-34}
wide (50 nm)	1.68×10^{-17}	1.38×10^{-34}

Note: The similarity in the trend of salt profiles of Figures 4.6 and 4.14, attributed to case (a) and case (c) respectively, should not lead to a false conclusion on the controlling mechanisms. In the case of fast drying (Figure 4.6), the gradient is caused by a slight increase in capillary pumping but almost no back-diffusion causing some crystals to be formed at the surface. However, the surface does not stay wet for much longer duration which limits the total mass of crystals being formed there and therefore a transition to gradient profile is achieved. On the other hand in the case of low initial concentration coupled with slow drying (Figure 4.14), back-diffusion is responsible for transporting considerable amount of salt to the interior of the network and formation of a gradient in salt mass towards the interior.

The profiles of absolute salt mass per slice are presented in the appendix Section C.

4.2 Conclusion

In this chapter, the pore network model of Chapter 2 has been extended to 3D configuration. Additionally, the porosity of real porous materials can now be accounted for through utilizing bundles of capillaries instead of single throats which connect two neighboring nodes. The effects are noticeable when comparing the drying curve for the modified pore network model to the model with single throats (from Chapter 2). These improvements include an extended first drying period as well as a smooth transition during the falling rate period.

Pore network simulations have been carried out for three different conditions by varying drying rate and initial salt concentration. The effect of pore size distribution

has been investigated through varying standard deviation for throat radii distribution function. For each case, a set of Monte-Carlo type simulations with ten realizations has been carried out. The aim was to investigate the effect of randomness in network generation on the final crystal distribution. The effect of network size has also been investigated by choosing two sizes of $15 \times 15 \times 21$ (for large networks) and $9 \times 9 \times 15$ (for small networks).

Fast drying leads to viscous stabilization of the drying front where for the narrow pore size distribution a uniform salt distribution profile is achieved. The profiles evolve to a decreasing gradient towards the interior of the network. Increasing the standard deviation of throat radii causes capillary flow to be more pronounced. In these sets of simulations, the variance of the results between the ten realizations is moderate. This variance increases as the pore size distribution is widened implying that the stronger capillary regime intensifies the randomness of the results.

Slow drying leads to capillary fingering regime for a large portion of the simulations. The network surface stays wet until network saturation falls to values around 70 % at which point the liquid connectivity in the network is very weak. The change in the pore size distribution has negligible effect since the capillary flow of the liquid is at very high level and can neither be hindered nor can it be enhanced by the pore size distribution. For high initial concentration, ion transport to the network surface is handled by capillary flow of the liquid since back-diffusion is very limited. This leads to 25 % of the total mass of salt crystals being accumulated in the top slice. Crystals are uniformly distributed in the interior network which is due to the isolation of liquid and local crystallization. The variance of the data is very low and does not decrease significantly by enlargement of the network, indicating that the network size of $15 \times 15 \times 21$ may be considered representative for these results.

Decreasing the initial concentration of the salt combined with slow drying conditions makes the diffusion of the salt to become a relevant factor for the crystallization pattern. It is shown that a smooth decreasing gradient in the mass of salt is obtained toward inner slices. Back-diffusion of ions is responsible for transporting considerable amount of salt to the network depth as slow drying provides enough time for diffusion. The variance of the results is at a higher level compared to the previous case especially at the network surface, nonetheless, it is still considered low compared to the simulations with fast drying conditions. The increase in network size proves to be very useful in mitigating the effect of random generation in this case.

The variance of the data suggests that random distribution of throats is a predominant factor at high drying rates. This provides valuable insight into the process. It further suggests that the results of simulations with high drying rate should be an-

alyzed with more caution. It is expected that the results will become more uniform as pore networks are enlarged.

Chapter 5

Summary and future work

5.1 Conclusion

In this thesis, ion transport and crystallization as a result of drying of salt solution in porous media has been studied. To this goal, the crystallization algorithm has been developed and incorporated into existing pore network models. The model is isothermal and all colligative properties of solutions are neglected. Moreover, ion adsorption at the pore wall and alteration of pore size distribution, due to crystallization, have not been accounted for. Few modifications have proved necessary in this endeavor by investigating the pore network simulation results. The modifications vary from changes in the network geometry to new approaches to the algorithms to handle various phenomena. Finally, in order to minimize the effects of random network generation, Monte-Carlo type simulations have been carried out using 3D networks. The findings of these simulations are recapitulated in this chapter.

The first pore network model focuses on drying of initially saturated materials based on the model of Metzger et al. [66]. The void space of a porous medium is approximated by a network of cylindrical throats which are connected via nodes that have no volume. Therefore, the throats hold the liquid volume and nodes are used for computational purposes. Liquid motion in the network is modeled by capillary induced viscous flow whereas vapor transfer follows Stefan's law. Ion transport in the throats is modeled by a 1D advection-diffusion equation assuming plug flow of liquid. Initially, uniform ion concentration for the throats has been assumed to discretize said equation. However, the node-throats geometry of the network made an unorthodox solution necessary, which needs to be validated. Thus, a test problem has been developed where a capillary which is connected to a reservoir is exposed to evaporation. As a reference, this problem was solved by the finite volume method

and the concentration profile was compared to the ones obtained from pore network simulation. The results are identical indicating the validity of the solution. Moreover, the numerical accuracy of the model has been assessed by mass dispersion in a long tube. This problem can be solved analytically where a function is acquired over time and space for salt concentration. The comparison points at significant overestimation of diffusion. It has been demonstrated that the discrepancy between the results is directly correlated with the values of the local Pe number. A remedy to this issue is to decrease the length of the computational elements. However, since the problem involves only ion transport calculations and not the liquid motion, throats are adaptively divided (according to the current local Pe number) to virtual computational elements only concerning ion transport calculations. The computational grid can be refined or coarsened following an algorithm according to the current Pe number.

Simulations with 2D pore networks have been carried out by the drying-crystallization model. Combination of capillary pumping, diffusion, and drying rate dictate crystallization pattern in the network. Slow drying leads to the formation of significant portion of efflorescence during the first drying period. Crystals are distributed uniformly in the interior of the network as isolated clusters of liquid dry individually. Raising the drying rate causes the first drying period to end very rapidly. During this stage, capillary flow is very limited and salt crystallizes locally at the top slice. This period is followed by a drastic drop in evaporation rate due to the addition of a significant vapor diffusion resistance by empty throats of the first layer. As a result, capillarity dominates the process leading to transport of significant amount of crystals to regions beneath the surface. As liquid flow pattern, in the second drying period, is similar to that of the slow drying case, crystallization pattern in the network depth looks very much alike for both cases. Simulations with the same conditions are repeated for lower initial concentration to enhance the diffusion effect. In short, diffusion leads to more homogeneous crystallization especially in the case of slow drying. The 2D simulations, despite being limited in their application, have helped a great deal in understanding the underlying mechanisms regarding drying induced crystallization in porous media.

The previous model does not include the wetting stage of the process. This stage is especially important if the samples are not filled by submerging into a solution basin for sufficient time which may lead to a fully saturated porous medium. It is a crucial part of processes such as spray agglomeration where droplets of binder solution are sprayed over porous particles or agglomerates. This process has previously been studied by the pore network model of Rahimi et al. [87]. The algorithm of that model is considerably improved by introducing volume at throat junctions in

the form of spherical pores. Comparison of the results of these two models reveals clear advantages of this modification. The comparison is conducted by decoupling the capillary pressure induced by pores from their respective radii. Some of the improvements are as follows: tackling of unsustainable events, more stable liquid flow, ease of construction of networks with bimodal pore size distribution, etc. Later on, the crystallization algorithm has been implemented into this model with an assumption of perfect mixing in the pores. A second comparison between the crystallization pattern predicted by this model and the drying-crystallization model of Chapter 2 has been carried out. The results have qualitative similarities although in exceptional cases clear disparities are observed. More importantly, computational efficiencies of the two aforementioned models are considerably far apart, with the drying-crystallization model having a clear advantage. On that note, it is borderline impractical to perform 3D simulations with the wetting-drying-crystallization model, let alone in Monte-Carlo setting.

It is well understood that 2D simulations miss important effects when describing crystallization process during drying of real porous samples. The areas which pose the most important limiting factors are as follows: liquid connectivity, network size, and network porosity. The first two limitations are addressed by extending the model to 3D configuration and including periodic boundary conditions, thus increasing pore coordination number and eliminating the effect of network sides. Moreover, network porosity has been increased by introducing sections of uniform porosity comprised of bundles of capillaries instead of single throats. The direct effect of this modification is shown by comparing drying curves for respective conditions. The new modified model does not suffer from an overestimated drop in the transition stage to the falling rate period while exhibiting an extended first drying period.

It is known that the random generation of network has a direct effect on the results quantitatively. It is believed that, given sufficiently large networks, the results may converge. Therefore, in order to assess the extent of these disparities, a set of Monte-Carlo simulations have been carried out where network generation varies. The results are then averaged while keeping the variance among all simulations in mind. Three different conditions for simulations are considered and for each case throat radii standard deviation is varied. Fast drying with high initial concentration produces the most unpredictable results with a moderately high standard deviation. Although a stabilizing drying front is achieved, the limited capillary pumping still produces high variation between salt profiles at the end of the simulations. In this case, an increase in the network size has noticeable effect on the consistency of the results, but an even further enlargement might prove useful. Mass of salt crystals per slice shows a gradient over distance from the network surface, as the pore size distri-

bution widens. The simulation conditions of case (a) produce the most homogeneous crystallization patterns especially for narrower pore size distribution (Figure 4.5). As drying rate is lowered capillarity dominates the results. Capillary fingering regime is responsible for the transport of significant amounts of salt to the network surface (one quarter of the whole salt mass). The remaining amount of salt is distributed very homogeneously as sub-florescence. The variance of the data is very low in this case, pointing at the predictability of these simulations. Simulations with smaller network sizes still produce consistent results between each realization. Variation of pore size distribution has minimal effect on the results as the drying rate is too low to produce any viscous effects in the network. In order to study the effect of diffusion, two factors should be considered: sufficient time and increased diffusion potential. These requirements can be provided by slow drying rate and decreasing initial salt concentration. According to the results, back-diffusion has a significant effect on salt profile at the end of simulations. Instead of a sharp drop in the mass of salt from the first to the second slice, a smooth transition is observed. The variance of the data is slightly higher compared to the high initial concentration case, especially at the network surface. Once again, simulations with smaller networks show a noticeable increase in the variance of the results within each set of simulations. An increase in the network size proves essential in this case to achieve consistency in the results.

These simulation results show very good qualitative agreement with the experimental results of Börnhorst et al. [10] obtained from microtomography. Moreover, the effects that were not captured in 2D simulations, such as receding drying front and diffusion effect, are clearly presented in the 3D pore network simulations.

5.2 Outlook

Even though promising results are obtained from 3D pore network simulations, the models can still be improved in a number of aspects. These improvements are divided into three different categories: tackling simplifying assumptions, the inclusion of new physical effects, and model's algorithm.

In developing the model, some important assumptions are made that may potentially alter the results of the model significantly. Firstly, the colligative properties of the salt solution need to be taken into account. As an example, it is shown in the literature (such as in [73]) that saturation vapor pressure has a nonlinear correlation with salt concentration. This might have a measurable effect on the drying rate. Also, the physical volume of salt crystals has been neglected in this model. The direct effect of this change involves alteration of pore size distribution and potentially clogging

of throats. This addition could prove detrimental to drying, especially in cases of massive efflorescence, and needs to be investigated thoroughly.

There are some effects which, given the circumstances, are capable of dominating ion transport and crystallization. For example, the drying process could be non-isothermal on many occasions. It is also commonly known that solubility of most salts is highly dependent on temperature. Thus, tracking variation of temperature and the corresponding effects in the system may be crucial to correctly simulate the process. Additionally, some effects can become decisive regarding pore geometry and pore size distribution. Two examples may be mentioned here: ion adsorption at pore walls and film effect. As throat or pore radii drop below certain values (depending on the salt, temperature, etc) ion adsorption may become detrimental to ion transport in the network. On the other hand, film effect in the system depends highly on the pore geometry. For example, cubic throats can have significant film induced effect where the liquid connection is maintained through the so-called "corner films" formed at the wedges. In the presence of film effect, drying curve and crystallization are changed drastically. Some of the expected consequences are an extended first drying period and the growth of crystals in seemingly dry regions. Finally, the kinetics of crystallization has been completely neglected, which is generally an important factor. Nevertheless, it is not completely obvious whether it might affect the results as significantly as the aforementioned points.

The algorithms presented in this work may be improved in various manners. One of the areas in which important gains can be achieved is the calculation scheme for salt time-steps. One of the suggestions is a procedure by which according to the local concentration salt time-step is defined (also known as von Neumann recipe). In this way, stability criterion is always maintained (not only for Pe number close to unity) as well as eliminating unnecessary divisions of global time-step. However, we are not completely optimistic on whether by implementing this recipe less computational cost is required since it is significantly dependent on network size and process conditions. Therefore, as a last resort transitioning to an implicit solution scheme to solve the ion transport equation should be considered.

Bibliography

[1] N. Alleborn and H. Raszillier. Spreading and sorption of a droplet on a porous substrate. *Chemical Engineering Science*, 59(10):2071 – 2088, 2004.

[2] L. André, Y. Peysson, and M. Azaroual. Well injectivity during CO_2 storage operations in deep saline aquifers, Part 2: Numerical simulations of drying, salt deposit mechanisms and role of capillary forces. *International Journal of Greenhouse Gas Control*, 22:301 – 312, 2014.

[3] M. Aubertin and R. Chapuis. *Predicting the coefficient of permeability of soils using the Kozeny-Carman equation.* Rapport technique. École polytechnique de Montréal, 2003.

[4] N. Bajcinca and S. Hofman. Optimal control for batch crystallization with size-dependent growth kinetics. In *Proceedings of the 2011 American Control Conference*, pages 2558 – 2565, June 2011.

[5] J. Bear. *Dynamics of fluids in porous media.* American Elsevier Publishing Company, Dover, 1972.

[6] N. Belgacem, M. Prat, and J. Pauchet. Coupled continuum and condensation evaporation pore network model of the cathode in polymer-electrolyte fuel cell. *International Journal of Hydrogen Energy*, 42(12), 8150 – 8165, 2017.

[7] S. Blacher, A. Lonard, B. Heinrichs, N. Tcherkassova, F. Ferauche, M. Crine, P. Marchot, E. Loukine, and J.-P. Pirard. Image analysis of x-ray microtomograms of $PdAg/SiO_2$ xerogel catalysts supported on Al_2O_3 foams. *Colloids and Surfaces A: Physicochemical and Engineering Aspects*, 241(13):201 – 206, 2004.

[8] T. D. Blake, A. Clarke, J. De Coninck, and M. J. de Ruijter. Contact angle relaxation during droplet spreading: Comparison between molecular kinetic theory and molecular dynamics. *Langmuir*, 13(7):2164 – 2166, 1997.

[9] M. J. Blunt. Flow in porous media: Pore-network models and multiphase flow. *Current Opinion in Colloid and Interface Science*, 6(3):197 – 207, 2001.

[10] M. Börnhorst, P. Walzel, A. Rahimi, A. Kharaghani, E. Tsotsas, N. Nestle, A. Besser, F. Kleine Jäger, and T. Metzger. Influence of pore structure and impregnation-drying conditions on the solid distribution in porous support materials. *Drying Technology*, 34(16):1964 – 1978, 2016.

[11] J. Carmeliet, F. Descamps, and G. Houvenaghel. A multiscale network model for simulating moisture transfer properties of porous media. *Transport in Porous Media*, 35(1):67 – 88, 1999.

[12] S. Chan and K. Ng. Geometrical characteristics of the pore space in a random packing of equal spheres. *Powder Technology*, 54(2):147 – 155, 1988.

[13] A. Clarke, T. D. Blake, K. Carruthers, and A. Woodward. Spreading and imbibition of liquid droplets on porous surfaces. *Langmuir*, 18(8):2980 – 2984, 2002.

[14] O. Coussy. Deformation and stress from in-pore drying-induced crystallization of salt. *Journal of the Mechanics and Physics of Solids*, 54(8):1517 – 1547, 2006.

[15] H. Darcy. *Les fontaines publiques de la ville de Dijon*. Victor Dalmont, Paris, France, 1856.

[16] S. H. Davis and L. M. Hocking. Spreading and imbibition of viscous liquid on a porous base, Part 1. *Physics of Fluids*, 11(1):48 – 57, 1999.

[17] S. H. Davis and L. M. Hocking. Spreading and imbibition of viscous liquid on a porous base, Part 2. *Physics of Fluids*, 12(7):1646 – 1655, 2000.

[18] M. A. Day. The no-slip condition of fluid dynamics. *Erkenntnis*, 33(3):285 – 296, 1990.

[19] M. Denesuk, G. Smith, B. Zelinski, N. Kreidl, and D. Uhlmann. Capillary penetration of liquid droplets into porous materials. *Journal of Colloid and Interface Science*, 158(1):114 – 120, 1993.

[20] T. G. D'Onofrio, H. K. Navaz, B. Markicevic, B. A. Mantooth, and K. B. Sumpter. Experimental and numerical study of spread and sorption of VX sessile droplets into medium grain-size sand. *Langmuir*, 26(5):3317 – 3322, 2010.

[21] H. Eloukabi, N. Sghaier, S. B. Nasrallah, and M. Prat. Experimental study of the effect of sodium chloride on drying of porous media: The crusty-patchy efflorescence transition. *International Journal of Heat and Mass Transfer*, 56(12):80 – 93, 2013.

[22] R. M. Espinosa-Marzal and G. W. Scherer. Mechanisms of damage by salt. *Geological Society, London, Special Publications*, 331(1):61 – 77, 2010.

[23] I. Fatt. The network model of porous media. *AIME Petroleum Transactions*, 207:144 – 159, 1956.

[24] A. Fick. Ueber Diffusion. *Annalen der Physik*, 170(1):59 – 86, 1855.

[25] H. B. Fischer, E. J. List, R. C. Koh, J. Imberger, and N. H. Brooks. Chapter 4 - shear flow dispersion. *Mixing in Inland and Coastal Waters*, pages 80 – 103. Academic Press, San Diego, 1979.

[26] D. S. Freitas and M. Prat. Pore network simulation of evaporation of a binary liquid from a capillary porous medium. *Transport in Porous Media*, 40(1):1 – 25, 2000.

[27] N. Fries and M. Dreyer. The transition from inertial to viscous flow in capillary rise. *Journal of Colloid and Interface Science*, 327(1):125 – 128, 2008.

[28] M. Giulietti, M. M. Seckler, S. Derenzo, M. I. Ré, and E. Cekinski. Industrial crystallization and precipitation from solutions: State of the technique. *Brazilian Journal of Chemical Engineering*, 18:423 – 440, 2001.

[29] T. D. Gonalves, L. Pel, and J. D. Rodrigues. Influence of paints on drying and salt distribution processes in porous building materials. *Construction and Building Materials*, 23(5):1751 – 1759, 2009.

[30] L. Guglielmini, A. Gontcharov, A. J. Aldykiewicz Jr., and H. A. Stone. Drying of salt solutions in porous materials: Intermediate-time dynamics and efflorescence. *Physics of Fluids*, 20(7):077101, 2008.

[31] S. Gupta, K. Terheiden, L. Pel, and A. Sawdy. Influence of ferrocyanide inhibitors on the transport and crystallization processes of sodium chloride in porous building materials. *Crystal Growth & Design*, 12(8):3888 – 3898, 2012.

[32] J. C. H. Derluyn, P. Moonen. Modelling of moisture and salt transport incorporating salt. In *International RILEM Symposium on Concrete Modelling*, pages 535–542. RILEM Publications SARL, 2008.

[33] A. Hamraoui and T. Nylander. Analytical approach for the Lucas-Washburn equation. *Journal of Colloid and Interface Science*, 250(2):415 – 421, 2002.

[34] K. P. Hapgood, J. D. Litster, S. R. Biggs, and T. Howes. Drop penetration into porous powder beds. *Journal of Colloid and Interface Science*, 253(2):353 – 366, 2002.

[35] S. M. Hassanizadeh and T. Leijnse. On the modeling of brine transport in porous media. *Water Resources Research*, 24(3):321 – 330, 1988.

[36] E. R. Herbert, P. Boon, A. J. Burgin, S. C. Neubauer, R. B. Franklin, M. Ardn, K. N. Hopfensperger, L. P. M. Lamers, and P. Gell. A global perspective on wetland salinization: Ecological consequences of a growing threat to freshwater wetlands. *Ecosphere*, 6(10):1 – 43, 2015.

[37] H. P. Huinink, L. Pel, M. Michels, and M. Prat. Drying processes in the presence of temperature gradients: Pore-scale modelling. *The European Physical Journal E*, 9(1):487 – 498, 2002.

[38] J. J. Valenza and G. W. Scherer. A review of salt scaling, Part 1: Phenomenology. *Cement and Concrete Research*, 37(7):1007 – 1021, 2007.

[39] J. J. Valenza and G. W. Scherer. A review of salt scaling, Part 2: Mechanisms. *Cement and Concrete Research*, 37(7):1022 – 1034, 2007.

[40] M. A. Ioannidis and I. Chatzis. Network modelling of pore structure and transport properties of porous media. *Chemical Engineering Science*, 48(5):951 – 972, 1993.

[41] A. Irawan. *Isothermal drying of pore networks: Influence of pore structure on drying kinetics*. PhD thesis, Otto von Guericke University Magdeburg, 2006.

[42] N. S. J. Desarnaud, D. Bonn. The pressure induced by salt crystallization in confinement. *Scientific Reports*, 6(30856), 2016.

[43] G. R. Jerauld, J. C. Hatfield, L. E. Scriven, and H. T. Davis. Percolation and conduction on Voronoi and triangular networks: A case study in topological disorder. *Journal of Physics C: Solid State Physics*, 17(9):1519, 1984.

[44] N. C. Reis Jr., R. F. Griffiths, and J. M. Santos. Numerical simulation of the impact of liquid droplets on porous surfaces. *Journal of Computational Physics*, 198(2):747 – 770, 2004.

[45] A. Kharaghani. *Irregular pore networks and mechanical effects during drying of porous media*. PhD thesis, Otto von Guericke University Magdeburg, 2010.

[46] A. Kharaghani, T. Metzger, and E. Tsotsas. A proposal for discrete modeling of mechanical effects during drying, combining pore networks with DEM. *AIChE Journal*, 57(4):872 – 885, 2011.

[47] A. Kharaghani, T. Metzger, and E. Tsotsas. An irregular pore network model for convective drying and resulting damage of particle aggregates. *Chemical Engineering Science*, 75:267 – 278, 2012.

[48] M. Knudsen. Die Gesetze der Molekularströmung und der inneren Reibungsströmung der Gase durch Röhren. *Annalen der Physik*, 333(1):75 – 130, 1909.

[49] M. Komiyama. Design and preparation of impregnated catalysts. *Catalysis Reviews*, 27(2):341 – 372, 1985.

[50] M. Koniorczyk, D. Gawin, P. Konca, and D. Bednarska. Modeling damage of building materials induced by sodium sulphate crystallization. *Bauphysik*, 38(6):366 – 371, 2016.

[51] N. S. Lani, N. Ngadi, N. Y. Yahya, and R. A. Rahman. Synthesis, characterization and performance of silica impregnated calcium oxide as heterogeneous catalyst in biodiesel production. *Journal of Cleaner Production*, 146:116 – 124, 2017.

[52] J. B. Laurindo and M. Prat. Numerical and experimental network study of evaporation in capillary porous media: Phase distributions. *Chemical Engineering Science*, 51(23):5171 – 5185, 1996.

[53] J. B. Laurindo and M. Prat. Numerical and experimental network study of evaporation in capillary porous media: Drying rates. *Chemical Engineering Science*, 53(12):2257 – 2269, 1998.

[54] K. H. Le, A. Kharaghani, C. Kirsch, and E. Tsotsas. Discrete pore network modeling of superheated steam drying. *Drying Technology*, 35(13): 1584 – 1601, 2017.

[55] K. H. Le, A. Kharaghani, C. Kirsch, and E. Tsotsas. Pore network simulations of heat and mass transfer inside an unsaturated capillary porous wick in the dry-out regime. *Transport in Porous Media*, 114(3):623 – 648, 2016.

[56] D. Lockington and J.-Y. Parlange. A new equation for macroscopic description of capillary rise in porous media. *Journal of Colloid and Interface Science*, 278(2):404 – 409, 2004.

[57] L. A. Rijniers, L. Pel, H. P. Huinink, and K. Kopinga. Salt crystallization as damage mechanism in porous building materials: A nuclear magnetic resonance study. *Magnetic Resonance Imaging*, 23:273 – 276, 2005.

[58] R. Lucas. Ueber das Zeitgesetz des kapillaren Aufstiegs von Flüssigkeiten. *Kolloid-Zeitschrift*, 23(1):15 – 22, 1918.

[59] M. Mantle, N. Reis, R. Griffiths, and L. Gladden. MRI studies of the evaporation of a single liquid droplet from porous surfaces. *Magnetic Resonance Imaging*, 21(34):293 – 297, 2003.

[60] B. Markicevic, T. G. D'Onofrio, and H. K. Navaz. On spread extent of sessile droplet into porous medium: Numerical solution and comparisons with experiments. *Physics of Fluids*, 22(1):012103, 2010.

[61] B. Markicevic, H. Li, Y. Sikorski, A. Zand, M. Sanders, and H. K. Navaz. Infiltration time and imprint shape of a sessile droplet imbibing porous medium. *Journal of Colloid and Interface Science*, 336(2):698 – 706, 2009.

[62] B. Markicevic and H. K. Navaz. Numerical solution of wetting fluid spread into porous media. *International Journal of Numerical Methods for Heat & Fluid Flow*, 19(3/4):521 – 534, 2009.

[63] B. Markicevic and H. K. Navaz. Primary and secondary infiltration of wetting liquid sessile droplet into porous medium. *Transport in Porous Media*, 85(3):953 – 974, 2010.

[64] W. McCabe, J. Smith, and P. Harriott. *Unit operations of chemical engineering*. McGraw-Hill, New York, USA, 2005.

[65] T. Metzger, A. Irawan, and E. Tsotsas. Influence of pore structure on drying kinetics: A pore network study. *AIChE Journal*, 53(12):3029 – 3041, 2007.

[66] T. Metzger, A. Irawan, and E. Tsotsas. Isothermal drying of pore networks: Influence of friction for different pore structures. *Drying Technology*, 25(1):49 – 57, 2007.

[67] T. Metzger and E. Tsotsas. Influence of pore size distribution on drying kinetics: A simple capillary model. *Drying Technology*, 23(9-11):1797 – 1809, 2005.

[68] T. Metzger and E. Tsotsas. Viscous stabilization of drying front: Three-dimensional pore network simulations. *Chemical Engineering Research and Design*, 86(7):739 – 744, 2008.

[69] U. Nachshon, A. Ireson, G. van der Kamp, S. R. Davies, and H. S. Wheater. Impacts of climate variability on wetland salinization in the North American prairies. *Hydrology and Earth System Sciences*, 18(4):1251–1263, 2014.

[70] U. Nachshon, E. Shahraeeni, D. Or, M. I. Dragila, and N. Weisbrod. Infrared thermography of evaporative fluxes and dynamics of salt deposition on heterogeneous porous surfaces. *Water Resources Research*, 47(12), W12519, 2011.

[71] U. Nachshon, N. Weisbrod, M. I. Dragila, and A. Grader. Combined evaporation and salt precipitation in homogeneous and heterogeneous porous media. *Water Resources Research*, 47(3), W03513, 2011.

[72] H. K. Navaz, B. Markicevic, A. R. Zand, Y. Sikorski, E. Chan, M. Sanders, and T. G. D'Onofrio. Sessile droplet spread into porous substrates: Determination of capillary pressure using a continuum approach. *Journal of Colloid and Interface Science*, 325(2):440 – 446, 2008.

[73] M. Norouzi Rad and N. Shokri. Nonlinear effects of salt concentrations on evaporation from porous media. *Geophysical Research Letters*, 39(4), L04403, 2012.

[74] M. Norouzi Rad, N. Shokri, and M. Sahimi. Pore-scale dynamics of salt precipitation in drying porous media. *Phys. Rev. E*, 88:032404, 2013.

[75] S. C. Nowicki, H. T. Davis, and L. E. Scriven. Microscopic determination of transport parameters in drying porous media. *Drying Technology*, 10(4):925 – 946, 1992.

[76] L. Pel, H. P. Huinink, and K. Kopinga. Salt transport and crystallization in porous building materials. *Magnetic Resonance Imaging*, 21(34):317 – 320, 2003.

[77] J. Petković, H. P. Huinink, L. Pel, K. Kopinga, and R. P. J. van Hees. Salt transport in plaster/substrate layers. *Materials and Structures*, 40(5):475 – 490, 2006.

[78] Y. Peysson, L. André, and M. Azaroual. Well injectivity during CO_2 storage operations in deep saline aquifers, Part 1: Experimental investigation of

drying effects, salt precipitation and capillary forces. *International Journal of Greenhouse Gas Control*, 22:291 – 300, 2014.

[79] F. Plourde and M. Prat. Pore network simulations of drying of capillary porous media: Influence of thermal gradients. *International Journal of Heat and Mass Transfer*, 46(7):1293 – 1307, 2003.

[80] L. L. Popovich, D. L. Feke, and I. Manas-Zloczower. Influence of physical and interfacial characteristics on the wetting and spreading of fluids on powders. *Powder Technology*, 104(1):68 – 74, 1999.

[81] M. Prat. Percolation model of drying under isothermal conditions in porous media. *International Journal of Multiphase Flow*, 19(4):691 – 704, 1993.

[82] M. Prat. Isothermal drying on non-hygroscopic capillary-porous materials as an invasion percolation process. *International Journal of Multiphase Flow*, 21(5):875 – 892, 1995.

[83] M. Prat. On the influence of pore shape, contact angle and film flows on drying of capillary porous media. *International Journal of Heat and Mass Transfer*, 50(78):1455 – 1468, 2007.

[84] M. Prat and F. Bouleux. Drying of capillary porous media with a stabilized front in two dimensions. *Phys. Rev. E*, 60:5647 – 5656, 1999.

[85] K. Pruess and N. Müller. Formation dry-out from CO_2 injection into saline aquifers, Part 1: Effects of solids precipitation and their mitigation. *Water Resources Research*, 45(3), W03402, 2009.

[86] A. Rahimi, A. Kharaghani, T. Metzger, and E. Tsotsas. Pore network model for drying of salt solutions: Solute migration and crystallization. In *Proceedings of Nordic Baltic Drying Conference. Gdansk, Poland*, 2015.

[87] A. Rahimi, T. Metzger, A. Kharaghani, and E. Tsotsas. Interaction of droplets with porous structures: Pore network simulation of wetting and drying. *Drying Technology*, 34(9):1129 – 1140, 2016.

[88] L. A. Rijniers, H. P. Huinink, L. Pel, and K. Kopinga. Experimental evidence of crystallization pressure inside porous media. *Phys. Rev. Lett.*, 94:075503, 2005.

[89] C. Rodriguez-Navarro, E. Doehne, and E. Sebastian. Influencing crystallization damage in porous materials through the use of surfactants: Experimental

results using sodium dodecyl sulfate and cetyldimethylbenzylammonium chloride. *Langmuir*, 16(3):947 – 954, 2000.

[90] F. A. SanMartin, J. B. Laurindo, and L. A. Segura. Pore-scale simulation of drying of a porous media saturated with a sucrose solution. *Drying Technology*, 29(8):873 – 887, 2011.

[91] G. W. Scherer. Crystallization in pores. *Cement and Concrete Research*, 29(8):1347 – 1358, 1999.

[92] G. W. Scherer. Reply to the discussion by S. Chatterji of the paper: "Crystallization in pores". *Cement and Concrete Research*, 30(4):673 – 675, 2000.

[93] G. W. Scherer. Stress from crystallization of salt. *Cement and Concrete Research*, 34(9):1613 – 1624, 2004.

[94] N. Shahidzadeh-Bonn, J. Desarnaud, F. Bertrand, X. Chateau, and D. Bonn. Damage in porous media due to salt crystallization. *Phys. Rev. E*, 81:066110, 2010.

[95] D. Smith, G. W. Scherer, and J. Anderson. Shrinkage during drying of silica gel. *Journal of Non-Crystalline Solids*, 188(3):191 – 206, 1995.

[96] H. C. Van Ness, J. M. Smith, and M. Abbott. *Introduction to chemical engineering thermodynamics*. McGraw-Hill, New York, USA, 2004.

[97] V. M. Starov, S. Kostvintsev, V. Sobolev, M. Velarde, and S. Zhdanov. Spreading of liquid drops over dry porous layers: Complete wetting case. *Journal of Colloid and Interface Science*, 252(2):397 – 408, 2002.

[98] V. M. Starov. Surfactant solutions and porous substrates: Spreading and imbibition. *Advances in Colloid and Interface Science*, 111(12):3 – 27, 2004.

[99] A. N. Stranges. A history of the Fischer-Tropsch synthesis in Germany. In B. Davis and M. Occelli, editors, *Fischer-Tropsch synthesis, catalyst and catalysis*, volume 163 of *Studies in Surface Science and Catalysis*, pages 1 – 27. Elsevier, 2007.

[100] B. Straubhaar, J. Pauchet, and M. Prat. Pore network modelling of condensation in gas diffusion layers of proton exchange membrane fuel cells. *International Journal of Heat and Mass Transfer*, 102:891 – 901, 2016.

[101] Y. Sun, A. Kharaghani, T. Metzger, J. Müller, and E. Tsotsas. Micro-model experiments and pore network simulations of liquid imbibition in porous media. *Chemical Engineering Science*, 150:41 – 53, 2016.

[102] Y. Sun, A. Kharaghani, T. Metzger, J. Müller, and E. Tsotsas. Lotion distribution in wet wipes investigated by pore network simulation and x-ray micro tomography. *Transport in Porous Media*, 107(2):449 – 468, 2015.

[103] V. K. Surasani, T. Metzger, and E. Tsotsas. Consideration of heat transfer in pore network modelling of convective drying. *International Journal of Heat and Mass Transfer*, 51(910):2506 – 2518, 2008.

[104] V. K. Surasani, T. Metzger, and E. Tsotsas. A non-isothermal pore network drying model with gravity effect. *Transport in Porous Media*, 80(3):431 – 439, 2009.

[105] V. K. Surasani, T. Metzger, and E. Tsotsas. Drying simulations of various 3D pore structures by a non-isothermal pore network model. *Drying Technology*, 28(5):615 – 623, 2010.

[106] S. P. Sutera and R. Skalak. The history of Poiseuille's law. *Annual Review of Fluid Mechanics*, 25:1 – 20, 1993.

[107] N. Tavare. *Industrial crystallization: Process simulation, analysis and design.* Plenum press, New York, USA, 1995.

[108] S. Veran-Tissoires, M. Marcoux, and M. Prat. Discrete salt crystallization at the surface of a porous medium. *Phys. Rev. Lett.*, 108:054502, 2012.

[109] S. Veran-Tissoires and M. Prat. Evaporation of a sodium chloride solution from a saturated porous medium with efflorescence formation. *Journal of Fluid Mechanics*, 749:701 – 749, 2014.

[110] N. Vorhauer, T. Metzger, and E. Tsotsas. On the influence of temperature gradients on drying of pore networks. In *Proceedings of European Drying Conference. Palma, Spain.* Citeseer, 2011.

[111] E. W. Washburn. The dynamics of capillary flow. *Phys. Rev.*, 17:273 – 283, 1921.

[112] R. Wu, A. Kharaghani, and E. Tsotsas. Capillary valve effect during slow drying of porous media. *International Journal of Heat and Mass Transfer*, 94:81 – 86, 2016.

[113] R. Wu, A. Kharaghani, and E. Tsotsas. Two-phase flow with capillary valve effect in porous media. *Chemical Engineering Science*, 139:241 – 248, 2016.

[114] A. G. Yiotis, A. G. Boudouvis, A. K. Stubos, I. N. Tsimpanogiannis, and Y. C. Yortsos. Effect of liquid films on the drying of porous media. *AIChE Journal*, 50(11):2721 – 2737, 2004.

[115] A. G. Yiotis, A. K. Stubos, A. G. Boudouvis, and Y. C. Yortsos. A 2D pore-network model of the drying of single-component liquids in porous media. *Advances in Water Resources*, 24(34):439 – 460, 2001.

[116] A. G. Yiotis, A. K. Stubos, A. G. Boudouvis, I. N. Tsimpanogiannis, and Y. C. Yortsos. Pore-network modeling of isothermal drying in porous media. *Transport in Porous Media*, 58(1):63 – 86, 2005.

[117] T. Young. An essay on the cohesion of fluids. *Philosophical Transactions of the Royal Society of London*, 95:65 – 87, 1805.

[118] M. Zdražil. Preparation of alumina supported molybdena catalysts by new slurry impregnation method: MoO_3/Al_2O_3 sulfide hydrodesulfurization catalyst. *Catalysis Letters*, 27(3):337 – 344, 1994.

Appendix A

Simulation parameters

Table A.1: Physical properties of the materials used in simulations.

liquid dynamic viscosity ($Pa \cdot s$)	1×10^{-3}
liquid surface tension (Nm^{-1})	7.27×10^{-2}
Vapor-gas binary diffusion coefficient ($m^2 s^{-1}$)	2.5×10^{-5}
liquid molar mass ($kgkmol^{-1}$)	18.02
liquid density (kgm^{-3})	998.2
saturation concentration of salt (kgm^{-3})	359.3
ion-liquid binary diffusion coefficient ($m^2 s^{-1}$)	1×10^{-9}

Table A.2: Drying conditions and initial salt concentration for different cases.

parameter	high	low
boundary layer thickness (μm)	1	100
drying air temperature ($^{\circ}C$)	80	25
saturation vapor pressure (Pa)	47000	2339
initial salt concentration (kgm^{-3})	323.3	71.8

Table A.3: Pore network structure information for simulations of Chapter 2 and Section 3.2.3.

number of nodes in vertical direction	10
number of nodes in horizontal direction	10
total number of vertical throats	90
total number of horizontal throats	81
mean throat radius	100 nm
throat radii standard deviation	10 nm
throat length	1 μm
porosity	0.14

Table A.4: Pore network structure information for simulations of Chapter 3 (section 3.3).

number of nodes in vertical direction	20
number of nodes in horizontal direction	12
total number of vertical throats	180
total number of horizontal throats	209
mean throat radii	200 nm
throat radii standard deviation	20 nm
mean macro-throat radius	400 nm
macro-throat radii standard deviation	40 nm
throat length	1 μm
porosity of monomodal network	0.2
porosity of bimodal network	0.26
droplet volume (m^3)	1.5×10^{-17}

Table A.5: Pore network structure information for simulations of Chapter 4.

number of nodes in vertical direction	21
number of nodes in each lateral direction	15
total umber of vertical throats	4725
total umber of horizontal throats	9000
mean throat radii	200 nm
reference throat radii standard deviation	20 nm
narrow throat radii standard deviation	10 nm
wide throat radii standard deviation	50 nm
throat length	1 μm
porosity of network	0.7

Appendix B

Simulation results for Chapter 3

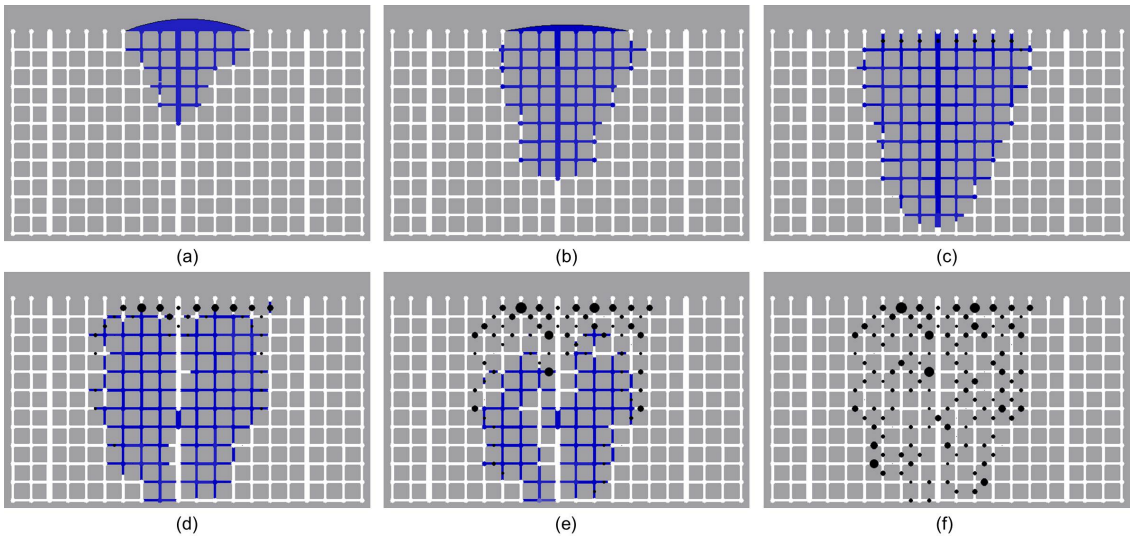

Figure B.1: Phase distribution for fast drying and high initial salt concentration produced by wetting-drying-crystallization algorithm. Network comprises of microporous regions separated by vertical macro-channels. Results are shown for network saturations of: (a) 10 %, (b) 20 %, (c) 30 % in wetting stage and (d) 25 %, (e) 15 %, (f) 0 % in drying stage.

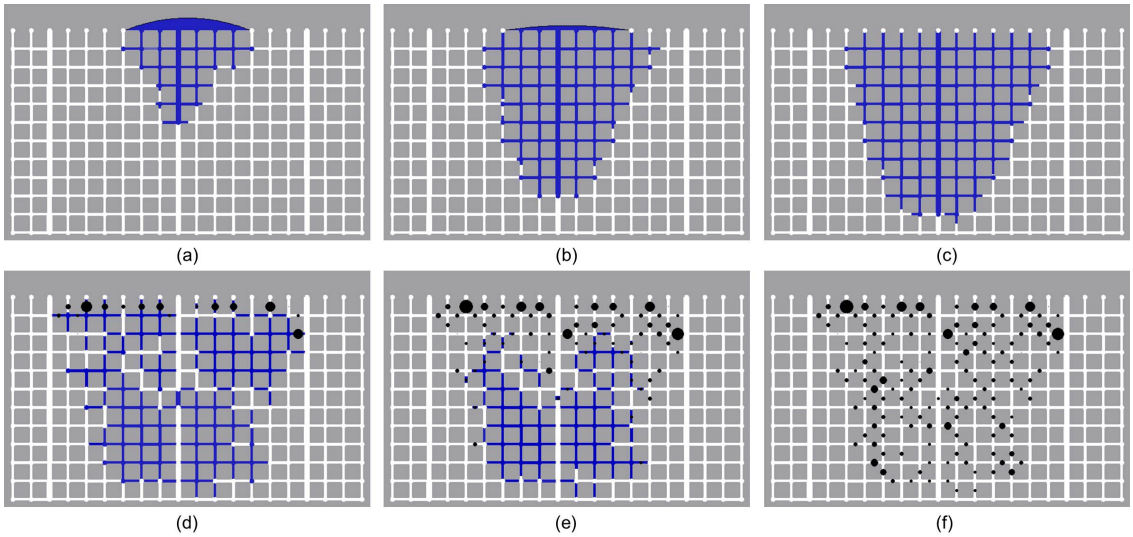

Figure B.2: Phase distribution for slow drying and high initial salt concentration produced by wetting-drying-crystallization algorithm. Network comprises of microporous regions separated by vertical macro-channels. Results are shown for network saturations of: (a) 10 %, (b) 25 %, (c) 30 % in wetting stage and (d) 25 %, (e) 15 %, (f) 0 % in drying stage.

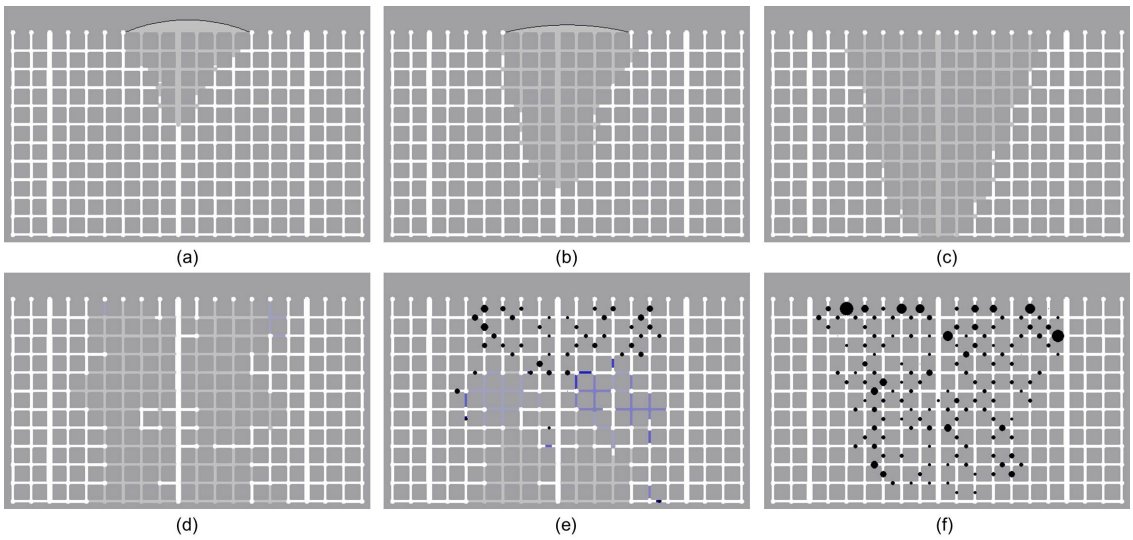

Figure B.3: Phase distribution for slow drying and low initial salt concentration produced by wetting-drying-crystallization algorithm. Network comprises of microporous regions separated by vertical macro-channels. Results are shown for network saturations of: (a) 10 %, (b) 20 %, (c) 33 % in wetting stage and (d) 25 %, (e) 15 %, (f) 0 % in drying stage.

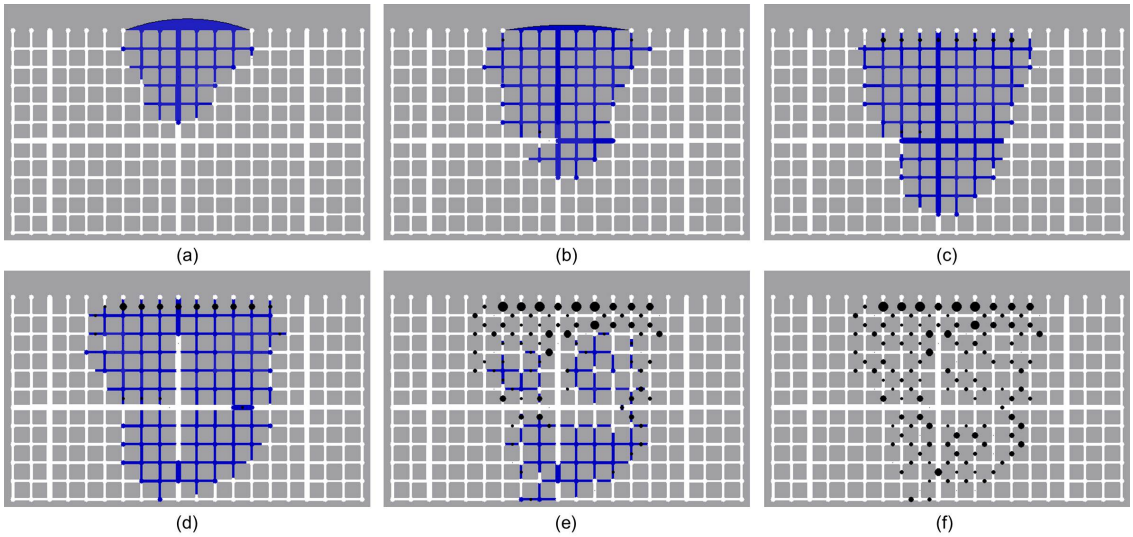

Figure B.4: Phase distribution for fast drying and high initial salt concentration produced by wetting-drying-crystallization algorithm. Network comprises of microporous regions separated by vertical and horizontal macro-channels. Results are shown for network saturations of: (a) 10 %, (b) 20 %, (c) 27 % in wetting stage and (d) 25 %, (e) 10 %, (f) 0 % in drying stage.

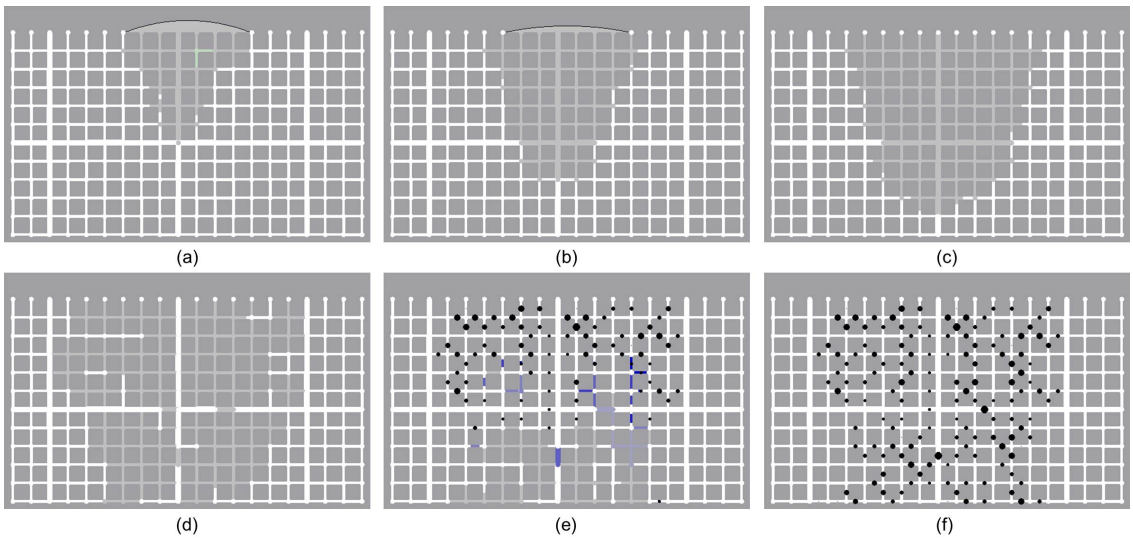

Figure B.5: Phase distribution for slow drying and low initial salt concentration produced by wetting-drying-crystallization algorithm. Network comprises of microporous regions separated by vertical and horizontal macro-channels. Results are shown for network saturations of: (a) 10 %, (b) 20 %, (c) 30 % in wetting stage and (d) 25 %, (e) 10 %, (f) 0 % in drying stage.

Appendix C

Simulation results for Chapter 4

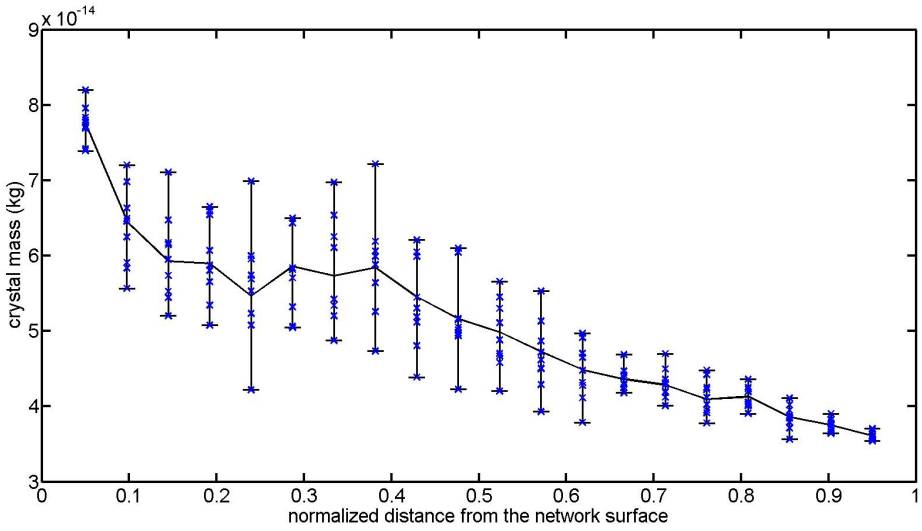

Figure C.1: Salt mass profile at the end of drying for case (a) with throat radii standard deviation of 10 nm.

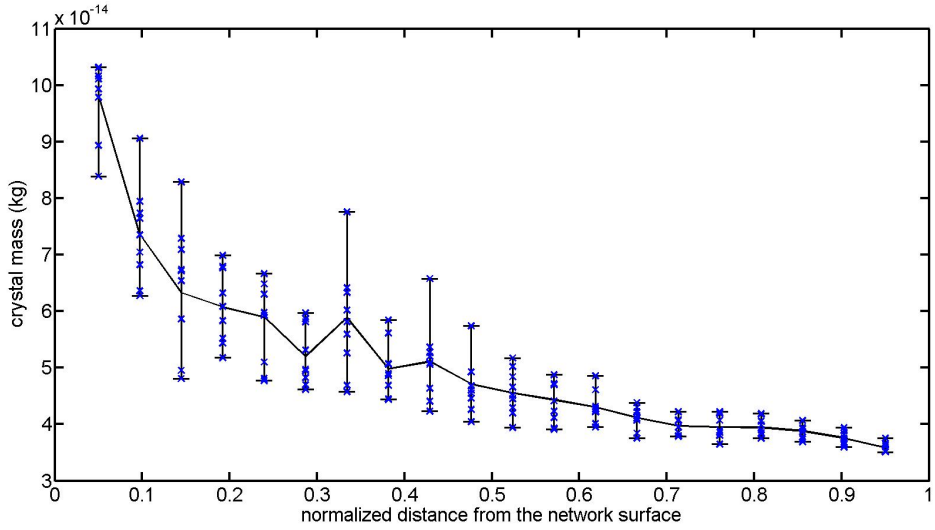

Figure C.2: Salt mass profile at the end of drying for case (a) with throat radii standard deviation of 20 nm.

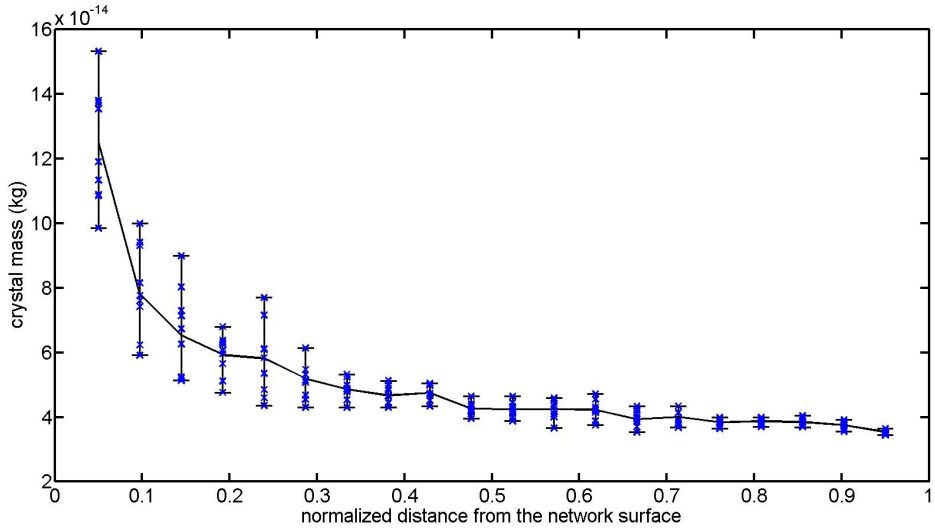

Figure C.3: Salt mass profile at the end of drying for case (a) with throat radii standard deviation of 50 nm.

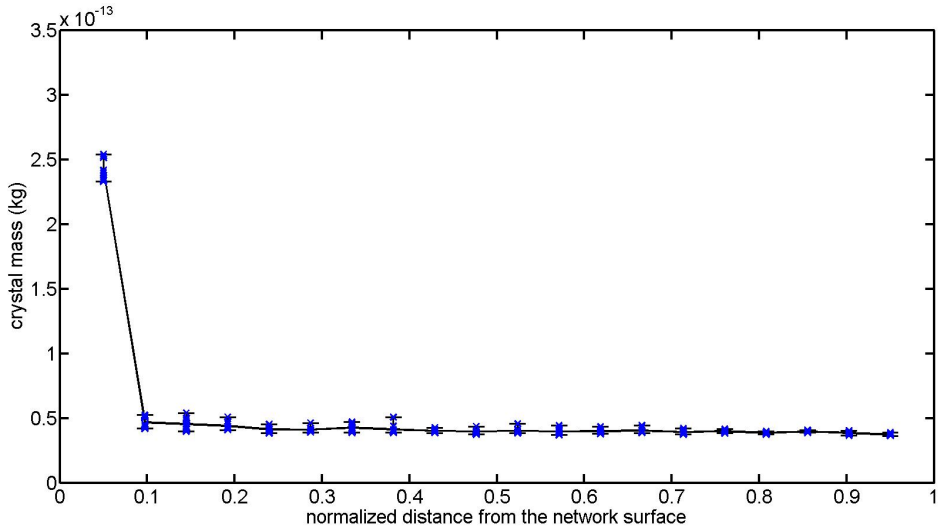

Figure C.4: Salt mass profile at the end of drying for case (b) with throat radii standard deviation of 10 nm.

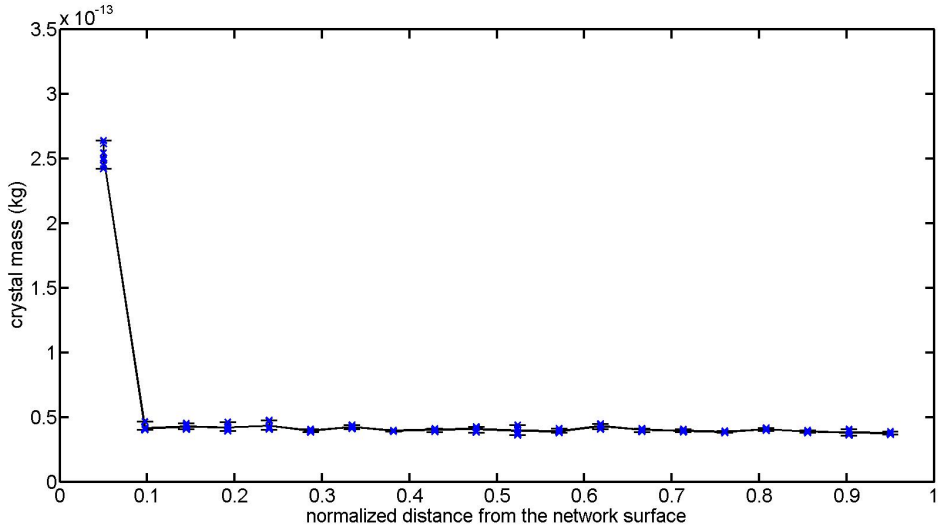

Figure C.5: Salt mass profile at the end of drying for case (b) with throat radii standard deviation of 20 nm.

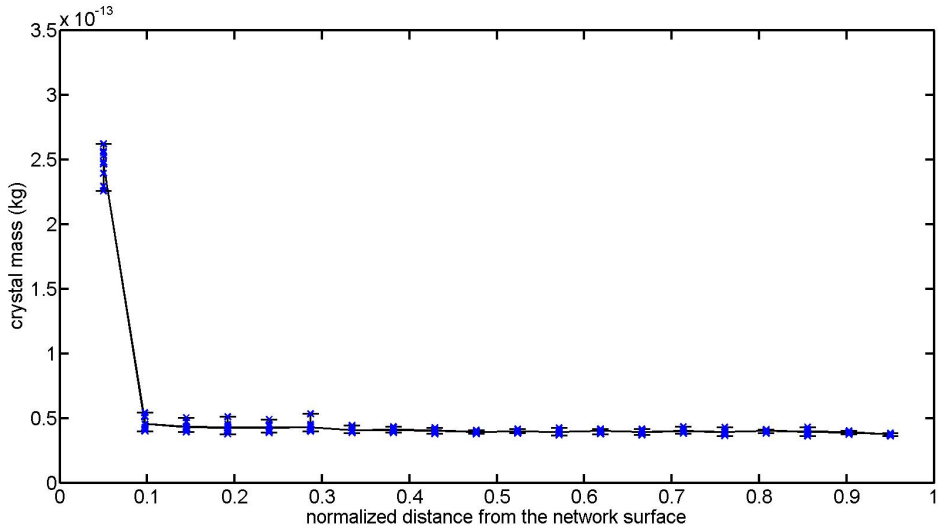

Figure C.6: Salt mass profile at the end of drying for case (b) with throat radii standard deviation of 50 nm.

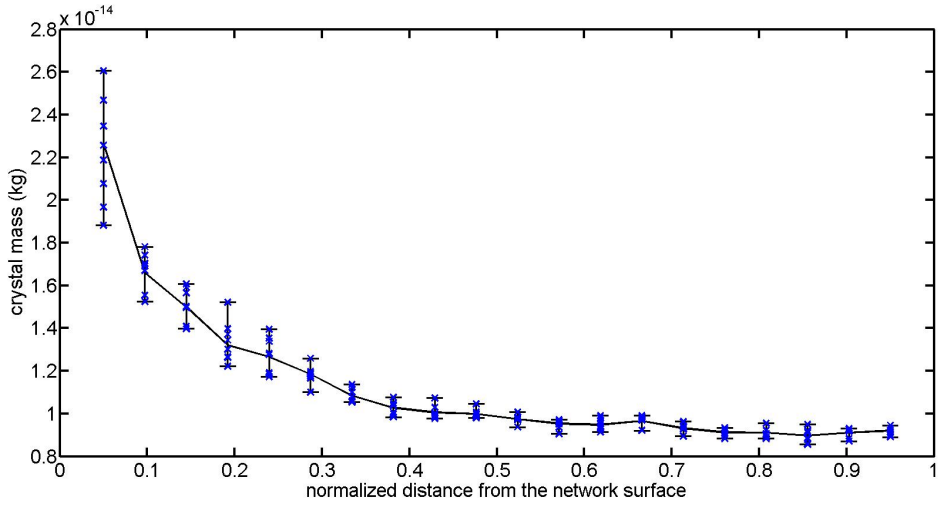

Figure C.7: Salt mass profile at the end of drying for case (c) with throat radii standard deviation of 10 nm.

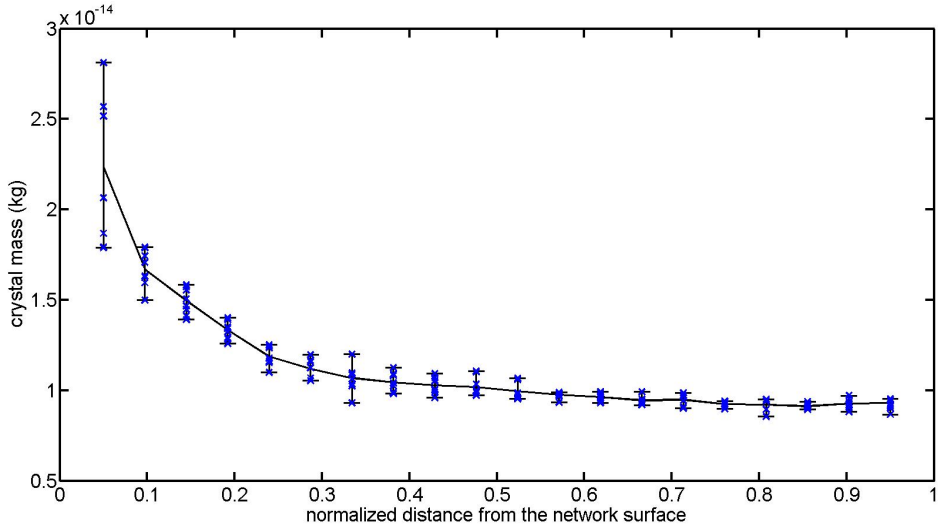

Figure C.8: Salt mass profile at the end of drying for case (c) with throat radii standard deviation of 20 nm.

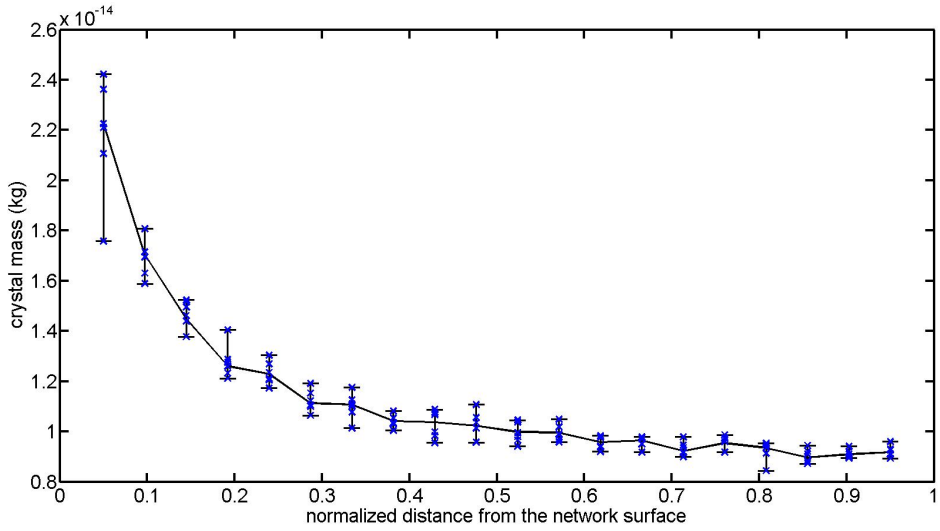

Figure C.9: Salt mass profile at the end of drying for case (c) with throat radii standard deviation of 50 nm.

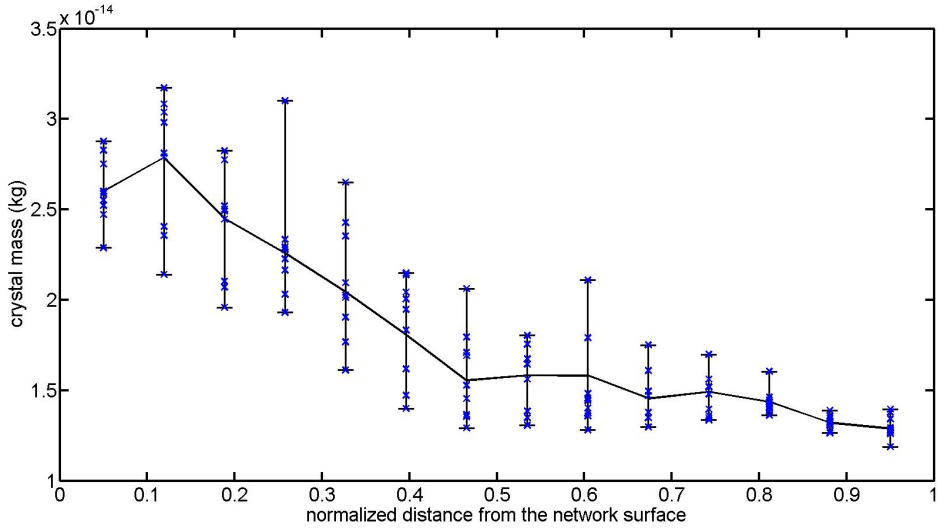

Figure C.10: Salt mass profile at the end of drying for case (a) with throat radii standard deviation of 10 nm for the small network of size $9 \times 9 \times 15$.

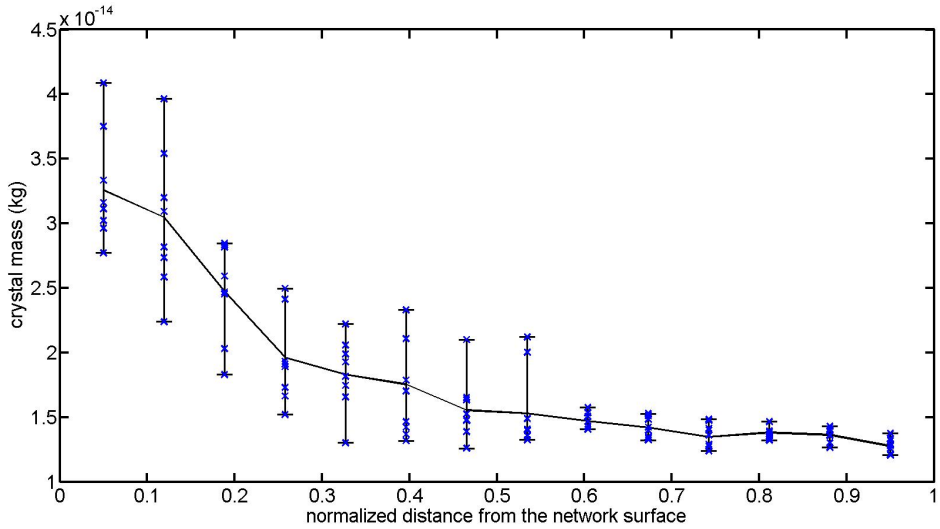

Figure C.11: Salt mass profile at the end of drying for case (a) with throat radii standard deviation of 20 nm for the small network of size $9 \times 9 \times 15$.

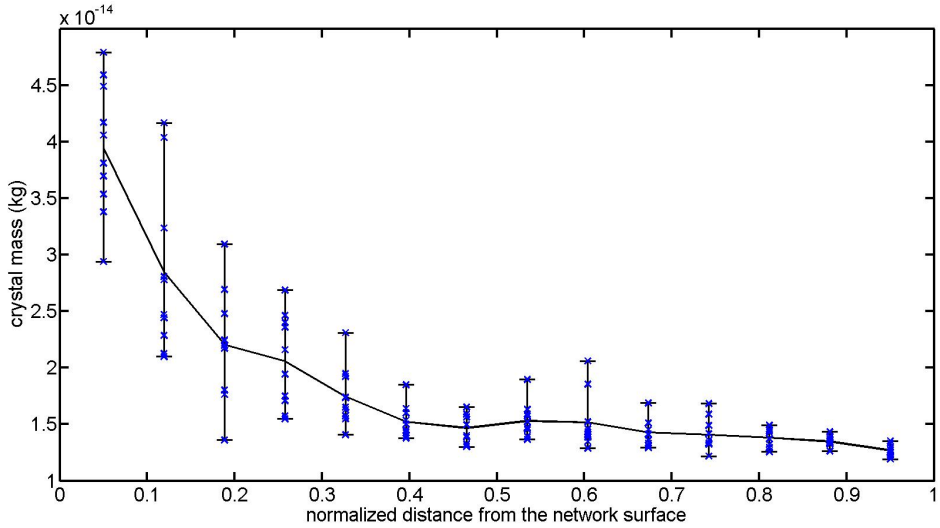

Figure C.12: Salt mass profile at the end of drying for case (a) with throat radii standard deviation of 50 nm for the small network of size $9 \times 9 \times 15$.

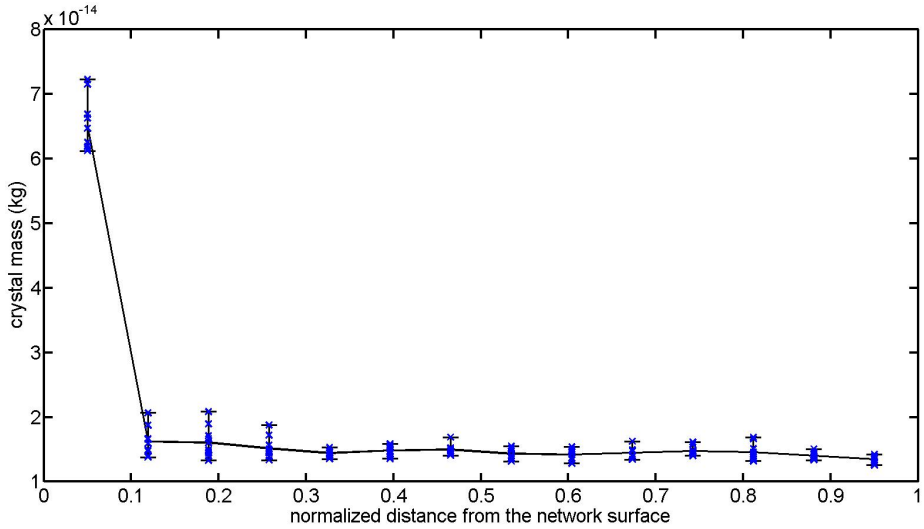

Figure C.13: Salt mass profile at the end of drying for case (b) with throat radii standard deviation of 10 nm for the small network of size $9 \times 9 \times 15$.

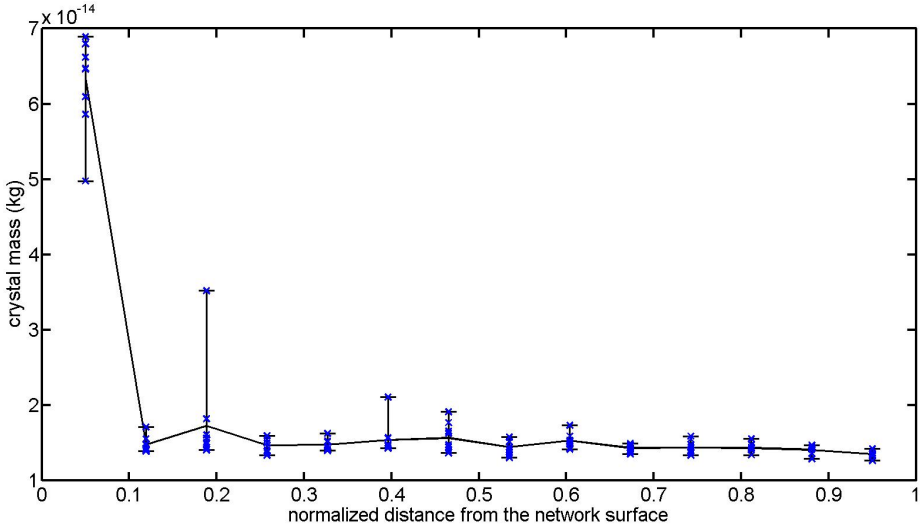

Figure C.14: Salt mass profile at the end of drying for case (b) with throat radii standard deviation of 20 nm for the small network of size $9 \times 9 \times 15$.

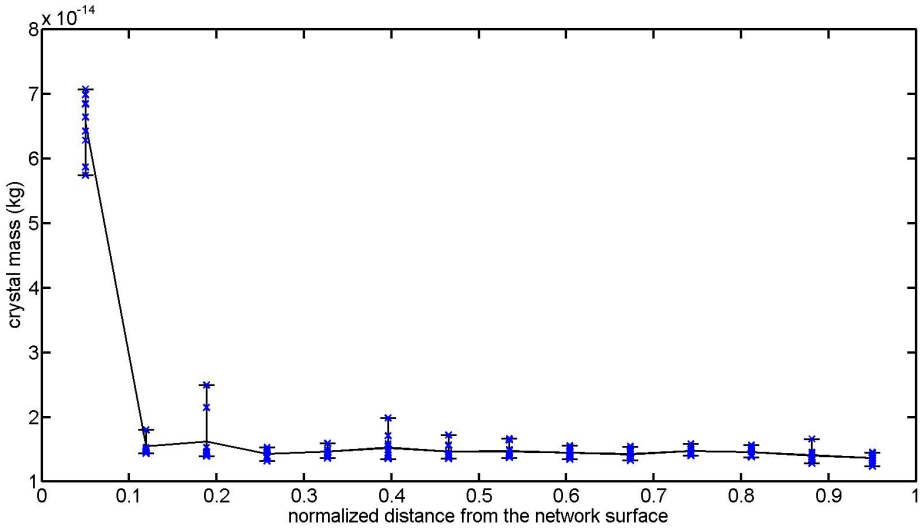

Figure C.15: Salt mass profile at the end of drying for case (b) with throat radii standard deviation of 50 nm for the small network of size $9 \times 9 \times 15$.

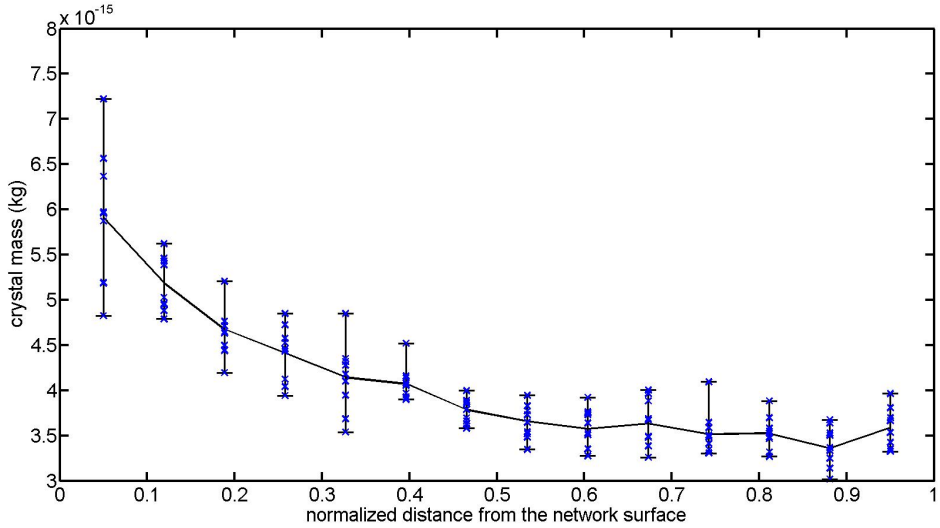

Figure C.16: Salt mass profile at the end of drying for case (c) with throat radii standard deviation of 10 nmfor the small network of size $9 \times 9 \times 15$.

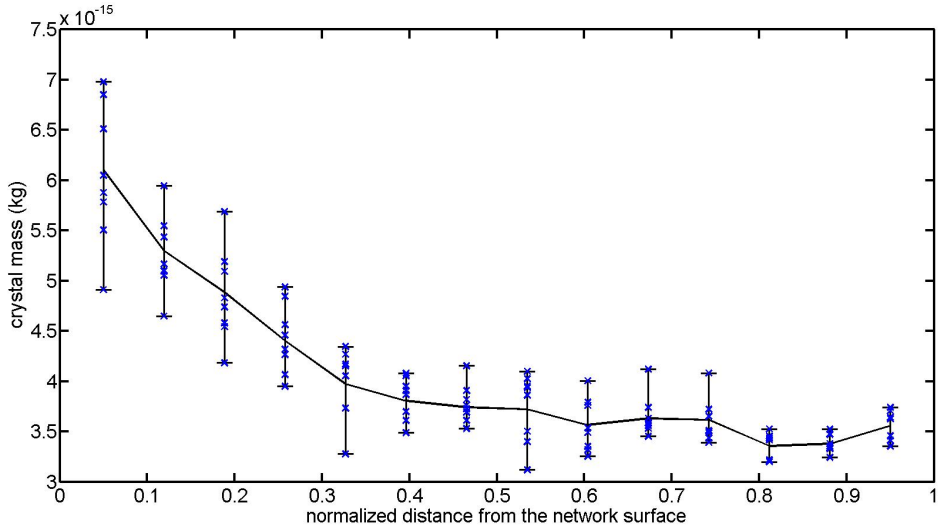

Figure C.17: Salt mass profile at the end of drying for case (c) with throat radii standard deviation of 20 nm for the small network of size $9 \times 9 \times 15$.

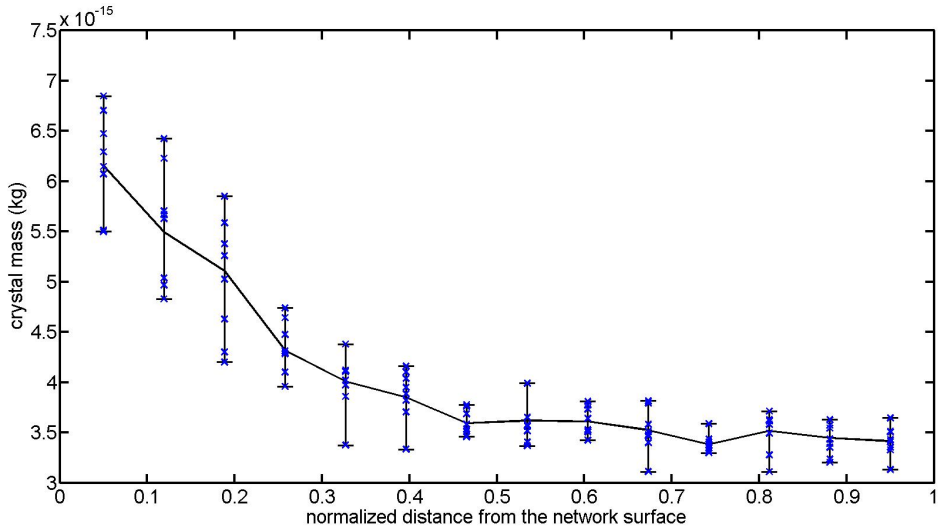

Figure C.18: Salt mass profile at the end of drying for case (c) with throat radii standard deviation of 50 nm for the small network of size $9 \times 9 \times 15$.

Appendix D

Electronic appendix

Codes and results of this thesis will be documented in an electronic appendix, available at the chair of Thermal Process Engineering, Otto Von Guericke University Magdeburg. In the following a list of contents of this electronic appendix is given.

MATLAB Codes and Result Files

- Test Problems
  - FVM_PNM comparison (Section 2.2.4)
    file to run: ViscousDryingSquareNetwork.m
  - Mass dispersion_PNM comarison(Section 2.2.5)
    file to run: PN.m
- Ion Transport and Crystallization
  - 2D Drying_Crystallization (Section 2.2.6)
    file to run: ViscousDryingSquareNetwork.m
  - Wetting_Drying_Crystallization_PoresSpheres (Sections 3.2.3 and 3.3)
    file to run: BasicAlgorithm.m
  - 3D Drying_Crystallization (Section 4.1.1)
    file to run: ViscousDryingCubicNetwork.m
- Comparison of Wetting-Drying models
  - Wetting_Drying_NodesNoVolume (Sections 3.2.3)
    file to run: BasicAlgorithm.m
  - Wetting_Drying_PoreSpheres (Sections 3.2.3)
    file to run: BasicAlgorithm.m
  - Wetting_Drying_PoreSpheres (DecoupledPressureAtPores) (Sections 3.2.3)
    file to run: BasicAlgorithm.m

    - Wetting_Drying_PoreSpheres (Standard) (Sections 3.2.3)
      file to run: BasicAlgorithm.m
- Monte-Carlo Simulations
    - Simulation Results (Sections 4.1.1)
      file to run: FigureGenerator.m

Student works

The following student works were conducted within the framework of this thesis:

1. Ahmad Gohari, *Two-dimensional Discrete Model to Shrinkage during Drying.* Master thesis, Chair of Thermal Process Engineering, Otto von Guericke University Magdeburg, Magdeburg, August 2014.

2. Xiaoci Hu, *Incorporation of pore-node volume into wetting-drying pore network model.* Master thesis, Chair of Thermal Process Engineering, Otto von Guericke University Magdeburg, Magdeburg, September 2015.

Publications and presentations

Own publications and presentations related to this thesis in national and international journals and conferences are listed the following.

Publications in national and international journals, and in conference proceedings

1. A. Rahimi, T. Metzger, A. Kharaghani, and E. Tsotsas. *Interaction of droplets with porous structures*, Drying Technology, 34(9):1129 – 1140, 2016.

2. M. Börnhorst, P. Walzel, A. Rahimi, A. Kharaghani, E. Tsotsas, N. Nestle, A. Besser, F. Kleine Jäger, and T. Metzger. *Influence of pore size distribution and impregnation-drying conditions on the solid distribution in porous support materials*, Drying Technology, 34(16):1964 – 1978, 2016.

3. A. Rahimi, A. Kharaghani, T. Metzger, and E. Tsotsas. *Discrete pore network modeling of solute transport and solid formation during drying of a capillary porous structure*, To be submitted.

4. A. Rahimi, A. Kharaghani, T. Metzger, and E. Tsotsas. *Pore network modeling of impregnation and drying of porous media: infiltration of a salt solution droplet*, To be prepared.

5. A. Rahimi, A. Kharaghani, T. Metzger, and E. Tsotsas. *Drying of a shrinking porous medium saturated with a solution: a pore network study*, 6th European Drying Conference, Torino, Italy, Jul. 2019.

6. A. Rahimi, T. Metzger, A. Kharaghani, and E. Tsotsas. *Discrete modeling of ion transport and crystallization in layered porous media during drying*, 21st International Drying Symposium, Valencia, Spain, Sep. 2018.

7. A. Rahimi, T. Metzger, A. Kharaghani, and E. Tsotsas. *Solute transport and crystallization in a combined wetting-drying pore network model*, 20th International Drying Symposium, Gifu, Japan, Aug. 2016.

8. A. Rahimi, A. Kharaghani, T. Metzger, and E. Tsotsas. *Pore network simulation of salt crystallization in drying porous media*, 5th European Drying Conference, Budapest, Hungary, Oct. 2015.

9. A. Rahimi, A. Kharaghani, T. Metzger, and E. Tsotsas. *Pore network model for drying of salt solutions: solute migration and crystallization*, 1st Nordic Baltic Drying Conference, Gdansk, Poland, Jun. 2015.

10. A. Rahimi, T. Metzger, A. Kharaghani, and E. Tsotsas. *Droplet migration into porous substrate simulated by mono-modal and bimodal networks*, 19th International Drying Symposium, Lyon, France, Aug. 2014.

11. A. Rahimi, Y. Sun, A. Kharaghani, and E. Tsotsas. *Pore network simulation of penetration and evaporation of liquid droplet on porous particle*, 4th European Drying Conference, Paris, France, Oct. 2013.

Oral and poster presentations in national and international conferences

1. A. Rahimi, A. Kharaghani, T. Metzger, and E. Tsotsas. *Drying of a shrinking porous medium saturated with a solution: a pore network study*, to be presented (oral) in 6th European Drying Conference, Torino, Italy, 10-12 Jul. 2019.

2. A. Rahimi, T. Metzger, A. Kharaghani, and E. Tsotsas. *Pore network modeling of shrinkage during drying of porous media saturated with salt solution*, presented (oral) in Jahrestreffen der ProcessNet-Fachgruppe Trocknungstechnik, Essen, Germany, 18-20 Mar. 2019.

3. A. Rahimi, T. Metzger, A. Kharaghani, and E. Tsotsas. *Discrete modeling of ion transport and crystallization in layered porous media during drying*, presented (poster) in 21st International Drying Symposium, Valencia, Spain, 18-21 Sep. 2018.

4. A. Rahimi, T. Metzger, A. Kharaghani, and E. Tsotsas. *Migration of dissolved component during drying of composite solid material*, presented (oral) in Jahrestreffen der ProcessNet-Fachgruppe Trocknungstechnik, Merseburg, Germany, 26-28 Feb. 2018.

5. A. Rahimi, T. Metzger, A. Kharaghani, and E. Tsotsas. *Discrete modeling of ion transport and crystallization in porous media during a combined wetting-drying process*, presented (oral) in Jahrestreffen der ProcessNet-Fachgruppe Trocknungstechnik, Bruchsal, Germany, 14-15 Feb. 2017.

6. A. Rahimi, A. Kharaghani, T. Metzger, and E. Tsotsas. *Solute transport and crystallization in a combined wetting-drying pore network model*, presented (oral) in IVT Colloquium, Magdeburg, Germany, 15 Oct. 2016.

7. A. Rahimi, T. Metzger, A. Kharaghani, and E. Tsotsas. *Solute transport and crystallization in a combined wetting-drying pore network model*, presented (oral) 20th International Drying Symposium, Gifu, Japan, 7-10 Aug. 2016.

8. A. Rahimi, T. Metzger, A. Kharaghani, and E. Tsotsas. *Drying salt solutions in porous media by a 3D pore network model*, presented (oral) in The 5th International Workshop on CRYStallisation in POrous Media, Toulouse, France, 6-8 Jun. 2016.

9. A. Rahimi, T. Metzger, A. Kharaghani, and E. Tsotsas. *3D Pore network model for drying salt solutions in porous media*, presented (oral) in Jahrestreffen der ProcessNet-Fachgruppe Trocknungstechnik, Weimar, Germany, 14-15 Mar. 2016.

10. A. Rahimi, A. Kharaghani, T. Metzger, and E. Tsotsas. *Pore network simulatin of salt crystallization in drying porous media*, presented (oral) in 5th European Drying Conference, Budapest, Hungary, 21-23 Oct. 2015.

11. A. Rahimi, A. Kharaghani, T. Metzger, and E. Tsotsas. *Pore network model for drying of salt solutions: solute migration and crystallization*, presented (oral) in 1st Nordic Baltic Drying Conference, Gdansk, Poland, 17-19 Jun. 2015.

12. A. Rahimi, T. Metzger, A. Kharaghani, and E. Tsotsas. *Drying-induced discrete salt crystallization within a porous matrix*, presented (oral) in Jahrestreffen der ProcessNet-Fachgruppe Trocknungstechnik, Leipzig, Germany, 4-6 Mar. 2015.

13. A. Rahimi, T. Metzger, A. Kharaghani, and E. Tsotsas. *Droplet migration into porous substrate simulated by mono-modal and bimodal networks*, presented (oral) in 19th International Drying Symposium, Lyon, France, 24-27 Aug. 2014.

14. A. Rahimi, T. Metzger, A. Kharaghani, and E. Tsotsas. *Pore network simulation to determine the influence of pore structure on wetting-drying kinetics of*

porous particles, presented (oral) in Jahrestreffen der ProcessNet-Fachgruppe Trocknungstechnik, Karlsruhe, Germany, 19-21 Feb. 2014.

15. A. Rahimi, Y. Sun, A. Kharaghani, and E. Tsotsas. *Pore network simulation of penetration and evaporation of liquid droplet on porous particle*, presented (poster) in 4th European Drying Conference, Paris, France, Oct. 2013.